

AD-A162 160



AFOSR-TR- 85-1070

ROTORDYNAMIC FORCES DEVELOPED

BY LABYRINTH SEALS

by

DARA W. CHILDS

DAVID L. RHODE

NOVEMBER 1984

DTIC
S ELEC
DEC 9 1985
A

Turbomachinery Laboratories
Mechanical Engineering Department

UNCLASSIFIED

SECURITY CLASSIFICATION OF THIS PAGE

REPORT DOCUMENTATION PAGE

1a. REPORT SECURITY CLASSIFICATION UNCLASSIFIED		1b. RESTRICTIVE MARKINGS	
2a. SECURITY CLASSIFICATION AUTHORITY Unclassified		3. DISTRIBUTION/AVAILABILITY OF REPORT Approved for public release; distribution unlimited.	
2b. DECLASSIFICATION/DOWNGRADING SCHEDULE			
4. PERFORMING ORGANIZATION REPORT NUMBER(S)		5. MONITORING ORGANIZATION REPORT NUMBER(S) AFOSR-TR- 85 - 1070	
6a. NAME OF PERFORMING ORGANIZATION Texas A&M University	6b. OFFICE SYMBOL (If applicable)	7a. NAME OF MONITORING ORGANIZATION AFOSR/NA	
6c. ADDRESS (City, State and ZIP Code) College Station, Texas 77843-3123		7b. ADDRESS (City, State and ZIP Code) Bolling AFB DC 20332-6448	
8a. NAME OF FUNDING/SPONSORING ORGANIZATION Air Force Office of Scientific Research	8b. OFFICE SYMBOL (If applicable) AFOSR/NA	9. PROCUREMENT INSTRUMENT IDENTIFICATION NUMBER F49620-82-K-0033	
8c. ADDRESS (City, State and ZIP Code) Bolling Air Force Base, D.C. 20332-6448		10. SOURCE OF FUNDING NOS.	
		PROGRAM ELEMENT NO. 61102F	PROJECT NO. 2302/ B1
11. TITLE (Include Security Classification) Rotordynamic Forces Developed by Labyrinth Seals		TASK NO. B1	
12. PERSONAL AUTHOR(S) Dara W. Childs and David L. Rhode		WORK UNIT NO.	
13a. TYPE OF REPORT Annual	13b. TIME COVERED FROM 9/1/83 TO 8/31/84	14. DATE OF REPORT (Yr., Mo., Day) November 1984	15. PAGE COUNT 143
16. SUPPLEMENTARY NOTATION			
17. COSATI CODES		18. SUBJECT TERMS (Continue on reverse if necessary and identify by block number)	
FIELD	GROUP	SUB. GR.	
		Labyrinth Seals	
		Rotordynamic Forces	
		Computational Fluid Dynamics	
19. ABSTRACT (Continue on reverse if necessary and identify by block number)			
<p>Numerous developments have been completed toward the accurate measurement and prediction of the fluid-structure-interaction forces on labyrinth seals. The test facility was refined and data acquisition was automated. Measurements were obtained of both stiffness and damping force coefficients for two labyrinth seal configurations operating with small rotor motion about its centered position. Only the cross-coupled damping coefficient exhibits significant sensitivity to shaft speed, and the coefficients increase monotonically with increasing supply-to-discharge pressure ratio. Fluid pre-rotation exhibits a strong influence on cross-coupled stiffness, which increases and decreases, respectively, with pre-rotation in and opposite to the direction of shaft rotation. Direct damping is less sensitive to fluid pre-rotation, and is generally largest for pre-rotation against the shaft direction.</p> <p>A simple Iwatsubo-based force coefficient model was also developed. Predictions obtained from the approximate model are much more sensitive to shaft speed than corresponding current measurements, and damping values are approximately one-fourth of those measured.</p>			
20. DISTRIBUTION/AVAILABILITY OF ABSTRACT UNCLASSIFIED/UNLIMITED <input checked="" type="checkbox"/> SAME AS RPT. <input type="checkbox"/> DTIC USERS <input type="checkbox"/>		21. ABSTRACT SECURITY CLASSIFICATION UNCLASSIFIED	
22a. NAME OF RESPONSIBLE INDIVIDUAL Dr A K Amos		22b. TELEPHONE NUMBER (Include Area Code) 202/767-4937	22c. OFFICE SYMBOL AFOSR/NA

UNCLASSIFIED

SECURITY CLASSIFICATION OF THIS PAGE

In addition, most tasks were completed in the development of a much more sophisticated prediction model which solves the finite difference form of the complete, three-dimensional, Reynolds-averaged Navier-Stokes equations for compressible flow. False diffusion errors were eliminated and considerable computer processing cost reductions were implemented. A highly successful compressible, recirculating flow prediction test case reveals that the concentric-rotor (two-dimensional) version of the computer program provides results which are in close agreement with corresponding measurements. A brief exploratory prediction of the compressible air flow within a concentric-rotor, generic, teeth-on-rotor seal indicates that the seal cavity distribution of dimensionless temperature and swirl velocity may be represented in simple models by a cavity-average value of approximately 1.05 and 0.71, respectively. Cavity-average density values are approximately 0.92.

Accession For	
NTIS CRA&I	<input checked="checked" type="checkbox"/>
DTIC TAB	<input type="checkbox"/>
Unannounced	<input type="checkbox"/>
Justification	
By	
Distribution /	
Availability Codes	
Dist	Avail and/or Special
A	



UNCLASSIFIED

TABLE OF CONTENTS

	PAGE
I. INTRODUCTION -----	1
II. EXPERIMENTAL DEVELOPMENTS -----	2
A. Introduction -----	2
B. Research Program-Review -----	2
C. Labyrinth Seal Test Results -----	4
D. Research Program - Plans for Current Year -----	15
E. Graduate Student Development -----	16
III. COMPUTATIONAL DEVELOPMENTS -----	18
A. Introduction -----	18
B. False Diffusion -----	18
C. Compressible Flow Prediction Test Case of Concentric-Rotor (2-D) Computer Code -----	20
D. Prediction of Compressible Flow in a Concentric-Rotor Labyrinth Seal -----	28
E. Eccentric-Rotor (3-D) Computer Code Development -----	38
F. Summary -----	40
G. Graduate Student Development -----	41
H. Publications -----	41
I. Conference Presentations -----	42
IV. REFERENCES -----	43
V. APPENDIX A - "An Iwatsubo-Based Solution for Labyrinth Seals - Comparison to Experimental Results."	

AIR FORCE OFFICE OF SCIENTIFIC RESEARCH (AFOSR)
 NOTICE OF TRANSFER TO AFOSR
 This technology is the property of the Air Force Office of Scientific Research
 approved for release on 10-10-12.
 Distribution is unlimited.
 MATTHEW J. KENNEDY
 Chief, Technical Information Division

- VI. APPENDIX B - "A Comparison of Experimental and
Theoretical Results for Leakage, Pressure Distribution,
and Rotordynamic Coefficients for Annular Gas Seals."
- VII. APPENDIX C - "On the Prediction of Incompressible Flow
in Labyrinth Seals."

I. INTRODUCTION

Seals develop fluid-structure-interaction forces due to the relative motion of the rotor and housing at seal locations, and these forces have been shown to have a significant influence on the rotordynamic stability and response characteristics of high performance turbomachinery. The present research effort was initiated in September of 1982, and is a combined computational-experimental program to develop experimentally-validated computational approaches for predicting seal forces. More specifically, computational approaches are being developed to define the force coefficients for the force-motion relationship:

$$- \begin{Bmatrix} F_X \\ F_Y \end{Bmatrix} = \begin{bmatrix} K & k \\ -k & K \end{bmatrix} \begin{Bmatrix} X \\ Y \end{Bmatrix} + \begin{bmatrix} C & c \\ -c & C \end{bmatrix} \begin{Bmatrix} \dot{X} \\ \dot{Y} \end{Bmatrix} \quad (1)$$

where (X,Y) are components of the relative displacement vector between the rotor and the stator at the seal location, and (F_X, F_Y) are components of the reaction force resulting from transient pressure and velocity distributions within the seal. The computational approaches which are being developed in this study will define the pressure and velocity distributions within the seal which result from relative rotor-stator motion. The computational approaches are to be validated by comparison to experimental measurements of the following quantities:

- (a) transient measurements of the displacement (X, Y) and force (F_X, F_Y) components, which results in calculated values for the rotordynamic (stiffness and damping) coefficients of Eq. (1), and
- (b) laser velocimeter measurements of the velocity distributions within labyrinth seal cavities.

Dr. Childs and Dr. Rhode are responsible, respectively, for the

experimental and computational developments. In the following two chapters, reviews are provided of the research accomplishments with respect to these two complementary facets of the research projects.

II. EXPERIMENTAL DEVELOPMENTS

A. Introduction

The experimental developments of this program are jointly supported by NASA and AFOSR. NASA funds (\$323,749; 1 July 1981 to 31 December 1984) have been used to develop the test facility and test apparatus and to support analytical-computational developments. NASA officials are primarily interested in annular seals having constant-clearance or convergent-taper geometries with smooth and honeycomb stator surfaces. Their interest in this type of seal arises from applications in the turbine areas of the high-pressure turbopumps of the Space Shuttle Main Engine. This status report reviews the progress of the complete program without distinguishing between sources of support.

B. Research Program - Review

During the past year, the test program has been in a "shakedown" mode involving the following developments:

- (a) Accelerometers were installed on the stator to correct for acceleration-induced forces which are measured by the transient load cells. Software and electronics have been developed to implement this correction.
- (b) One of the hollow roller bearings which support the test shaft in its housing was installed improperly by the original machine shop and failed. Replacement units were installed properly and have worked

satisfactorily.

(c) The original coolant and lubricant loop for the radial bearings and the thrust bearing was found to be inadequate and was replaced.

(d) A stepper motor was added to provide remote external control for vertical positioning of the test section seal.

(e) A 4:1 belt-pulley speed increaser was added to the electric-motor drive system to provide a theoretical top speed of 21,500 cpm. This eliminated the need for the installation of an air turbine which was originally provided for higher speeds. The belt-drive system also eliminated the undesirable restraint of the coupling which was originally provided as a low-speed drive system. The pulley system has a marginal but adequate lifetime out to 20,000 rpm when transmitting up to 30 hp.

(f) Extensive software has been developed to expedite the execution of testing and the processing and presentation of test data. As a result, 150 data points can generally be secured in under three hours.

(g) An approximate analysis was developed [1] based on Iwatsubo's work [2] for the prediction of leakage and the rotordynamic coefficients of Eq. (1) for labyrinth seals. A copy of reference [1] is attached. In comparison to previously published data of Wachter and Benckert [3], the analysis provides satisfactory results. However, Wachter and Benckert provide only direct and cross-coupled stiffness data (K and k of Eq. (1)), with no damping measurements. Further, the data only applies for fluid prerotation without shaft rotation, or shaft rotation without fluid rotation. As specified in [1], the approximate analysis is in rough agreement with teeth-on-stator data but is completely at odds with the published teeth-on-rotor results.

(h) The following seal configurations were tested:

- (i) smooth, constant-clearance,
- (ii) smooth, convergent-tapered,
- (iii) smooth-rotor, honeycomb stator,
- (iv) constant-clearance labyrinth with teeth-on-stator, and
- (v) constant-clearance labyrinth with teeth-on-rotor.

The honeycomb seal was provided by NASA and Rocketdyne and is the turbine interstage seal for the HPOTP (High Pressure Oxygen Turbopump) of the SSME (Space Shuttle Main Engine). The two labyrinth seals are illustrated in figure 1 and use cavity and tooth dimensions based on G. E. aircraft-gas-turbine design practice.

C. Labyrinth Seal Test Results

The test apparatus and facility are described in detail in Nicks' thesis [4], which is attached as part of this report. The test apparatus has the capability to identify the seal rotordynamic coefficients of the general linearized model

$$-\begin{Bmatrix} F_X \\ F_Y \end{Bmatrix} = \begin{bmatrix} K_{XX}(e_0) & K_{XY}(e_0) \\ K_{YX}(e_0) & K_{YY}(e_0) \end{bmatrix} \begin{Bmatrix} X \\ Y \end{Bmatrix} + \begin{bmatrix} C_{XX}(e_0) & C_{XY}(e_0) \\ C_{YX}(e_0) & C_{YY}(e_0) \end{bmatrix} \begin{Bmatrix} \dot{X} \\ \dot{Y} \end{Bmatrix} \quad (2)$$

for small motion about an arbitrary static eccentricity position defined by e_0 , e.g., $X_0 = e_0$, $Y_0 = 0$. This is in contrast to the model of Eq. (1) which applies for small motion about a centered position.

The following parameters can be controlled in testing:

- (a) Pressure ratio. The seal discharge pressure is atmospheric, and the supply pressure can be increased from zero to approximately 90 psi.
- (b) Running speed. The running speed range for the present test apparatus is zero to 8000 rpm.

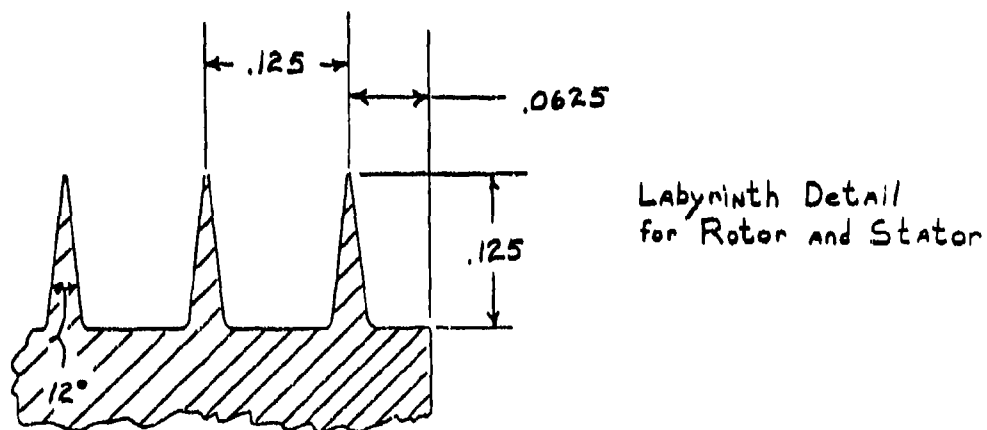
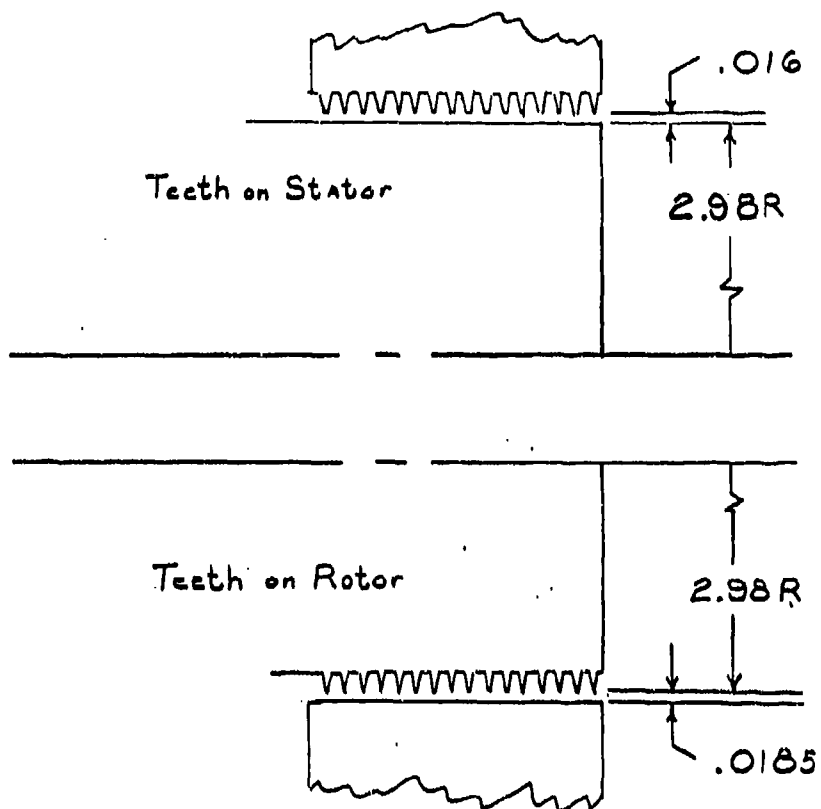


FIGURE 1. Labyrinth Test Configuration

(c) Inlet Tangential Velocity. Swirl rings are provided at the seal inlet to prerotate the flow either in the same direction or an opposite direction to rotation. Also, fluid can be introduced with no intentional prerotation.

All testing is done with air and includes static measurements of the entrance and exit pressures and temperatures, and pressure measurements in each labyrinth cavity. The testing reported here is for small motion about a centered position.

Figure 2 illustrates the test results for a tooth-on-rotor labyrinth seal configuration with fluid prerotation in the direction of shaft rotation. The independent variable is running speed and families of curves are presented for various pressure ratios. Observe that all of the coefficients, except for the cross-coupled damping coefficients, are relatively insensitive to running speed. The cross-coupled damping coefficient displays the most erratic behavior with respect to its dependency on running speed and pressure ratio. Again, from figure 2, observe the general monotonic increase of the rotordynamic coefficients with increasing pressure ratios.

From a rotordynamics viewpoint, the direct damping and cross-coupled stiffness coefficients are quite significant in determining the stability and peak response characteristics of rotors. The direct stiffness and cross-coupled damping terms have a minute influence on critical speed locations and are of markedly less interest. Figures three and four illustrate the dependence of these coefficients on pressure ratio. The three curves on each of these figures are for no fluid prerotation and prerotation in the same and opposite direction, respectively, to shaft rotation. The curves connect the average value, with respect to speed, for

FIGURE 2(a). Direct stiffness results for teeth-on rotor labyrinth seal configuration with fluid prerotation in the direction of shaft rotation.

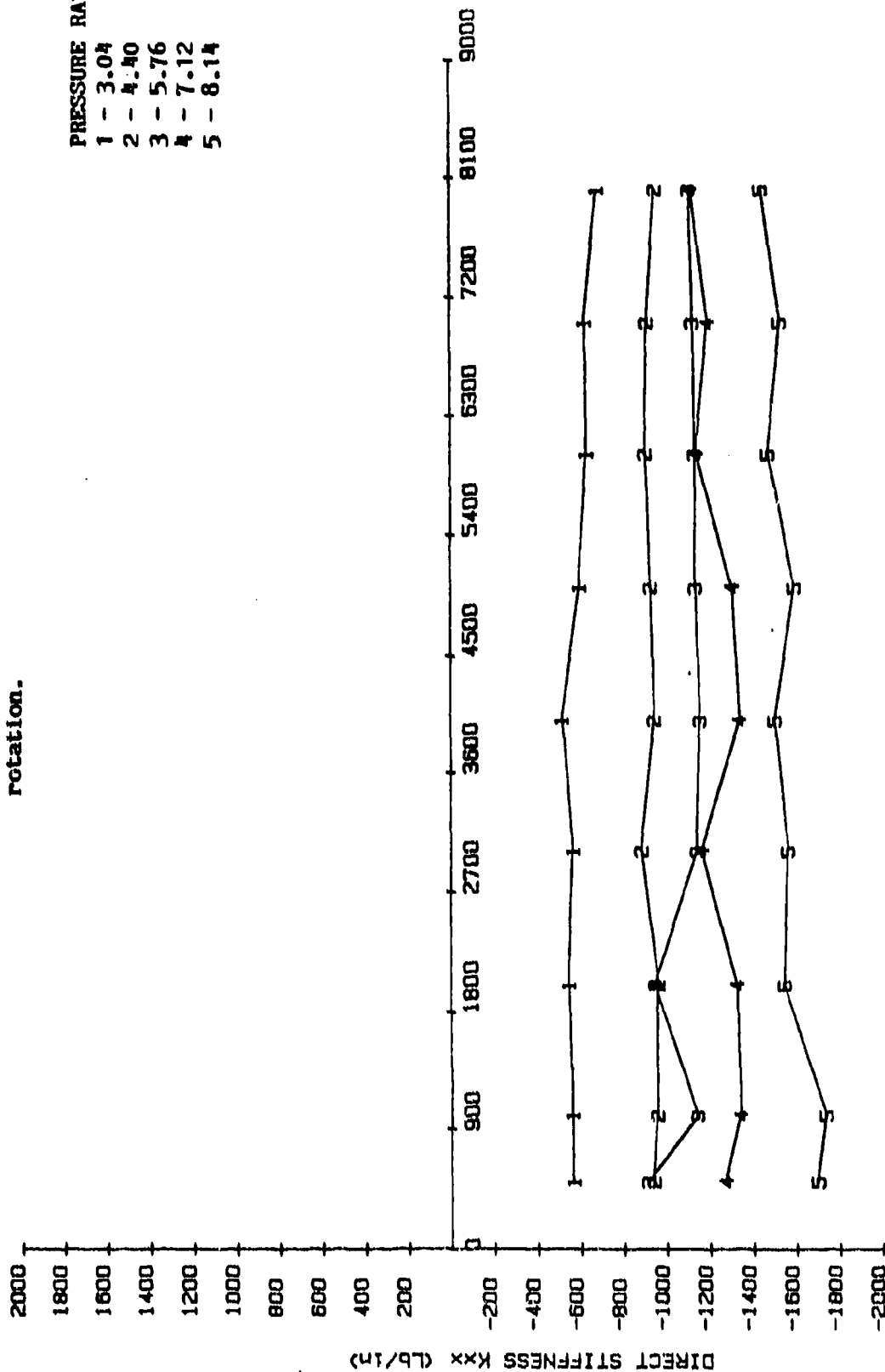


FIGURE 2(b). Cross-coupled stiffness results for teeth-on-rotor labyrinth seal configuration with fluid rotation in the direction of shaft rotation.

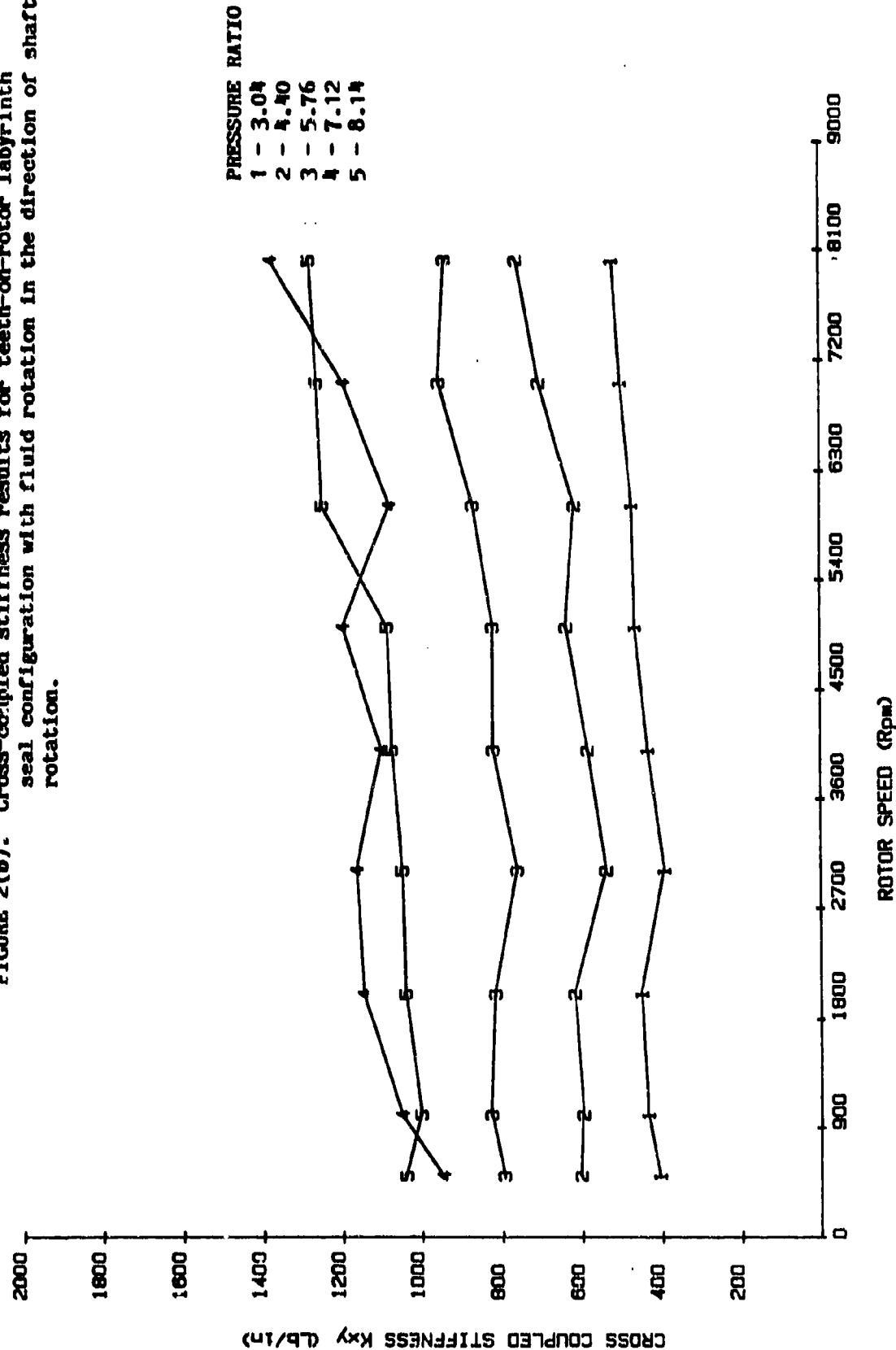


FIGURE 2(c). Direct damping results for teeth-on-rotor labyrinth seal configuration with fluid rotation in the direction of shaft rotation.

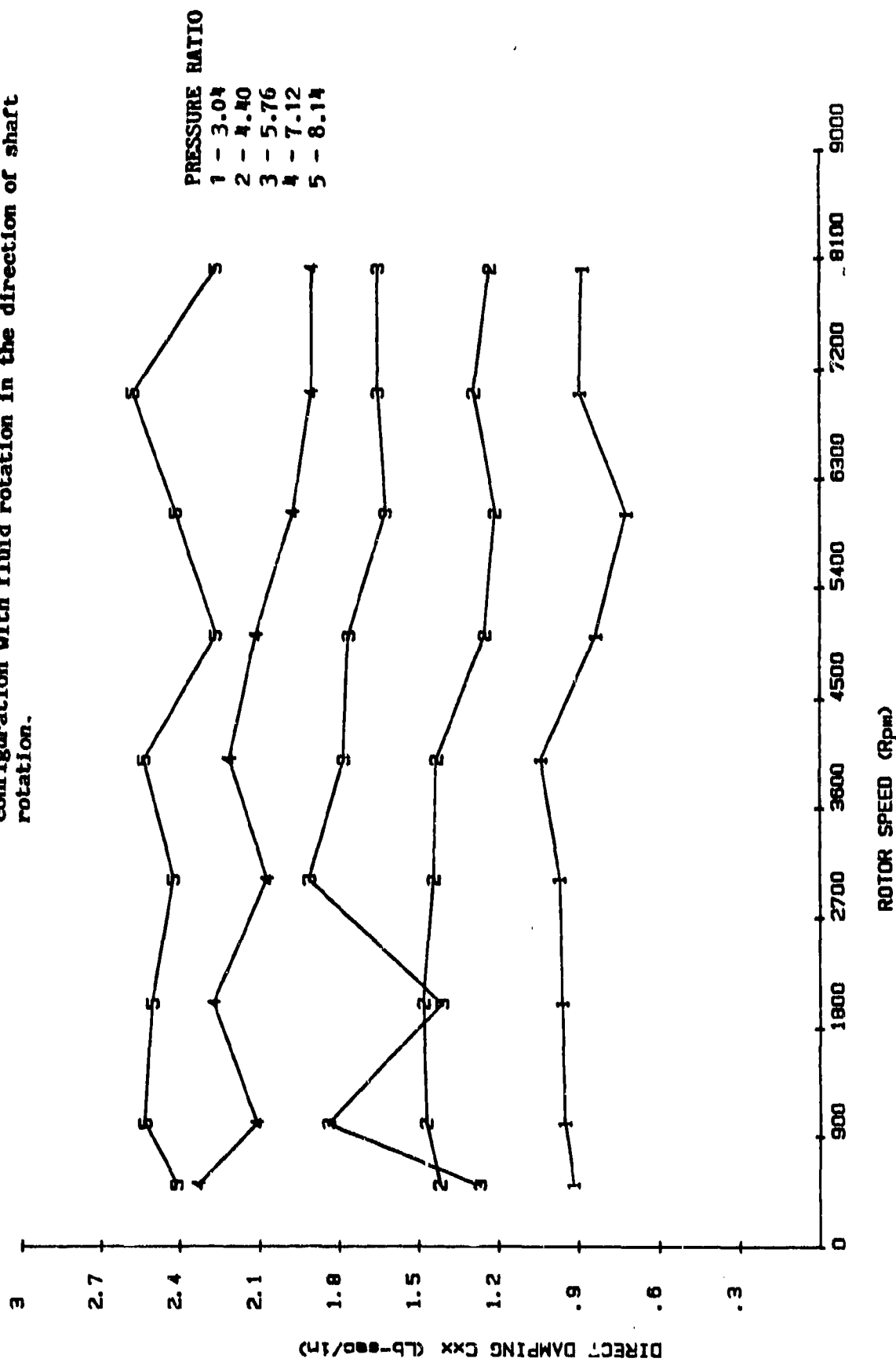
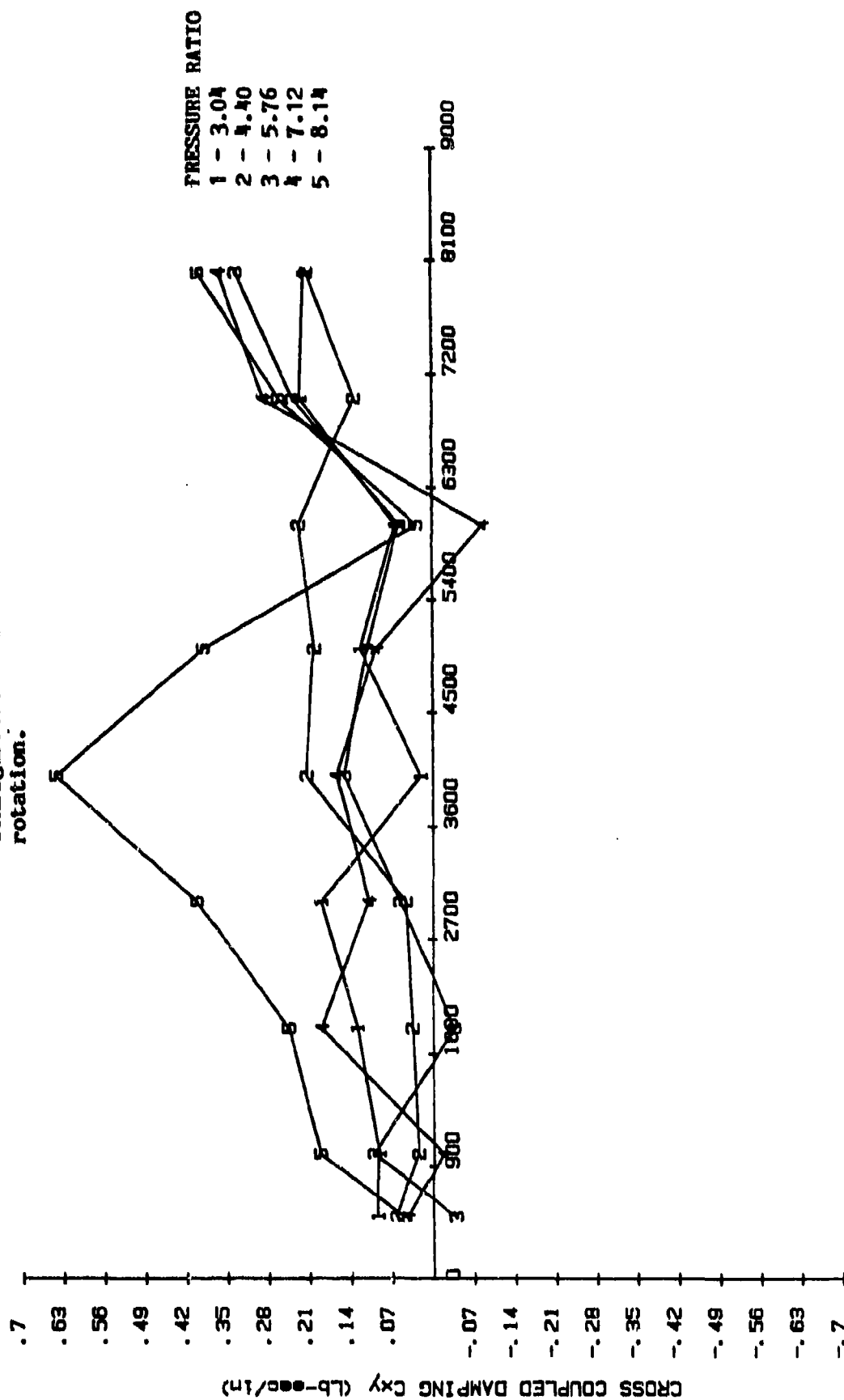
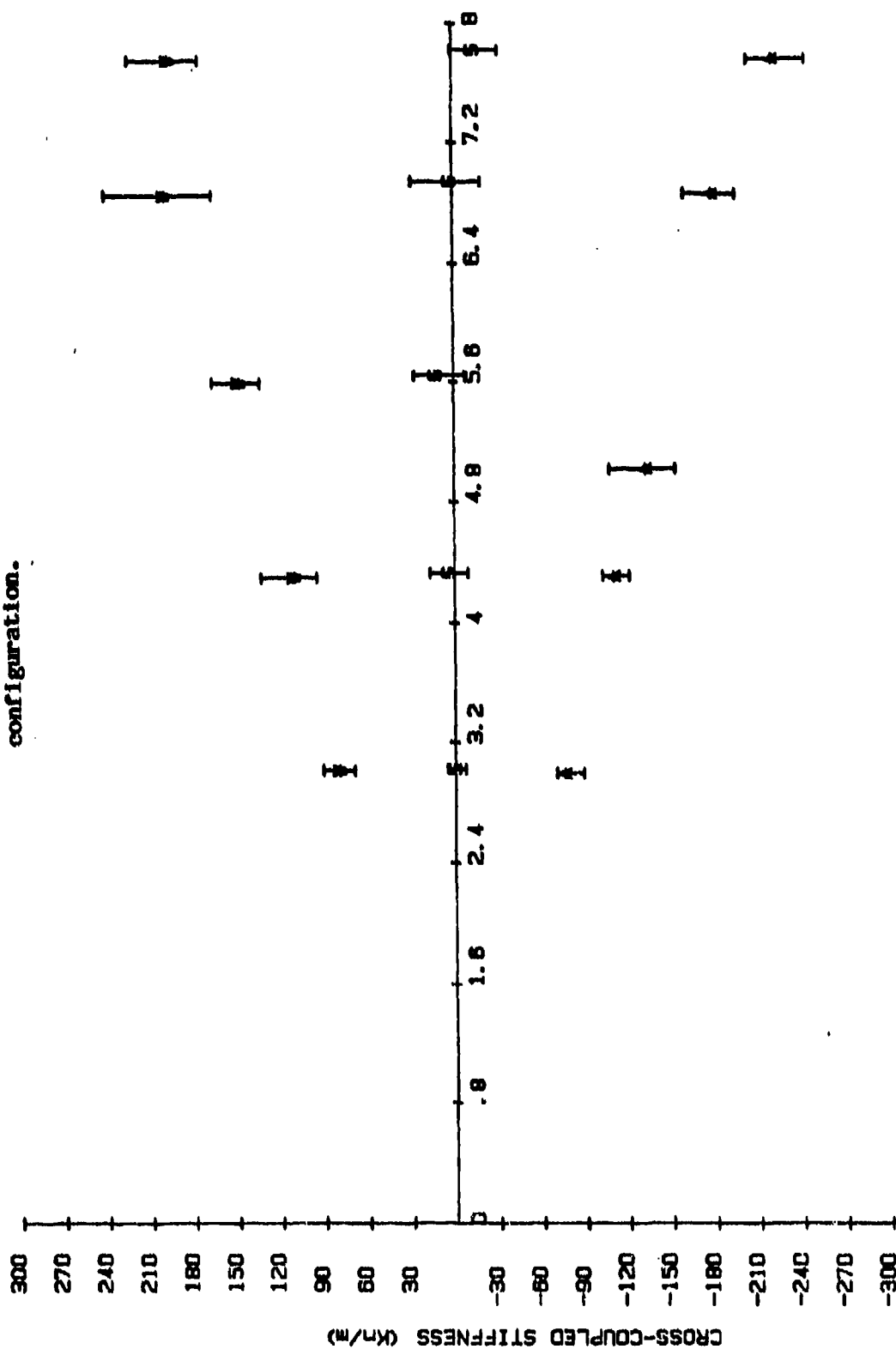


FIGURE 2(d). Cross-coupled damping results for teeth-on-rotor labyrinth seal configurations with fluid rotation in the direction of shaft rotation.



ROTOR SPEED (Rpm)

FIGURE 3(a). Cross-coupled stiffness versus pressure ratio for three inlet-tangential-velocity conditions; teeth-on-rotor configuration.



PRESSURE RATIO (PR/PS)

FIGURE 3(b). Direct damping versus pressure ratio for three inlet-tangential-velocity conditions; teeth-on-rotor configuration.

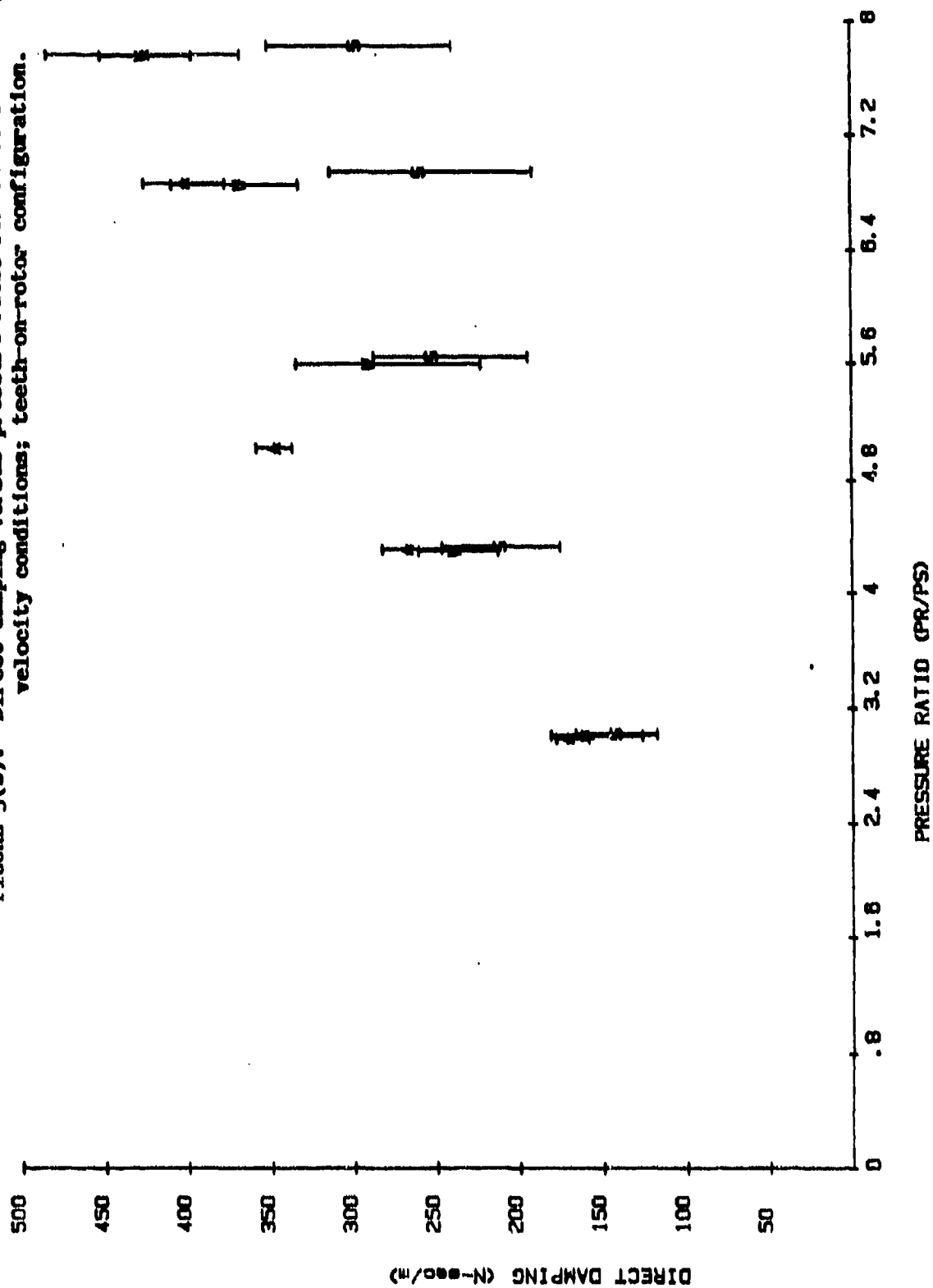
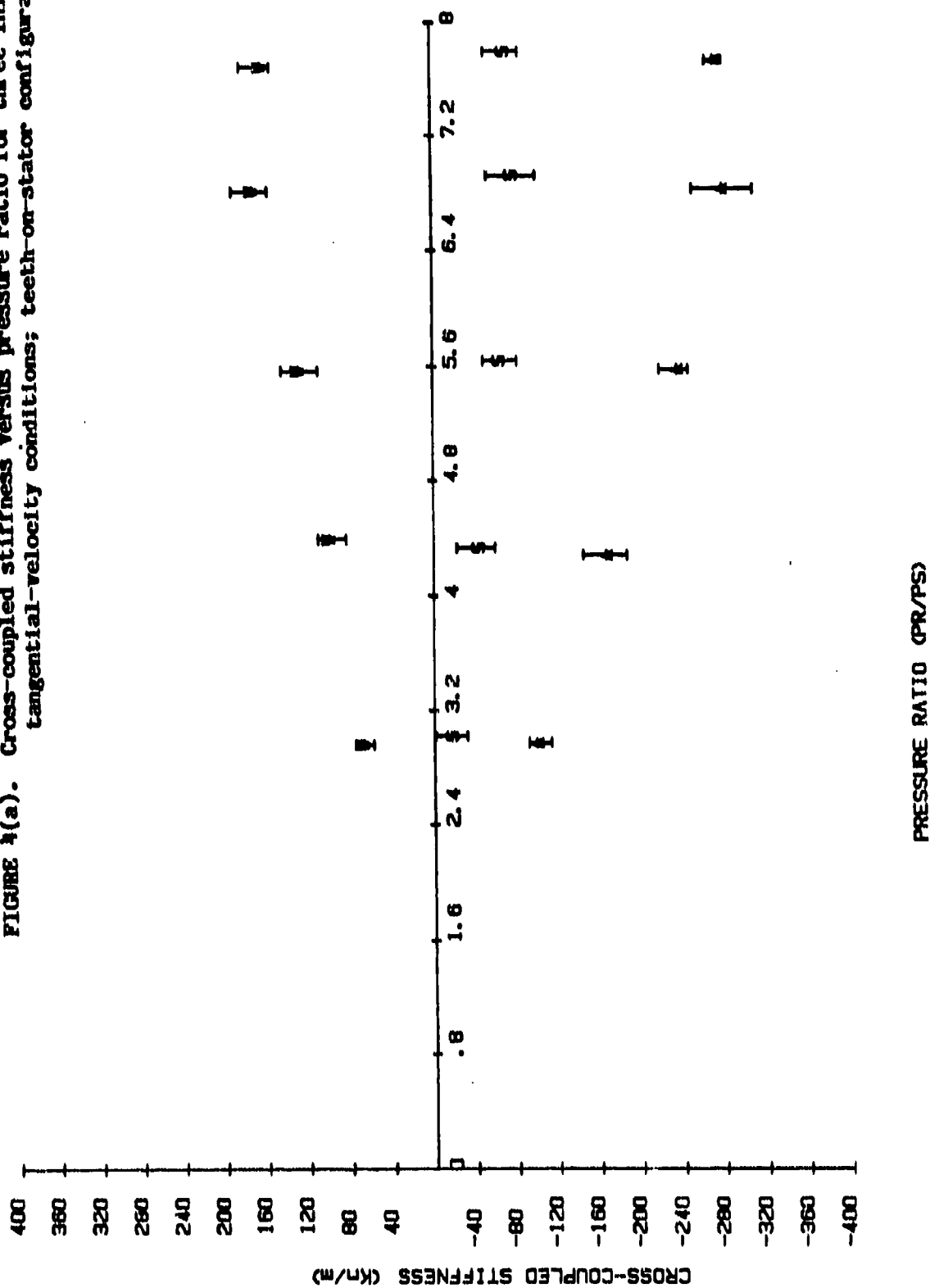
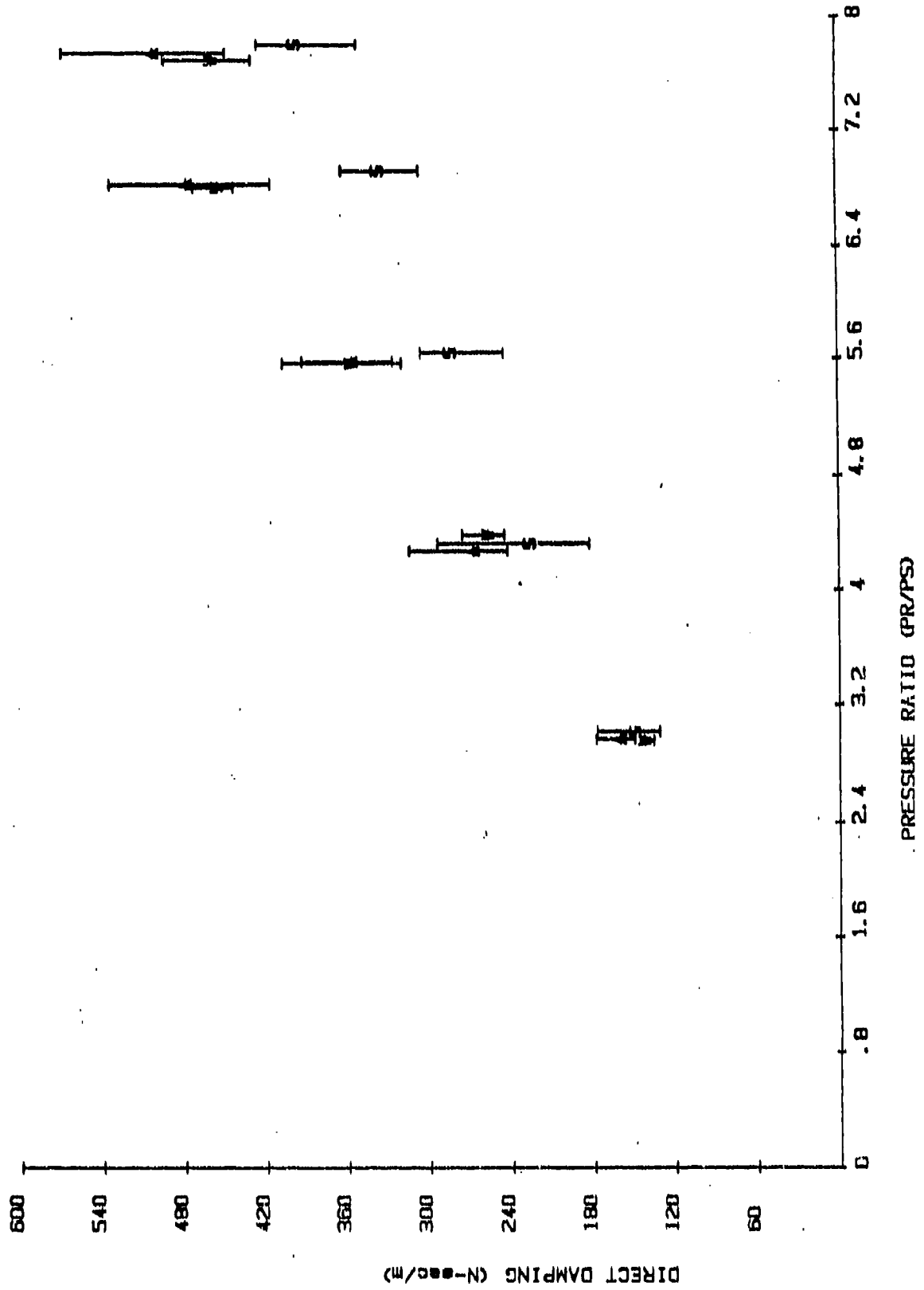


FIGURE 4(a). Cross-coupled stiffness versus pressure ratio for three inlet-tangential-velocity conditions; teeth-on-stator configuration.



PRESSURE RATIO (PR/PS)

FIGURE 4(b). Direct damping versus pressure ratio for three inlet-tangential-velocity conditions; teeth-on-stator configuration.



each coefficient. The horizontal bars, which connect the vertical lines through each data point show the extreme values due to speed dependency.

With respect to the cross-coupled stiffness, the results of figures 3 and 4 show a strong influence on fluid prerotation with k increasing and decreasing due to fluid prerotation, respectively, in the direction of shaft rotation and opposed to shaft rotation. Comparatively small values result for no shaft rotation. Cross-coupled stiffness values are generally smaller for teeth-on-stator than teeth-on-rotor configurations.

The direct damping value is less sensitive to fluid prerotation. It is generally largest for fluid prerotation against shaft rotation, moderately smaller for prerotation in the same direction as rotation, and smallest for no fluid prerotation. Observe that direct damping increases with the pressure ratio and would have an approximate, extrapolated zero value for a pressure ratio of one.

The test results provided in figures 2 through 4 are vastly better than any which have previously been published. They have only recently been obtained and will obviously require substantial additional study. The correlation with the analysis of reference [1], developed in this study, is disappointing. Specifically, measured cross-coupled stiffness coefficients are much less sensitive to running speed than predicted, and measured damping values are on the order of four times higher than predictions. As discussed in the following section, a "new and improved" but still quite simplified solution will be developed in the coming year which should substantially improve the correlation between theory and experiment.

D. Research Program - Plans for Current Year

The following specific tasks will be completed in current contract

time period:

(a) Test Apparatus Development. The labyrinth seals leak a great deal less than the annular seals which have been tested in the past for NASA. As a consequence the vortex flow meter which was originally purchased has proven to be oversized and will shortly be replaced by an appropriately sized turbine flow meter. In addition, the inlet swirl rings were also oversized to achieve sufficiently high tangential velocities and are being supplemented with new units. Finally, various redesigns are underway to yield a sharp increase in running speed, probably to something on the order of 15,000-16,000 rpm.

(b) Computational Developments. As noted earlier, a simplified analysis has been developed for the prediction of rotordynamic coefficients of labyrinth seals [1], and has not proven to be particularly satisfactory. The motivation for developing this type of analysis, as compared to the complete three-dimensional Navier-Stokes solution of Dr. Rhodes, is quite simply cost and convenience. A relatively simplified analysis is needed for design purposes. A "new and improved" simplified analysis is currently under development based on the work of Jenny, Wyssman, and Pham [5]. We propose to "calibrate" this model by comparison to Dr. Rhodes' more comprehensive solution.

(c) LDA Developments. Dr. Morrison and his graduate student, Mr. Mike Long, will continue to work at achieving velocity measurements within a labyrinth cavity.

E. GRADUATE STUDENT DEVELOPMENT

Mr. Joseph Scharrer has been working on this project since 1 January 1983. Mr. Scharrer concluded his B. S. degree in Mechanical Engineering at

Northern Arizona University in July of 1982 (in three years). He has been accepted into the AFRAPT program by TAMU and spent the summer of 1984 with General Electric at Lynn, Massachusetts. Mr. Scharrer has been responsible for a great deal of the experimental development work on this project, and has recently assisted in the development of an improved prediction model for rotordynamic-coefficients of a labyrinth seal [1]. Mr. Mike Long has been working with this project for the past year with Dr. Gerald Morrison on the development of LDA measurement techniques for labyrinth seals. He spent the summer working with Garrett at Phoenix, Arizona.

III. COMPUTATIONAL DEVELOPMENTS

A. Introduction

Good progress has been made in developing an advanced, user-simplistic, experimentally-validated, finite difference computer code for predicting the pressure and velocity fields and subsequently the four rotordynamic force coefficients of Eq. (1). The problem of subsonic air flow through a labyrinth seal is clearly elliptic, as recirculation zones have been observed in flow visualization experiments [6]. Also, it is three-dimensional because of rotor eccentricity effects which are of primary concern. It has been assumed that the rotor instability is manifested as a circular precessional orbit of frequency ω about the seal center position. The desired solution will be obtained from the steady-state form of the governing flow equations because a steady-state flowfield precesses along with the rotor in a $r-\theta$ plane.

Once the predicted pressure distribution (for a given orbital velocity ω) acting on the rotor is obtained, it will be employed to calculate the resulting F_x and F_θ forces. A second computation of the pressure and rotor force components at a different value of ω finally allows each of the all-important stiffness (K, k) and damping (C, c) coefficients to be calculated as needed for dynamics calculations of the rotor.

B. False Diffusion

Until recently, the upwind differencing scheme has been the most effective method for obtaining a stable numerical solution of

convection-dominated flows. However, this scheme is only first-order accurate and may introduce serious truncation errors known as false diffusion. This is especially true for flows where convection dominates (i.e., where the grid Peclet number $|Pé| \equiv |V|\Delta/\Gamma_\phi$ exceeds 2.0) with substantial streamline-to-grid skewness and diffusive transport normal to the flow direction.

False diffusion results in an overly diffusive solution. A turbulent recirculating flow, such as that within some labyrinth seals, is particularly susceptible to the effects of false diffusion because of its regions of considerable velocity gradient and streamline-to-grid skewness. One way to prevent false diffusion is to utilize a sufficiently fine grid so that central differencing for the convective terms may be used throughout the calculation domain. However, this is quite expensive for two-dimensional flows and prohibitive for three-dimensional ones.

The Hybrid upwind/central differencing scheme was originally embodied in the incompressible flow code. Using this method, the convective terms are formulated by upwind differencing for a grid Peclet number larger than 2.0; otherwise, central differencing is used. This differencing scheme has yielded solutions in which false diffusion has entirely obscured physical diffusion [7,8].

The recent QUICK scheme derived by Leonard [9] eliminates false diffusion. This scheme has been implemented in an original and highly stabilizing way. It eliminates false diffusion by incorporating a three-point upwind-shifted quadratic interpolation formula. Rhode, et al. [10] showed comparisons between the Hybrid and QUICK differencing schemes for incompressible flow in labyrinth seal cavities. It was shown that the

QUICK scheme yields a grid-independent solution using a considerably more coarse grid than does the Hybrid scheme, thereby considerably reducing the computational effort required. In that concentric-rotor seal flow problem, it was found that a solution of given accuracy was obtained using QUICK while consuming only 44% of the execution time required by the state-of-the-art Hybrid scheme. This advantage will certainly be more dramatic for the three-dimensional (eccentric-rotor) seal flow problems which lie ahead. This computational advancement was also presented by Rhode, et al. [11] for corresponding compressible flows.

Both the incompressible and the compressible flow labyrinth seal papers above included the complete distribution of numerous quantities revealing the detailed flow character throughout a realistic labyrinth seal cavity. Previously these detailed results were largely unavailable. These results serve to enhance one's fundamental understanding of the compressible flow field in a labyrinth seal which generates the rotordynamic instability forces of interest to gas turbine manufacturers.

C. Initial Compressible Flow Prediction Test Case of Concentric-Rotor (2-D) Computer Code

Due to the late arrival of the Laser-Doppler anemometer, detailed measurements of compressible flow in a labyrinth seal are yet to be obtained. Thus, a brief prediction assessment using a compressible recirculating flow problem was conducted before developing the final three-dimensional version of the code. A short literature search led to the selection of the sudden-expansion dump combustor flowfield

measured by Drewry [12]. He measured stagnation and static pressure as well as static temperature at five axial stations.

The test facility employed by Drewry is shown schematically in Fig. 5. High pressure air enters a large plenum chamber which exits into the 63.5 mm-diameter inlet duct. After passing through this 317.5 mm-long duct, it enters the combustor test section which exhibits a diameter and length of 97.5 mm and 381 mm, respectively. Finally, the flow discharges through a nozzle of 63.5 mm-diameter into the exhaust duct.

This flowfield is characterized by both the Reynolds number and the Mach number. Based on inlet duct conditions, these parameters exhibit values of 1.42×10^6 and 0.67, respectively. The inlet static pressure and temperature are 156 kPa (absolute) and 249.8°K, respectively.

The inlet flow measurements are perhaps most accurate at the measurement station approximately 105.0 mm upstream of the duct expansion (combustor inlet); hence, this location was chosen for the upstream computational boundary where a uniform profile is assumed for the axial velocity and temperature. Values of x in the figures are measured from this reference location. The domain extends downstream 348.0 mm from the expansion. Solutions were obtained using the QUICK scheme with a 34×30 grid as well as the Hybrid scheme with a 53×30 grid.

The overall flow pattern is indicated by the predicted streamline plot shown in Fig. 6. This result was obtained using the QUICK scheme with the 34×30 grid. The stream function is nondimensionalized by the inlet mass flow rate. The recirculating mass flow rate within the recirculation zone is approximately 10% of the inlet value. Drewry's oil

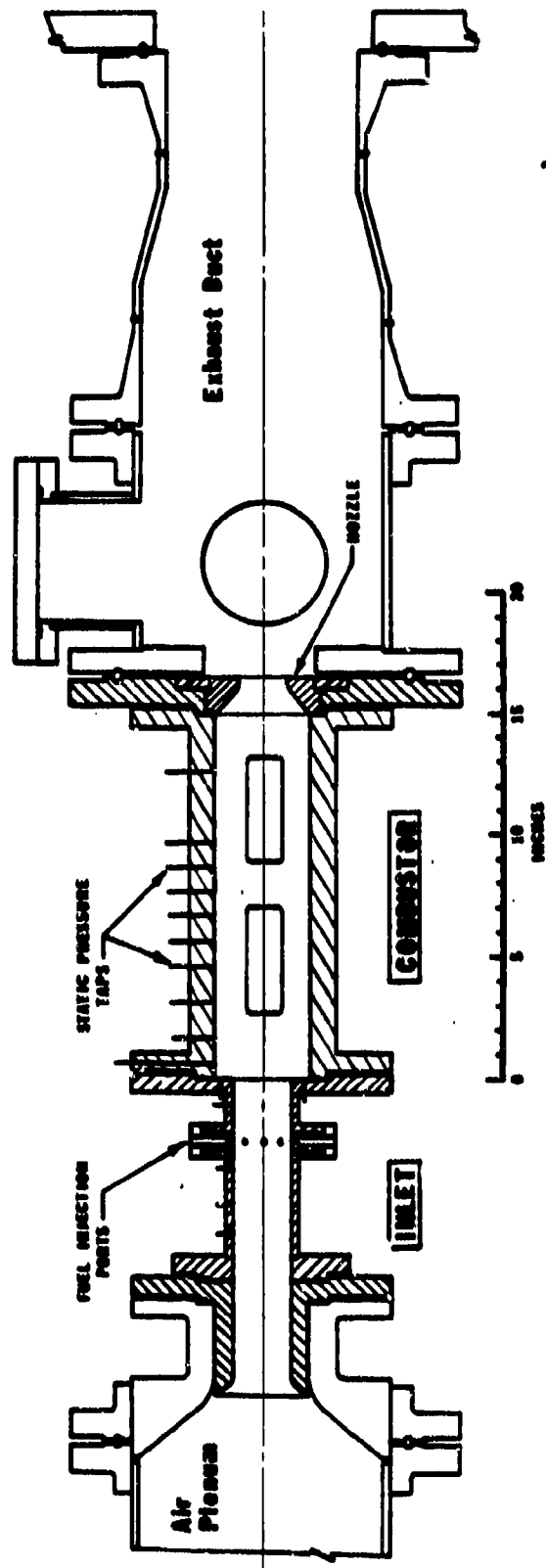


Figure 5. Test facility configuration for Drewry's combustor experiments (Ref. [12]).

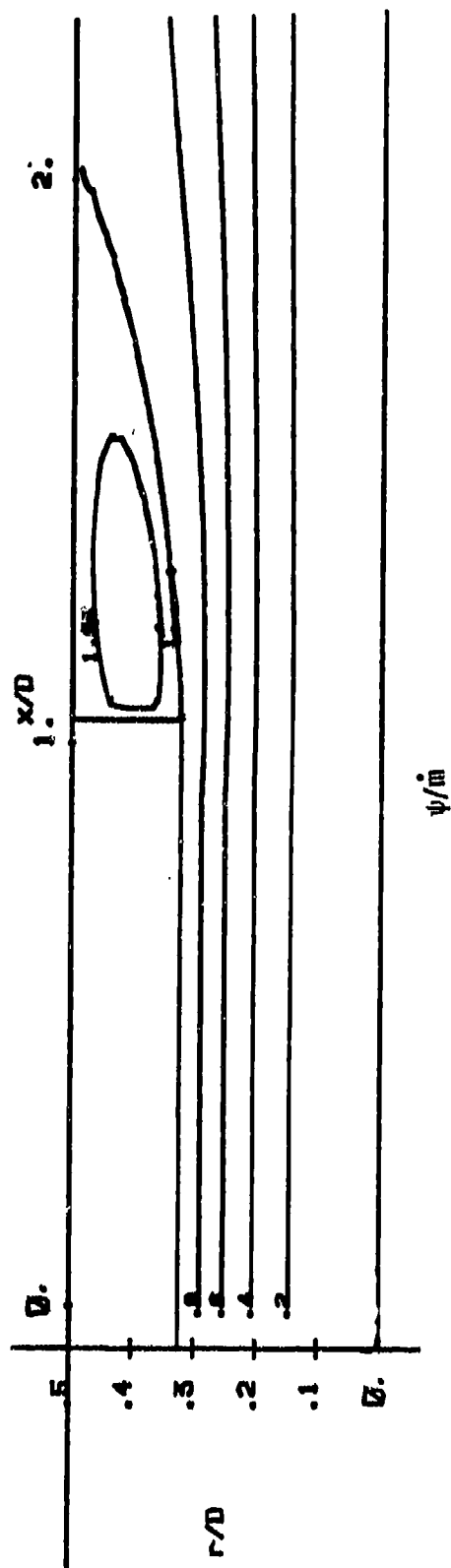


Figure 6. Predicted dimensionless streamline pattern within Drewry's combustor facility showing the 34x30 QUICK solution.

surface flow visualization results indicated that the dividing streamline ($\psi^* = 1.0$) reattachment occurs at $x/D = 1.99$. This length is under-predicted here by only 2.2%. The 53 x 30 Hybrid scheme solution (not shown) is almost identical, except in that case the reattachment length is under-predicted by 6.2%.

The radial profile plots presented in Figures 7 through 10 reveal the degree of agreement with measurements. The QUICK differencing scheme was used along with the 34 x 30 grid in obtaining these predictions. Figure 7 shows predicted and measured time-mean axial velocity profiles, nondimensionalized by the spatially-averaged inlet duct velocity $U = 212.3$ m/s. Observe the excellent agreement at the first and third axial stations in the presence of significantly less agreement at the second station. This is somewhat surprising as the large $\partial u / \partial r$ gradient at the first station appears to represent the most substantial prediction challenge. The discrepancy at the second station is attributed to measurement inaccuracy due to the use of non-directional pressure probes. This occurs for $r/D > 0.3$ where the streamlines were seen to exhibit non-zero slope; hence, relative to the local flow direction, the probe was oriented at a significant pitch angle rather than facing directly into the flow as desired.

Static pressure is given in Fig. 8. Each radial profile is nearly uniform, and the agreement with measurements is excellent. The discrepancy is less than 3.0% almost everywhere. Figure 9 shows profiles of static temperature. The slight nonuniformity seen in these profiles reflects the large velocity change occurring over the free shear layer thickness in this flow of essentially constant stagnation enthalpy.

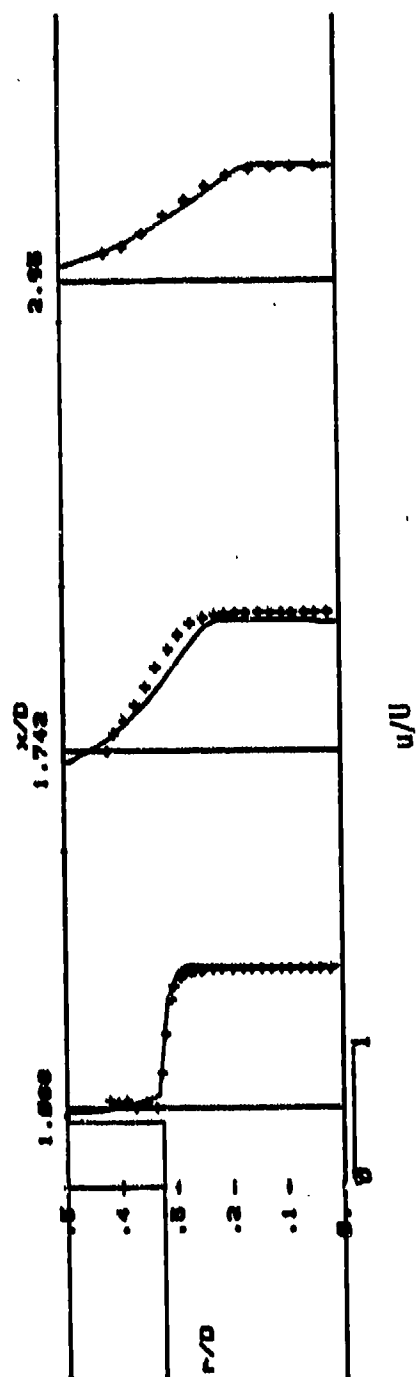


Figure 7. Predicted and measured dimensionless mean axial velocity showing the 34x30 QUICK solution (—) and Drewry's measurements (++++).

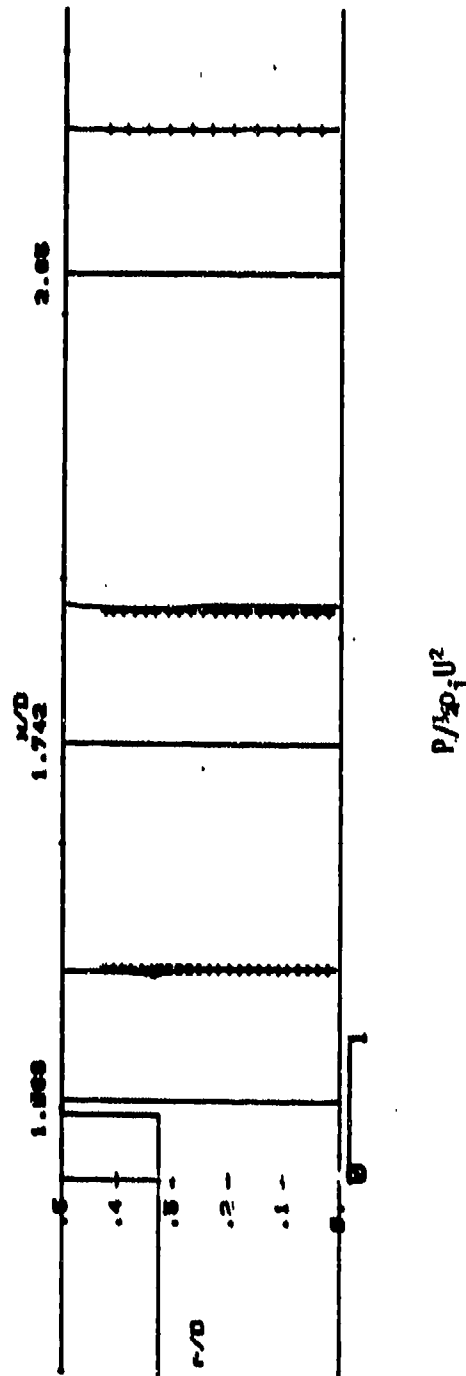


Figure 8. Predicted and measured dimensionless mean absolute pressure showing the 34x30 QUICK solution (—) and Drewry's measurements (++++).

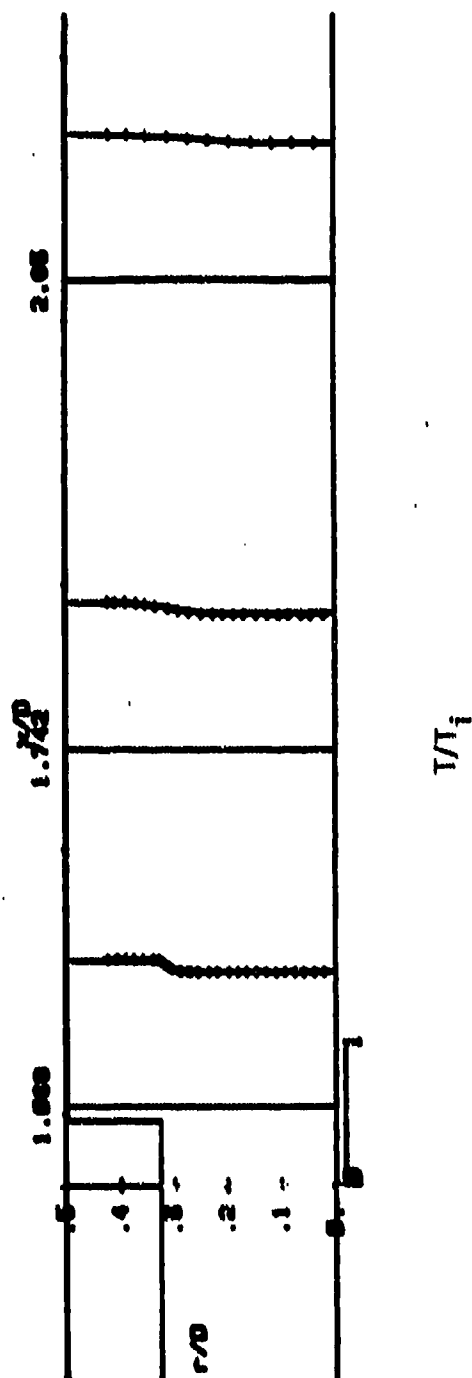


Figure 9. Predicted and measured dimensionless temperature showing the 34x30 QUICK solution (—) and Drewry's measurements (+++).

Excellent agreement with measurements is again obtained.

Predicted density profiles also exhibit this nonuniformity as shown in Fig. 10. Due to the inverse relationship between density and temperature, the radial gradient is opposite to that of temperature.

D. Prediction of Compressible Flow in a Concentric-Rotor Labyrinth Seal

The convergence rate and other operational characteristics of the two-dimensional (concentric-rotor) compressible flow code were evaluated via prediction of a generic labyrinth seal of the same geometry which was computed earlier for incompressible flow. This also serves to enhance one's insight into the compressible flow, eccentric-rotor flow field which produces the all-important rotordynamic forces. The configuration of the labyrinth seal considered is depicted in Fig. 11.

The seal configuration exhibits a cavity axial length $L=1.113$ mm, stator wall radius $R_s=42.89$ mm, tooth radial clearance $c=0.216$ mm, and radial distance from cavity base to stator wall $d=1.105$ mm. The shaft speed $\Omega=35,410$ rpm, the mean cavity inlet temperature $T=294.4^\circ\text{K}$, and the cavity inlet static pressure on the stator wall $P_{ow}=3.06 \times 10^2$ kPa (absolute). Results are presented for the case in which the cavity inlet Mach number $M_1=0.65$ using the tooth-clearance bulk axial velocity. Other dimensionless parameters are $Re_x \equiv 2Uc/\nu = 2.07 \times 10^4$ and $Ta \equiv (Wd/\nu)(d/r_{sh})^{1/2} = 4.16 \times 10^3$. Solutions were also obtained for inlet Mach number values of 0.2, 0.5, and 0.72 using the same inlet pressure, density, and temperature. Comparisons between the four solutions are discussed subsequently.

Measured distributions of compressible flow variables within a

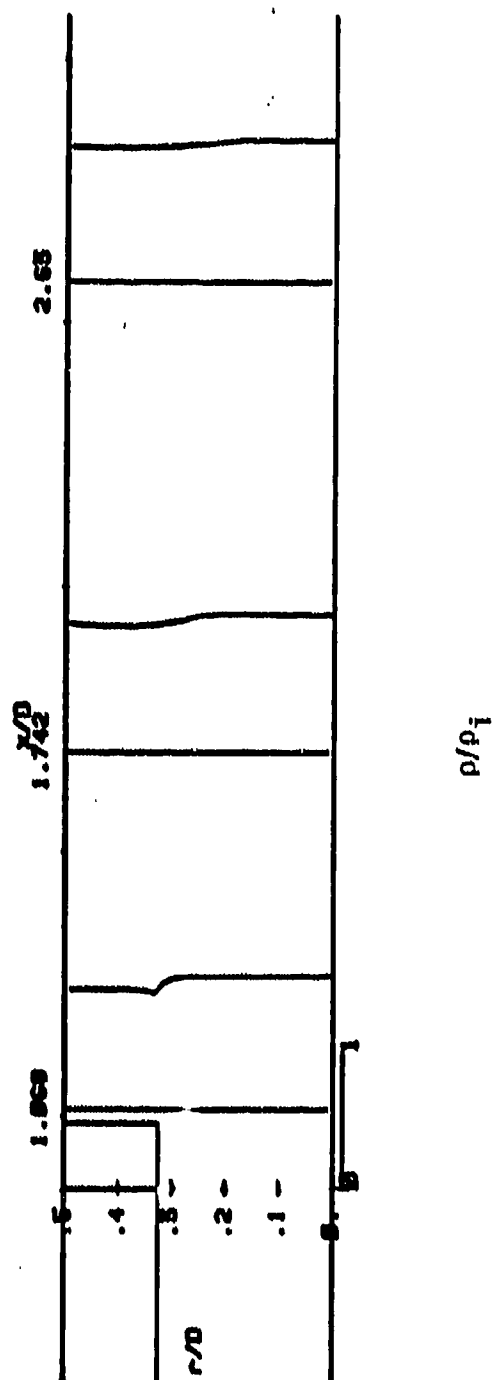


Figure 10. Predicted dimensionless density showing the 34x30 QUICK solution.

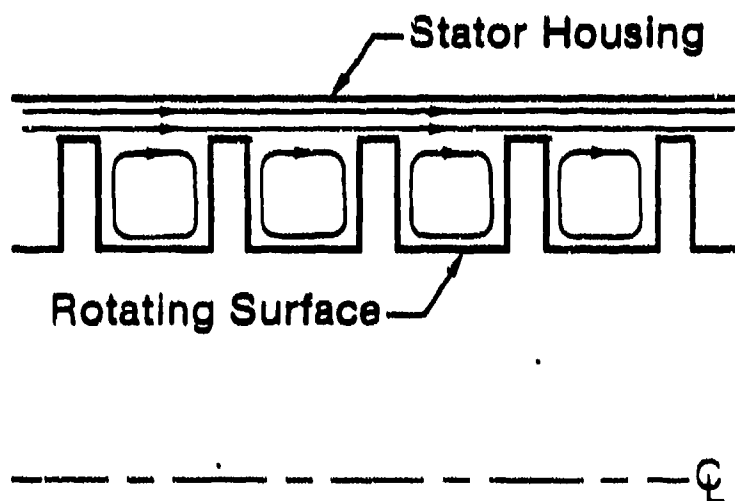


Figure 11. Configuration and expected streamline pattern for a generic, straight-through labyrinth seal.

labyrinth seal cavity are not yet available. For the previous incompressible flow results [10], these inlet profiles were calculated along with the solution by setting the inlet value of each variable (except pressure) equal to the corresponding outlet value at each numerical iteration. This was based on the assumption that the incompressible flow is streamwise periodic. However, this assumption is not valid for the present variable-density flow situations. For the present case, the dimensionless inlet profiles of the incompressible flow solution were adopted as the dimensionless inlet boundary values for compressible flow through the identical seal cavity.

Figures 12 through 17 exhibit predictions using a 33×31 grid employing the QUICK scheme. This arrangement was previously shown [10] to yield accurate solutions of the difference equations for the incompressible flow case. The convergence criteria for this study ranged as low as 0.1% for the normalized sum of residual source magnitudes.

Figure 12 shows the predicted dimensionless streamline pattern. The stream function is nondimensionalized by the leakage mass flow rate. The free shear layer emanating from the separation corner gives rise to the expected recirculation zone in the cavity. There is no indication from predictions that an additional small recirculation zone exists in the lower corners of the cavity near the base of each tooth.

Although streamline patterns for other M_1 cases are nearly identical, an interesting observation can be made from comparing Fig. 12 with streamline plots for $M_1=0.2$, 0.5, and 0.72. The recirculation strength as a percentage of leakage mass flow rate decreases slightly for increasing M_1 . This relative strength for the $M_1=0.2$ case is 40.2% and it steadily

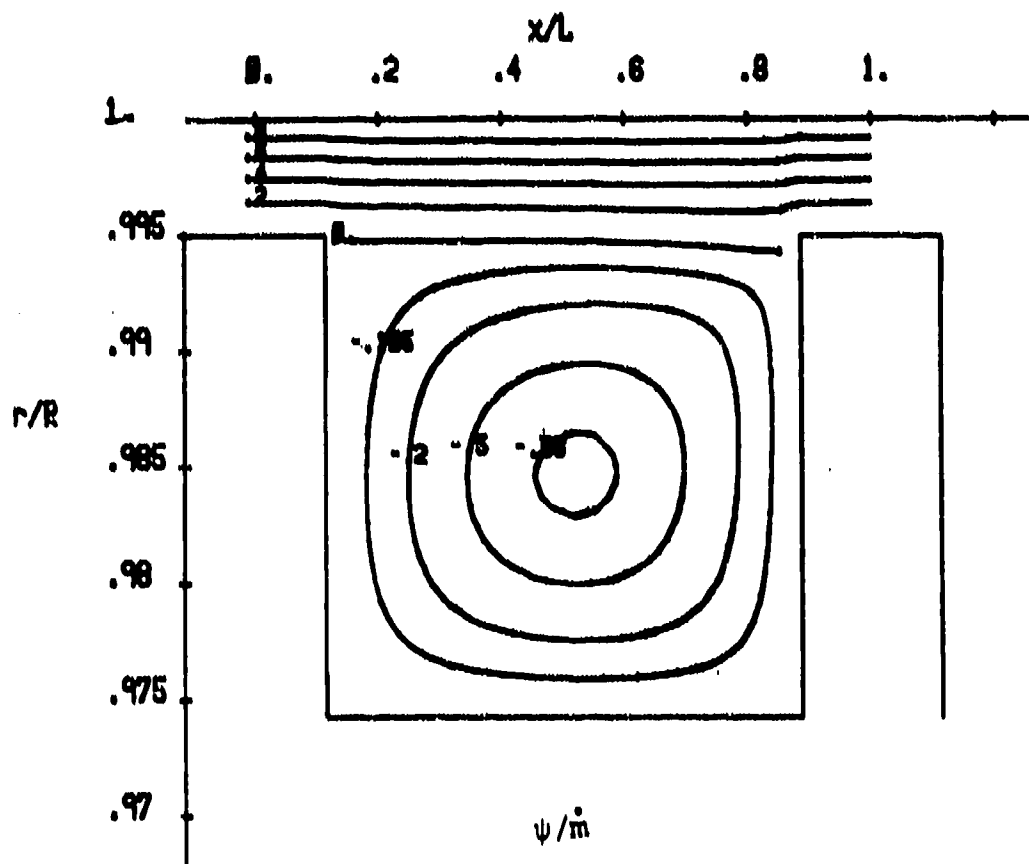


Figure 12. Predicted dimensionless streamline pattern for $M_1=0.65$.

decreases to 35.4% for $M_1=0.72$. For comparison, the flow of liquid hydrogen through the identical seal cavity at $Re_x=1 \times 10^6$ and $Ta=1.3 \times 10^5$ produces a recirculation strength of 39.0%.

The predicted radial profile plots pertain to the $M_1=0.65$ case and indicate numerous previously unavailable details. Corresponding results for other Mach number cases are very similar. One exception is a somewhat more pronounced variation in axial velocity and pressure for the higher M_1 cases in the region above the downstream tooth. Figure 13 shows axial velocity nondimensionalized by the cavity inlet bulk value $U=223.5$ m/s. The solution indicates the expected large value of $\partial u / \partial r$ near the separation corner. This reveals a high level of turbulence energy generation in this thin shear layer region.

For the higher M_1 cases, the large pressure decrease from inlet to outlet of the cavity yields a corresponding density decrease. This, in turn, results in a convective acceleration of the leakage flow in accordance with mass conservation. This effect is shown in Fig. 14 for each M_1 . As expected, this Mach number effect sharply increases with increasing M_1 .

The swirl velocity component is shown in Fig. 15 in which the shaft circumferential velocity is the nondimensionalizing factor. The distribution is nearly uniform at a value of 0.72. The corresponding liquid hydrogen case [10] exhibited uniform profiles with a value of 0.65. Not shown here are very sharp gradients near each surface.

Figure 16 shows the pressure distribution relative to the inlet stator wall pressure P_{ow} , which for this case is 3.06×10^5 Pa (absolute). It is normalized by the cavity inlet dynamic pressure. The pressure

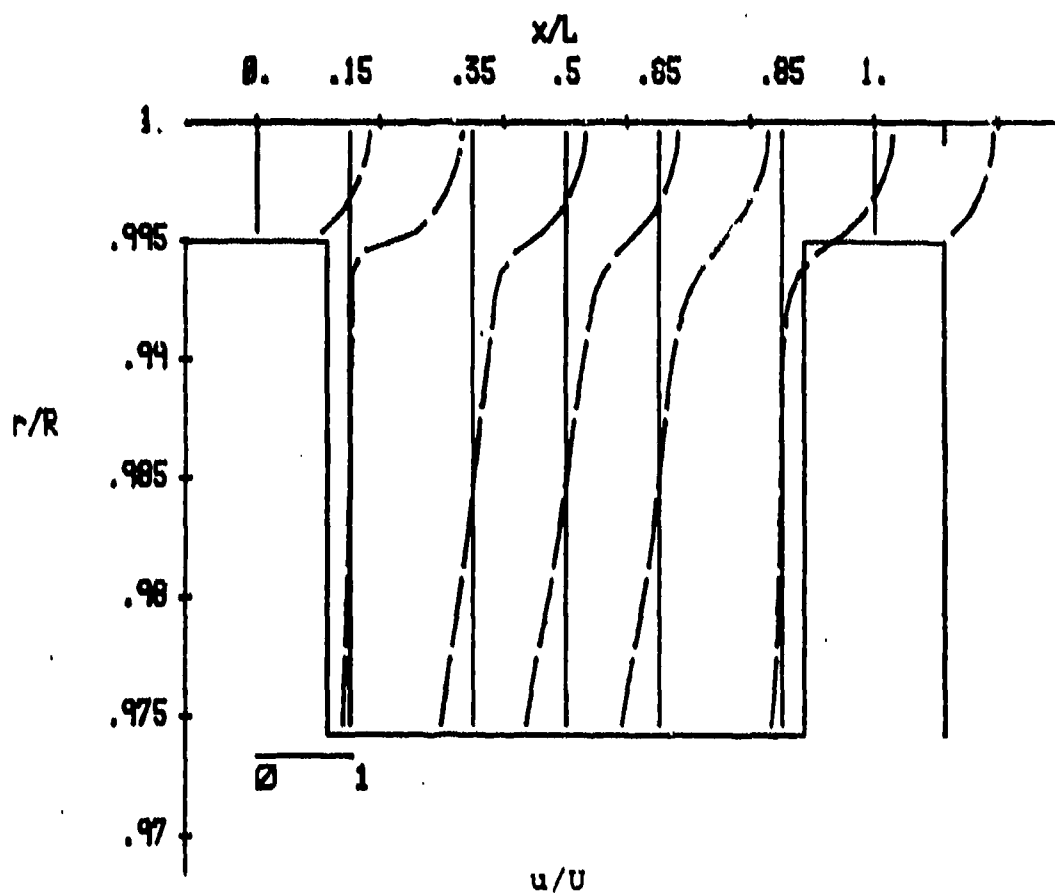


Figure 13. Predicted dimensionless mean axial velocity for $M_1=0.65$.

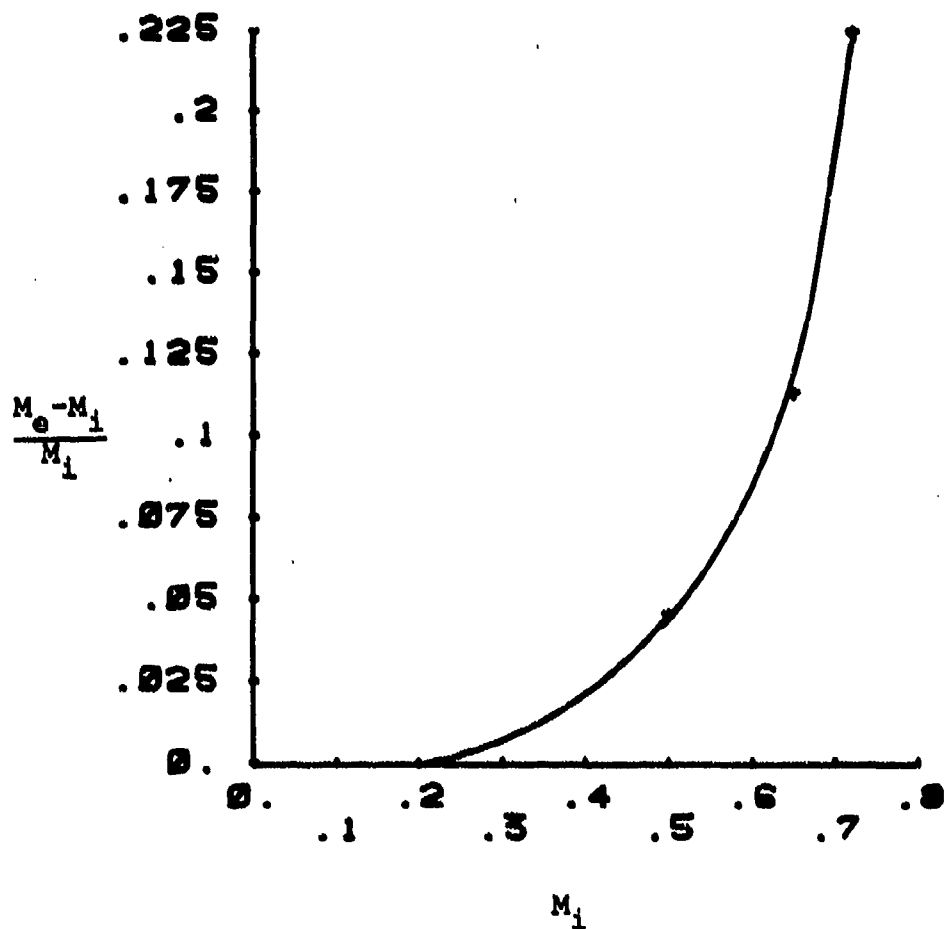


Figure 14. Predicted overall Mach number increase for the leakage flow through a single labyrinth seal cavity.

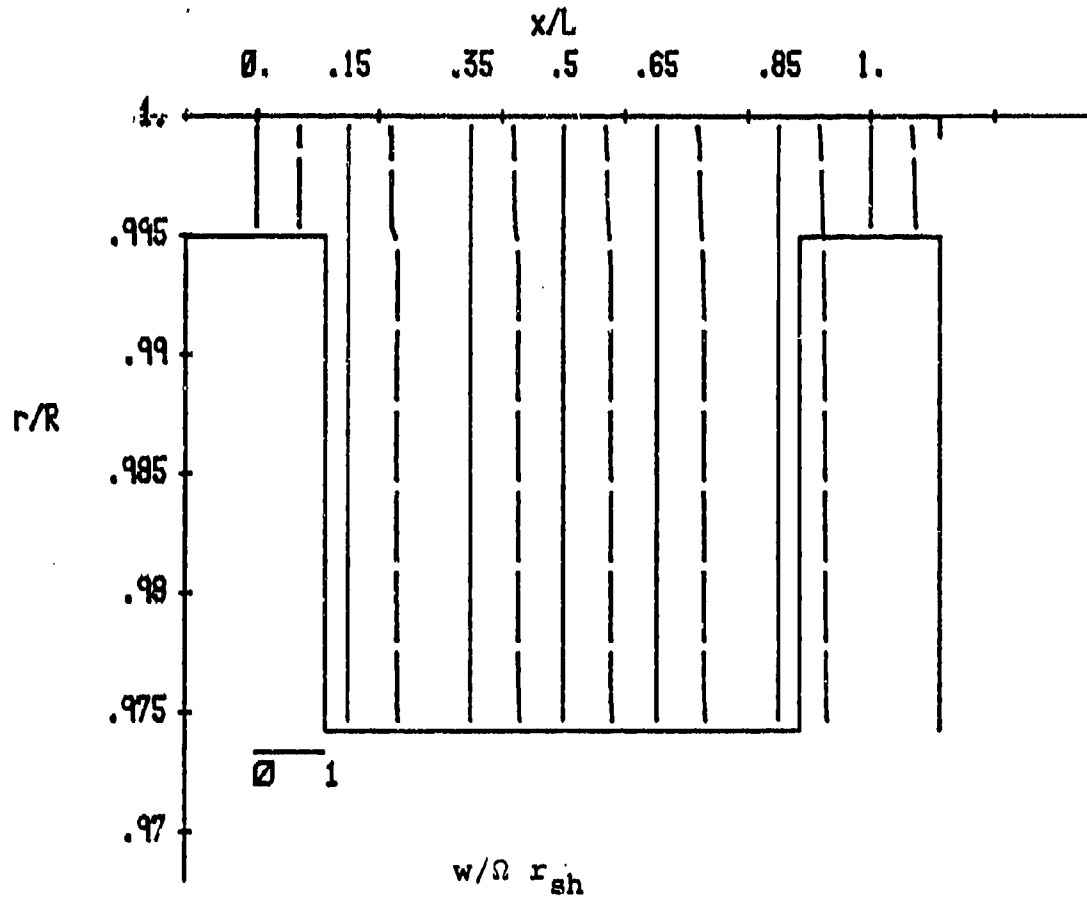


Figure 15. Predicted dimensionless mean swirl velocity for $M_1=0.65$.

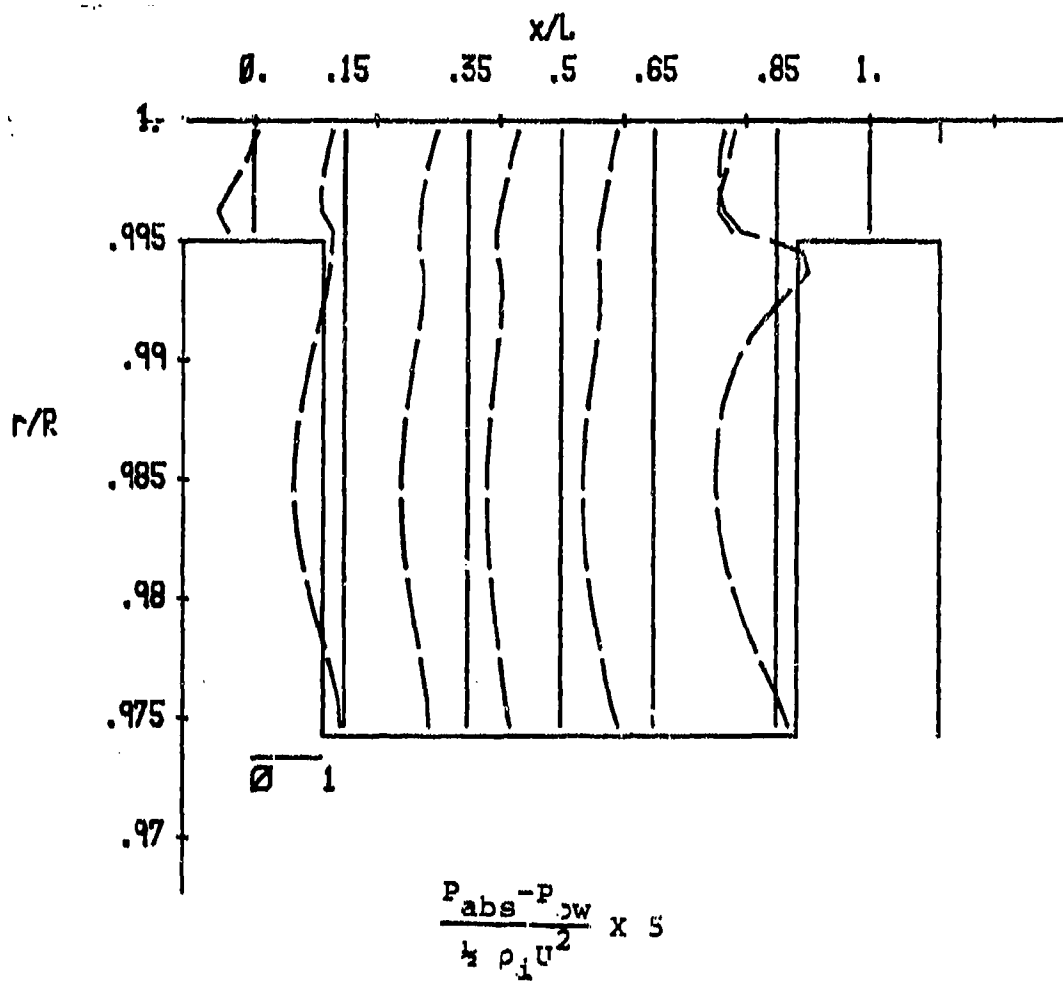


Figure 16. Predicted dimensionless mean relative pressure for $M_1 = 0.65$.

decreases slowly until $x/L=0.5$ and then increases slightly until approximately $x/L=0.75$. Finally, it decreases sharply as the flow accelerates over the downstream tooth. The sharp pressure peak observed at $x/L=0.85$ results from flow stagnation on the downstream tooth. For the given leakage flow rate, the overall bulk pressure drop across the cavity is approximately 3.5×10^4 Pa (0.34 atm).

Dimensionless turbulence kinetic energy is plotted in Fig. 17. As mentioned previously, it is the large value of $\partial u/\partial r$ in the free shear layer which produces intense turbulence energy in that region. This promotes the required large bulk pressure drop. As expected, the greatest turbulence energy value occurs near the stagnation point on the downstream tooth. The recirculation region effectively acts as a turbulence energy sink as the figure indicates a lack of turbulence generation there.

E. Eccentric-Rotor (3-D) Computer Code Development

The final major task in developing the required eccentric-rotor computer code entails the extension of the concentric-rotor compressible-flow code. This extension is conceptually straightforward and has been proceeding nicely. A three-dimensional computational mesh and corresponding storage arrays have been implemented. Also, numerous convective, diffusive, and source terms involving θ -derivatives have been appropriately incorporated into each of the governing equations. In addition, a 3-D iteration scheme has been included.

In accordance with objectives regarding the minimization of computational expense, numerous execution cost controls have been implemented. As previously mentioned, a major advancement in this

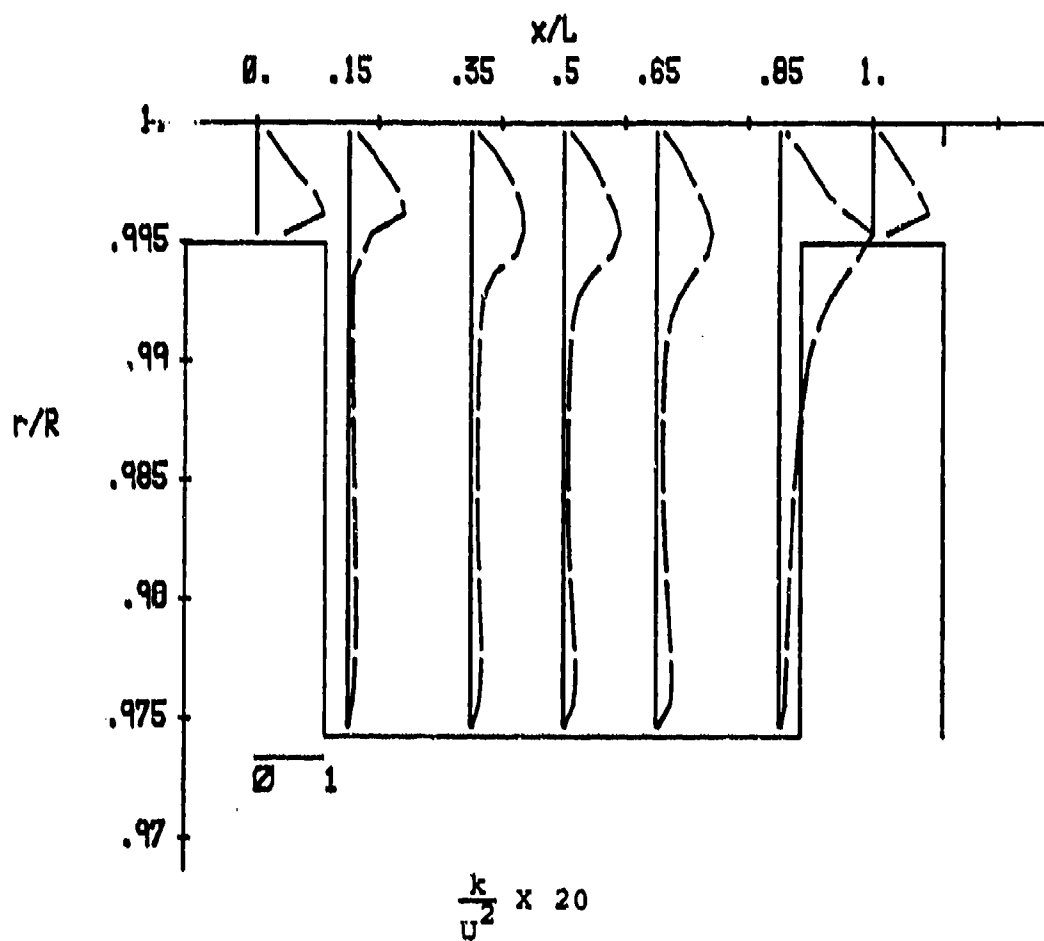


Figure 17. Predicted dimensionless turbulence kinetic energy for $M_1 = 0.65$.

regard is the incorporation of the QUICK differencing scheme in an original, and stabilizing manner, which has dramatically reduced the cost (via reduced grid density) required for necessary solution accuracy. This scheme was found to yield a 56% execution cost reduction for a concentric-rotor (2-D) case and will certainly provide considerably greater reductions for the all-important eccentric-rotor (3-D) cases of primary interest to engine manufacturers.

Several other cost reducing features are aimed at improving the convergence rate of the iterative solution procedures. Use of the well-known Cyclic Tri-Diagonal Matrix Algorithm as well as the SIMPLER solution approach allow fast convergence. Also, an advanced data input/output sequence has already provided substantial savings. It permits writing to and/or reading from disk/tape storage the current iteration level values at any desired interval. This allows the user, in the batch operating mode, to monitor solution progress, etc., and adjust the convergence rate parameters and then resume program execution.

F. Summary

Second year progress in developing the 3-D eccentric-rotor computer code included:

- (a) incorporation and evaluation of the QUICK differencing scheme to alleviate false diffusion errors and reduce execution costs,
- (b) evaluation of the 2-D concentric-rotor version via comparison with preliminary measurements of compressible flow through an abrupt pipe expansion,

- (c) brief exploratory predictions of compressible flow within a concentric-rotor labyrinth seal, and
- (d) partial completion of extending the highly successful concentric-rotor code to the required eccentric-rotor (3-D) version, including numerous execution cost saving features.

G. Graduate Student Development

Mr. Steve Sobolik continued employment during the second year of this project until June 1, 1984. He received a B.S. degree (Cum Laude) in Mechanical Engineering from TAMU in May 1982. He designed and developed software for Mitre Corp. (a NASA contractor) during three summers. Steve has been responsible for most of the computational development work on this project. He is an innovative individual and produces quality work. He was interviewed by numerous AFRAPT companies, and received an offer from Garrett Gas Turbine Engine Co. However, he accepted a more lucrative offer elsewhere.

Mr. Steve Hensel began employment on June 1, 1984, having received a B.S. degree (Cum Laude) in Nuclear Engineering from TAMU in May of 1984. Mr. Hensel is progressing admirably and is a self-motivated, innovative individual.

H. Publications

The manuscript, "Prediction of Incompressible Flow in Labyrinth Seals," was reviewed by the ASME Journal of Fluids Engineering. The manuscript will be revised slightly to comply with the reviewers' suggestions.

I. Conference Presentations

A paper consisting of the preliminary prediction test case of the sudden-expansion combustor flow field entitled: "Prediction of Subsonic Air Flow Through a Rocket/Ramjet Combustor" is accepted for presentation at the AIAA 23rd Aerospace Sciences Meeting. It will be held January 14 through 17, 1985 in Reno, Nevada. The authors are D. L. Rhode and S. R. Sobolik. Another paper consisting of the brief exploratory prediction of compressible flow in a concentric-rotor labyrinth seal is accepted for presentation at the 1985 ASME International Gas Turbine Conference. The title is: "Simulation of Subsonic Flow Through a Generic Labyrinth Seal." The conference is being held March 18 through 21, 1985 in Houston, Texas. In addition, an extended abstract for a third paper entitled: "Compressible Flow Prediction of an Axially-Staggered Labyrinth Seal," was submitted for the AIAA/ASME/SAE 21st Joint Propulsion Conference. It is to be held July 8 through 10, 1985 in Monterrey, California.

IV. REFERENCES

1. Childs, D., and Scharrer, J., "An Iwatsubo-Based Solution for Labyrinth Seals-Comparison to Experimental Results," presented at the Third Rotordynamic Workshop in High-Performance Turbomachinery, Texas A&M University, College Station, Texas 77843, also submitted for the 1985 ASME Gas Turbine Conference.
2. Iwatsubo, T., Matooka, N., and Kawai, R., "Flow Induced Force and Flow Pattern of Labyrinth Seals," NASA CP 2250 Proceedings of a workshop at Texas A&M University, 10-12 May 1982, Entitled Rotordynamic Instability Problems in High Performance Turbomachinery, pp. 205-222.
3. Wachter, J., and Bauckert, H., "Flow Induced Spring Coefficients of Labyrinth Seals for Applications in Rotordynamics," NASA CP 2250 Proceedings of a workshop at Texas A&M University, 10-12 May 1982, Entitled Rotordynamic Instability Problems in High Performance Turbomachinery, pp. 189-212.
4. Nicks, C. O., "A Comparison of Experimental and Theoretical Results for Leakage, Pressure Distribution, and Rotordynamic Coefficients for Annular Gas Seals," M.S. Thesis, Texas A&M University, September 1984.
5. Wyssman, H. R., Pham, T. C., and Jenny, R. J., "Predictions of Stiffness and Damping Coefficients for Centrifugal Compressor Labyrinth Seals," ASME Paper 84-GT-86, 29th International Gas Turbine Conference, Amsterdam, The Netherlands, June 1984.
6. Iwatsubo, T., "Evaluation of Instability Forces of Labyrinth Seals in Turbines or Compressors," NASA CP2133, Proceedings of a Workshop held at Texas A&M University entitled, "Rotordynamic Instability Problems on High-Performance Turbomachinery," 12-14 May 1980, pp. 139-167.

7. De Vahl Davis, G., and Mallinson, G. D., "An Evaluation of Upwind and Central Difference Approximations by a Study of Recirculating Flow," Computers and Fluids, Vol. 4, 1967, p. 29.
8. Leschziner, M. A., "On the Problem of Numerical Diffusion in First-Order Finite Difference Schemes Applied to Free Recirculating Flows," Proceedings of the 2nd GAMM Conference on Numerical Methods in Fluid Mechanics, Cologne, Federal Republic of Germany, 1977.
9. Leonard, B. P., "A Stable and Accurate Convective Modelling Procedure Based on Quadratic Upstream Interpolation," Comp. Maths. Appl. Mech. Eng., Vol. 19, 1979, pp. 59-98.
10. Rhode, D. L., Demko, J. A., Traegner, U. K., and Sobolik, S. R., "On the Prediction of Incompressible Flow in Labyrinth Seals," presented at the 7th Annual Energy-Sources Technology Conference, New Orleans, Louisiana, Feb. 12-16, 1984.
11. Rhode, D. L., Sobolik, S. R., and Traegner, U. K., "Prediction of Compressible Flow in Labyrinth Seals," 36th Annual Meeting of the American Physical Society, Nov. 20-22, 1983, Houston, Texas.
12. Drewry, James E., "Characterization of Sudden-Expansion Dump Combustor Geometries," AFAPL-TR-76-52, July 1976.

AN IWATSUBO-BASED SOLUTION FOR LABYRINTH SEALS

COMPARISON TO EXPERIMENTAL RESULTS

D. W. Childs* and J. K. Scharrer**
Texas A&M University
College Station, Texas 77843

SUMMARY

The basic equations are derived for compressible flow in a labyrinth seal. The flow is assumed to be completely turbulent in the circumferential direction where the friction factor is determined by the Blasius relation. Linearized zeroth and first-order perturbation equations are developed for small motion about a centered position by an expansion in the eccentricity ratio. The zeroth-order pressure distribution is found by satisfying the leakage equation while the circumferential velocity distribution is determined by satisfying the momentum equation. The first order equations are solved by a separation of variable solution. Integration of the resultant pressure distribution along and around the seal defines the reaction force developed by the seal and the corresponding dynamic coefficients. The results of this analysis are compared to published test results.

*Professor of Mechanical Engineering

**AFRAPT Graduate Research Trainee

INTRODUCTION

The problem of self excited vibration in turbomachinery due to labyrinth seals has led to the development of many analyses which attempt to model the physical phenomenon so that the problem can be better understood and therefore solved. The shortcoming with the analyses which have been presented to date is that they are difficult to understand and require limiting assumptions such as ignoring the area derivative in the circumferential direction, assuming that the friction factor is the same for all surfaces, and assuming that the flow coefficients is constant along the seal. These assumptions may be of some use mathematically, but do very little for the understanding of the physical occurrence. The first steps toward analysis of this problem were taken by Alford [1], who neglected circumferential flow and Spurk et al. [2] who neglected rotation of the shaft. Vance and Murphy [3] extended the Alford analysis by introducing a more realistic assumption of choked flow. Kostyuk [4] performed the first comprehensive analysis, but failed to include the change in area due to eccentricity which is responsible for the relationship between cross-coupled forces and parallel rotor displacements. Iwatsubo [5, 6] refined the Kostyuk model by including the time dependency of area change, but he neglected the area derivative in the circumferential direction. Kurohashi [7] incorporated dependency of the flow coefficient on eccentricity into his analysis, but assumed that the circumferential velocity in each cavity was the same.

The analysis presented here includes the variation of the area in the circumferential direction due to eccentricity and incorporates as

many of the physical phenomena in the flow field as was thought necessary to produce an adequate result. The main purpose of this paper is to present a unified and comprehensive derivation of a reduced set of equations and a new solution format for those equations. The results of this analysis are compared the published test results of Wachter and Benckert [8, 9, 10].

NOMENCLATURE

- A_1 : Cross sectional area of the cavity (L^2); defined in Eq. (1.a)
- B_1 : Height of labyrinth seal strip (L); defined in figure (1)
- C : Direct damping coefficient (Ft/L)
- C_r : Nominal radial clearance (L); defined in figure (1)
- D_h : Hydraulic diameter of cavity (L); introduced in Eq. (3)
- H : Local radial clearance (L)
- K : Direct stiffness coefficient (F/L)
- L : Pitch of seal strips (L); defined in figure (1)
- N_T : Number of seal strips
- $N_C = N_T - 1$: Number of cavities
- P : Pressure (F/L^2)
- R : Gas constant
- R_s : Radius of seal (L); defined in figure (1)
- T : Temperature (T)
- R_w : Surface velocity of rotor (L/t)
- V_1 : Average velocity of flow in circumferential direction (L/t)
- a, b : Radial seal displacement components due to elliptical whirl (L);
defined in Eq. (13)
- a_r : Dimensionless length upon which shear stress acts on rotor

a_s Dimensionless length upon which shear stress acts on stator
 c Cross coupled damping coefficient (Ft/L); in Eq. (18)
 k Cross coupled stiffness coefficient (F/L); in Eq. (18)
 \dot{m} Leakage mass flow rate per circumferential length (M/Lt)
 m_r, n_r, m_s, n_s Coefficients for Blasius relation for friction factor; defined in Eq. (3)
 t Time (t)
 ω Shaft angular velocity ($1/t$)
 ρ Density of fluid (M/L^3)
 ν Kinematic viscosity (L^2/t)
 $\epsilon = e/C_r$ Eccentricity ratio
 γ Ratio of specific heats
 K_Q^* Dimensionless cross-coupled stiffness parameter; defined in Eqs. (27)
 E_0^* Dimensionless entry swirl parameter; defined in Eqs. (27)

Subscripts

o Zeroth-order component
 i i -th chamber value
 1 First-order component
 x X-direction
 y Y-direction
 r Reservoir value
 s Sump value

PROCEDURE

The analysis presented here is developed for the see-through type of labyrinth seal shown in figure 1. The continuity and momentum equations will be derived for a single cavity control volume as shown in figures 2, 3, 4, and 5. A leakage model will be employed to account for the axial leakage. The governing equations will be linearized using perturbation analysis for small motion about a centered position. The zeroth-order continuity and momentum equations will be solved to determine the steady state pressure and velocity for each cavity. The first-order continuity and momentum equations will be reduced to linearly independent, algebraic equations by assuming an elliptical orbit for the shaft and a corresponding harmonic response for the pressure and velocity perturbations. The force and force coefficients for the seal are found by integration of the first-order pressure perturbation along and around the shaft.

ASSUMPTIONS

- 1) Fluid is considered to be an ideal gas.
- 2) Pressure variations within a chamber are small compared to the pressure difference across a seal strip.
- 3) The frequency of acoustic resonance in the cavity is much higher than that of the rotor speed.
- 4) Added mass terms are neglected.
- 5) The eccentricity of the rotor is small compared to the radial seal clearance.

- 6) In the determination of the shear stresses in the circumferential direction, the axial component of velocity is neglected.
- 7) The contribution of shear stress to the stiffness and damping coefficients is neglected.

GOVERNING EQUATIONS

Continuity Equation

Referring to the control volume in figures 2 and 3, the continuity equation for the control volume shown is:

$$\frac{\partial}{\partial t} (P_1 A_1) + \frac{\partial}{\partial \theta} \left(\frac{P_1 V_1 A_1}{R_s} \right) + \dot{m}_{1+1} - \dot{m}_1 = 0 \quad (1)$$

where the transverse surface area A_1 is defined by;

$$A_1 = (B_1 + H_1 + B_{1+1} + H_{1+1}) L_1 / 2 \quad (1.a)$$

Momentum Equation

The momentum equation (2) is derived using figures 4 and 5 which show the pressure forces and shear stresses acting on the control volume. This equation includes the area derivative in the circumferential direction, which was neglected by Iwatsubo [5, 6].

$$\begin{aligned} \frac{\partial P_1 V_1 A_1}{\partial t} + \frac{2 P_1 V_1 A_1}{R_s} \frac{\partial V_1}{\partial \theta} + \frac{\partial V_1^2}{R_s} + \frac{\partial A_1}{\partial \theta} \frac{V_1 A_1}{R_s} \frac{\partial P}{\partial \theta} \\ - \dot{m}_{1+1} V_1 - \dot{m}_1 V_{1-1} = - \frac{A_1}{R_s} \frac{\partial P_1}{\partial \theta} + \tau_{r1} a_{r1} L_1 - \tau_{s1} a_{s1} L_1 \end{aligned} \quad (2)$$

where a_r and a_s are the dimensionless length upon which the shear stresses act and are defined for teeth on rotor by

$$as_1 = 1 \quad ar_1 = (2B_1 + L_1) / L_1$$

and for teeth on the stator by

$$as_1 = (2B_1 + L_1) / L_1 \quad ar_1 = 1$$

Blasius [11] determined that the shear stresses for turbulent flow in a smooth pipe could be written as

$$S = \frac{1}{2} \rho U_m^2 n_o \left(\frac{U_m D_h}{\nu} \right)^{m_o}$$

where U_m is the mean flow velocity relative to the surface upon which the shear stress is acting. The constants m_o and n_o can be empirically determined for a given surface from pressure flow experiments. However, for smooth surfaces the coefficients given by Yamada [12] for turbulent flow between annular surfaces are:

$$m_o = -0.25 \quad n_o = 0.079$$

Applying Blasius' equation to the labyrinth rotor and stator surfaces yields the following definitions for the rotor and stator shear stresses.

$$\begin{aligned} \tau_{r1} &= \frac{\rho_1}{2} (Rw - V_1)^2 n_r \left[\frac{|Rw - V_1| D_{h1}}{\nu} \right]^{m_r} \text{sgn}(Rw - V_1) \\ \tau_{s1} &= \rho_1 \frac{V_1^2}{2} n_s \left[\frac{|V_1| D_{h1}}{\nu} \right]^{m_s} \text{sgn}(V_1) \end{aligned} \quad (3)$$

where D_{h1} is the hydraulic diameter defined by

$$D_{h1} = \frac{2(H_1 + B_1) L_1}{(H_1 + B_1 + L_1)} \quad (4)$$

Separate parameters (m_s , n_s), (m_r , n_r) for the stator and rotor, respectively, account for different rotor and stator roughnesses.

If Eq. (1) times the circumferential velocity is now subtracted from Eq. (2), the following reduced form of the momentum equation is obtained:

$$\rho_1 A_1 \frac{\partial V}{\partial t} + \rho_1 V_1 A_1 \frac{\partial V_1}{R_s \partial \theta} + \dot{m}_1 (V_1 - V_{1-1}) = \frac{-A_1}{R_s} \frac{\partial P}{\partial \theta} + \tau_{s1} n_{s1} L_1 + \tau_{r1} n_{r1} L_1 \quad (5)$$

In order to reduce the numbers of variables, all of the density terms are replaced with pressure terms using the ideal gas law.

$$P_1 = \rho RT \quad (6)$$

Furthermore, in order to make the perturbation analysis easier, the following substitution is made in the continuity equation:

$$\dot{m}_{1+1} - \dot{m}_1 = \frac{\dot{m}_{1+1}^2 - \dot{m}_1^2}{2\dot{m}_0}$$

Leakage Equation

To account for the leakage mass flow rate in the continuity and momentum equations, the leakage model of Neumann [13] was chosen. This model predicts leakage and pressures fairly accurately and has a term to account for kinetic energy carryover. However, the empirical flow coefficient relations given by Neumann were discarded in favor of the equations of Chaplygin

[14] for flow through an orifice. This was done to produce a different flow coefficient for succeeding contractions along the seal, as has been shown to be the case by Egli [15]. The form of the model is:

$$\dot{m}_1 = \mu_{11} \mu_2 H_1 \sqrt{\frac{P_{i-1}^2 - P_1^2}{RT}} \quad (7)$$

where the kinetic energy carryover coefficient μ_2 is defined for straight through seals as:

$$\mu_2 = \sqrt{\frac{NT}{(1-j)NT + j}}$$

where

$$j = 1 - (1 + 16.6 C_p/L)^{-2}$$

and is unity, by definition, for interlocking and combination groove seals. The flow coefficient is defined as:

$$\mu_{11} = \frac{\pi}{\pi + 2 - 5s_1 + 2s_1^2} \quad \text{where } s_1 = \left(\frac{P_{i-1}}{P_1} \right)^{\frac{\gamma-1}{\gamma}} - 1$$

For choked flow, Fliegner's formula [16] will be used for the last seal strip. It is of the form:

$$\dot{m}_{NC} = \frac{0.510 \mu_2}{\sqrt{RT}} P_{NC} H_{NT} \quad (8)$$

PERTURBATION ANALYSIS

For cavity 1, the continuity Eq. (1), momentum Eq. (5) and leakage Eq. (7) are the governing equations for the variables V_1 , P_1 , \dot{m}_1 . A perturbation analysis of these equations is to be developed with the eccentricity ratio, $\epsilon = e/Cr$, selected to be the perturbation parameter. The governing equations are expanded in the perturbation variables

$$\begin{aligned} P_1 &= P_{01} + \epsilon P_{11} & H_1 &= C_{r1} + \epsilon H_1 \\ V_1 &= V_{01} + \epsilon V_{11} & \Lambda_1 &= \Lambda_0 + \epsilon K H_1 \end{aligned}$$

where $\epsilon = e/Cr$ is the eccentricity ratio. The zeroth-order equations define the leakage mass flow rate and the circumferential velocity distribution for a centered position. The first-order equations define the perturbations in pressure and circumferential velocity due to a radial position perturbation of the rotor. Strictly speaking, the results are only valid for small motion about a centered position.

Zeroth-Order Solution

The zeroth-order leakage equation is

$$\dot{m}_1 + \dot{m}_1 = \dot{m}_1 = \dot{m}_0 \quad (9)$$

and is used to determine both the leakage-rate \dot{m}_0 and pressure distribution for a centered position. The leakage rate is determined using either Eq. (7) or Eq. (8), depending on the operating conditions. To determine if the flow is choked or not, assume that the pressure in

the last cavity is equal to the critical pressure for choking. Using this pressure, find the leakage from Eq. (8) and then use Eq. (7) to determine the reservoir pressure necessary to produce this condition. Based on this pressure, a determination can be made whether the flow is choked or not. The associated pressure distribution is determined by employing the calculated leakage, along with a known boundary pressure, and solving Eq. (7) sequentially for each cavity pressure P_{oi} .

The zeroth-order circumferential-momentum equation is

$$\dot{m}_o (V_{oi} - V_{oi-1}) = (\tau_{rio} a_{ri} - \tau_{sio} a_{si}) L_i \quad i = 1, 2, \dots, NC,$$

From calculated pressures, the densities can be calculated at each cavity from Eq. (6), and the only unknowns remaining in Eq. (10) are the circumferential velocities V_{oi} . Given an inlet tangential velocity, a Newton-root-finding approach can be used to solve Eq. (10) for the i -th velocity, one cavity at a time. This is done starting at the first cavity and working down stream.

First-Order Solution

The governing first-order equations (11, 12), define the pressure and velocity fluctuations resulting from the seal clearance function. The continuity equation (11) and momentum equation (12) follow:

$$G_{1i} \frac{\partial P_{1i}}{\partial t} + G_{1i} \frac{V_{oi}}{R_s} \frac{\partial P_{1i}}{\partial \theta} + G_{1i} \frac{P_{oi}}{R_s} \frac{\partial V_{1i}}{\partial \theta} + G_{3i} P_{1i} + G_{4i} P_{1i-1} + G_{5i} P_{1i+1} = -G_{6i} H_1 - G_{2i} \frac{\partial H_1}{\partial t} - G_{2i} \frac{V_{oi}}{R_s} \frac{\partial H_1}{\partial \theta}$$

$$X_{1i} \frac{\partial V_{1i}}{\partial t} + \frac{X_{1i} V_{oi}}{R_s} \frac{\partial V_{1i}}{\partial \theta} + \frac{A_{oi}}{R_s} \frac{\partial P_{1i}}{\partial \theta} + X_{2i} V_{1i} - \dot{m}_o V_{1i-1} + X_{3i} P_{1i} \quad (12)$$

$$+ X_{4i} P_{1i-1} = X_{5i} H_1$$

where the X_1 's and G_1 's are defined in Appendix A. If the shaft center moves in an elliptical orbit, then the seal clearance function can be defined as:

$$\begin{aligned} eH_1 &= -a \cos \omega t \cos \theta - b \sin \omega t \sin \theta \\ &= -\frac{a}{2} [\cos(\theta - \omega t) + \cos(\theta + \omega t)] - \frac{b}{2} [\cos(\theta - \omega t) - \cos(\theta + \omega t)] \end{aligned} \quad (13)$$

The pressure and velocity fluctuations can now be stated in the associated solution format:

$$P_{1i} = P_{0i}^+ \cos(\theta + \omega t) + P_{si}^+ \sin(\theta + \omega t) + P_{0i}^- \cos(\theta - \omega t) + P_{si}^- \sin(\theta - \omega t) \quad (14)$$

$$V_{1i} = V_{0i}^+ \cos(\theta + \omega t) + V_{si}^+ \sin(\theta + \omega t) + V_{0i}^- \cos(\theta - \omega t) + V_{si}^- \sin(\theta - \omega t) \quad (15)$$

Substituting Eqs. (13), (14), and (15) into Eqs. (11) and (12) and grouping like terms of sines and cosines (as shown in Appendix B) eliminates the time and theta dependency and yields eight linear algebraic equations per cavity. The resulting system of equations of the i -th cavity is of the form:

$$[A_{i-1}] (X_{i-1}) + [A_i] (X_i) + [A_{i+1}] (X_{i+1}) = \frac{a}{c} (B_i) + \frac{b}{c} (C_i) \quad (16)$$

where

$$(X_{i-1}) = (P_{si-1}^+, P_{0i-1}^+, P_{si-1}^-, P_{0i-1}^-, V_{si-1}^+, V_{0i-1}^+, V_{si-1}^-, V_{0i-1}^-)^T$$

$$(X_i) = (P_{si}^+, P_{0i}^+, P_{si}^-, P_{0i}^-, V_{si}^+, V_{0i}^+, V_{si}^-, V_{0i}^-)^T$$

$$(X_{i+1}) = (P_{si+1}^+, P_{0i+1}^+, P_{si+1}^-, P_{0i+1}^-, V_{si+1}^+, V_{0i+1}^+, V_{si+1}^-, V_{0i+1}^-)^T$$

The A matrices and column vectors B and C are given in Appendix B. To use Eq. (16) for the entire seal solution, a system matrix must be formed which is block tridiagonal in the A matrices. The size of this resultant matrix is $(cNC \times cNC)$ since pressure and velocity

perturbations at the inlet and the exit are assumed to be zero. This system is easily solved by various linear equation algorithms, and yields a solution of the form:

$$\begin{aligned}
 P_{s1}^+ &= \frac{a}{c} F_{as1}^+ + \frac{b}{c} F_{bs1}^+ \\
 P_{s1}^- &= \frac{a}{c} F_{as1}^- + \frac{b}{c} F_{bs1}^- \\
 P_{o1}^+ &= \frac{a}{c} F_{ao1}^+ + \frac{b}{c} F_{bo1}^+ \\
 P_{o1}^- &= \frac{a}{c} F_{ao1}^- + \frac{b}{c} F_{bo1}^-
 \end{aligned} \tag{17}$$

DETERMINATION OF DYNAMIC COEFFICIENT

The force-motion equations for a labyrinth seal are assumed to be of the form:

$$\begin{bmatrix} F_x \\ F_y \end{bmatrix} = \begin{bmatrix} -K & k \\ -k & K \end{bmatrix} \begin{bmatrix} X \\ Y \end{bmatrix} + \begin{bmatrix} C & 0 \\ -0 & C \end{bmatrix} \begin{bmatrix} \dot{X} \\ \dot{Y} \end{bmatrix} \tag{18}$$

The solution of Eq. (18) for the stiffness and damping coefficients is the objective of the current analysis. For the assumed elliptical orbit of Eq. (13), the X and Y components of displacement and velocity are defined as:

$$\begin{aligned}
 X &= a \cos \omega t & \dot{X} &= -a\omega \sin \omega t \\
 Y &= b \sin \omega t & \dot{Y} &= b\omega \cos \omega t
 \end{aligned}$$

Substituting these relations into (18) yields:

$$\begin{aligned}
 +F_x &= -K_a \cos \omega t - k_b \sin \omega t + C_a \omega \sin \omega t - C_b \omega \cos \omega t \\
 +F_y &= -k_a \cos \omega t - K_b \sin \omega t - C_a \omega \sin \omega t - C_b \omega \cos \omega t
 \end{aligned} \tag{19}$$

Redefining the forces, F_x and F_y , as the following:

$$F_x = F_{x0} \cos \omega t + F_{xs} \sin \omega t \quad (20)$$

$$F_y = F_{y0} \cos \omega t + F_{ys} \sin \omega t$$

and substituting back into (19) yields the following relations:

$$-F_{x0} = K_a + c b \omega \quad -F_{xs} = -C_a X + k b \quad (21)$$

$$-F_{y0} = k_a + C b \omega \quad -F_{ys} = K_b + c a \omega$$

The X and Y components of force can be found by integrating the pressure around the seal as follows:

$$F_x = -R a c \sum_{i=1}^{NC} \int_0^{2\pi} P_{i1} L_1 \cos \theta \, d\theta \quad (22)$$

$$F_y = R a c \sum_{i=1}^{NC} \int_0^{2\pi} P_{i1} L_1 \sin \theta \, d\theta \quad (23)$$

Only one of these components needs to be expanded in order to determine the dynamic coefficients. For this analysis, the X component was chosen. Substituting Eq. (14) into (22) and integrating yields:

$$F_x = -c a R a \sum_{i=1}^{NC} L_1 [(P_{s1}^+ - P_{s1}^-) \sin \omega t + (P_{o1}^+ + P_{o1}^-) \cos \omega t] \quad (24)$$

substituting from Eq. (17) and (19) into Eq. (24) and equating coefficients of $\sin \omega t$ and $\cos \omega t$ yields:

$$F_{xs} = -\pi R a \sum_{i=1}^{NC} L_1 [a(F_{as1}^+ - F_{as1}^-) + b(F_{bs1}^+ - F_{bs1}^-)] \quad (25)$$

$$F_{x0} = -\pi R a \sum_{i=1}^{NC} L_1 [a(F_{ao1}^+ + F_{ao1}^-) + b(F_{bo1}^+ + F_{bo1}^-)]$$

Equating the definitions for F_{xs} and F_{xo} provided by Eqs. (21) and (25) and grouping like terms of the linearly independent coefficients a and b yields the final solutions to the stiffness and damping coefficients:

$$\begin{aligned} K &= \pi R \sum_{i=1}^{NC} (F_{aoi}^+ + F_{aoi}^-) L_i \\ k &= \pi R \sum_{i=1}^{NC} (F_{bsoi}^+ - F_{bsoi}^-) L_i \\ C &= \frac{-\pi R s}{\omega} \sum_{i=1}^{NC} (F_{aso i}^+ - F_{aso i}^-) L_i \\ o &= \frac{\pi R s}{\omega} \sum_{i=1}^{NC} (F_{bso i}^+ + F_{bso i}^-) L_i \end{aligned} \quad (26)$$

SOLUTION PROCEDURE SUMMARY

In review, the solution procedure uses the following sequential steps:

- a) Leakage is determined from Eq. (7) or (8).
- b) Pressure distribution is found using Eq. (7).
- c) Velocity distribution is determined using Eq. (10).
- d) A system equation is formed and solved using the cavity Eq. (16).
- e) Results of this solution, as defined in Eqs. (17), are inserted into Eq. (26).

RESULTS

To compare the present analytic solution with the experimental results of Wachter and Beckert [8, 9, 10], the following dimensionless

parameters are introduced. The dimensionless cross-coupled stiffness and entry-swirl parameters are defined by Wachter and Benckert as:

$$K_Q^* = \frac{Cr K_{xy}}{ReLNT(Pr-Ps)} \quad E_0^* = \frac{0.5\rho_0 V^2 a}{(Pr-Ps) + 0.5\rho_0 V^2 x} \quad (27)$$

All of the results presented for comparison in this paper are for a seal with teeth on the stator, with entry swirl, and no shaft rotation. Although Wachter and Benckert published results for shaft rotation, the data for the operating conditions and seal geometry were insufficient for use in this study. The results in figures 7, 8, and 9 are from [8] and show the relationship between cross coupled stiffness and the entry swirl, for a seal with strips on the stator and the geometry shown in figure 6. The line shown is the experimental result and the symbols are the results from this analytical model. These figures show that the model compares favorably to the experimental results in magnitude and the overall trend for various operating conditions. The figures also show that the model does not yield a consistently high or low result. Instead, the model tends to over predict the value of the stiffness for a large number of strips and under predict stiffness for a small number of seals. This trend is probably due to errors in calculating the zeroth-order pressure distribution using the leakage model.

The results in table (1) are from [9, 10] for a seal with strips on the stator. The results show the effect of change in seal parameters such as pitch, number of teeth, radius, strip height, and clearance on the cross coupled stiffness. The model accurately shows the increase in cross-coupled stiffness due to decrease in clearance

and decrease in strip height, but it fails to remain constant for change of pitch and consistently over estimates the cross-coupled stiffness for the larger radius cases by about 26%.

CONCLUSION

A clear and understandable analysis utilizing reduced equations has been presented for the problem of calculating rotordynamic coefficients for labyrinth seals. This paper was developed to provide a less restrictive analysis and a better explanation of the current analyses. The model developed gives results that are within 25% of the experimental results which are available. However, this error must be balanced against the known uncertainties in the experimental data. This is especially important since all of the data used are for a nonrotating shaft and the only influence on the cross coupled stiffness was the entry swirl. Although Wachter and Benckert published data for a rotating shaft, the data were not sufficient to calculate a result. Also, the only data available for see-through labyrinths is for the type with strips on the stator. For a more rigorous test of this and other models, more complete data are required over a wider range of parameters for different seal geometries. Finally, this analysis is only considered valid for the see-through type of labyrinth seal since the model fared very poorly in comparison with experimental results for interlocking and grooved seal data.

REFERENCES

1. Alford, J. S., "Protecting Turbomachinery from Self-Excited Rotor Whirl," Transactions ASME J. of Engineering for Power, October 1965, pp. 333-344.
2. Spurk, J. H., and Keiper, R., "Selbsterregte Schwingungen bei Turbomaschinen infolge der Labyrinthströmung," Ingenieur-Archive 43, 1974, pp. 127-135.
3. Vance, J. M., and Murphy, B. T., "Labyrinth Seal Effects on Rotor Whirl Stability," Inst. of Mechanical Engineer, 1980, pp. 369-373.
4. Kostyuk, A. G., "A Theoretical Analysis of the Aerodynamic Forces in the Labyrinth Glands of Turbomachines," Teploenergetika, 19 (11)0, 1972, pp. 39-44.
5. Iwatsubo, T., "Evaluation of Instability Forces of Labyrinth Seals in Turbines or Compressors," NASA CP 2133 Proceedings of a workshop at Texas A&M University 12-14 May 1980, Entitled Rotordynamic Instability Problems in High Performance Turbomachinery, pp. 139-167.
6. Iwatsubo, T., Matooka, N., and Kawai, R., "Flow Induced Force and Flow Pattern of Labyrinth Seal," NASA CP 2250 Proceedings of a workshop at Texas A&M University 10-12 May 1982, Entitled Rotordynamic Instability Problems in High Performance Turbomachinery, pp. 205-222.
7. Kurohashi, M., Inoue, Y., Abe, T., and Fujikawa, T., "Spring and Damping Coefficients of the Labyrinth Seal," Paper No. C283/80 delivered at the Second International Conference on Vibrations in Rotating Machinery, The Inst. of Mech. Engineering.
8. Wachter, J., and Benckert, H., "Querkraft aus Spaltdichtungen-Eine mögliche Ursache für die Laufunruhe von Turbomaschinen," Atomkernenergie Bd. 32, 1978, Lfg. 4, pp. 239-246.
9. Wachter, J., and Benckert, H., "Flow Induced Spring Coefficients of Labyrinth Seals for Applications in Rotordynamics," NASA CP 2133 Proceedings of a workshop held at Texas A&M University 12-14 May 1980, Entitled Rotordynamic Instability Problems of High Performance Turbomachinery, pp. 189-212.
10. Benckert, H., "Stromungsbedingte Federkennwerte in Labyrinthdichtungen," Doctoral dissertation at University of Stuttgart, 1980.
11. Blasius, H., "Forschungsarb," Ing.-Wes., No 131, 1913.
12. Yamada, Y., Trans. Japan Soc. Mechanical Engineers, Vol. 27, No. 180, 1961, pp. 1267.

13. Neumann, K., "Zur Frage der Verwendung von Durchblickdichtungen im Dampfturbinenbau," Maschinentechnik, Vol. 13, 1964, No 4.

14. Gurevich, M. I., The Theory of Jets In An Ideal Fluid, Pergamon Press, 1966, pp. 319-323.

15. Egli, A., "The Leakage of Steam Through Labyrinth Glands," Trans. ASME, Vol. 57, 1935, pp. 115-122.

16. John, E. A. James, Gas Dynamics, Wiley, 1979.

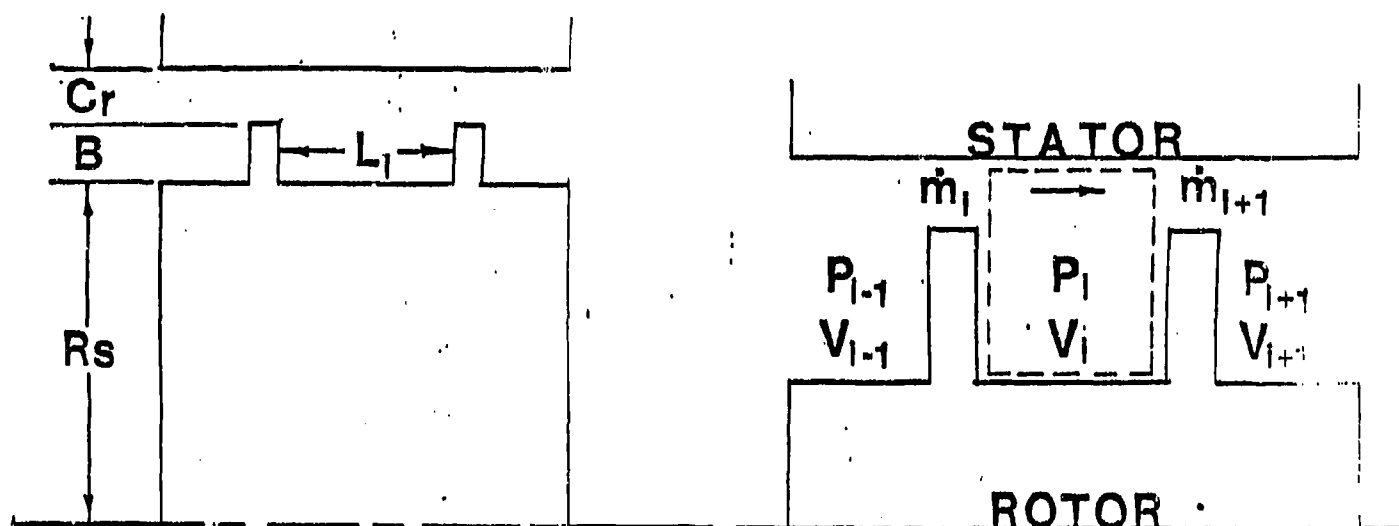


Figure 1
A Typical Cavity

Figure 2
Cavity Control Volume

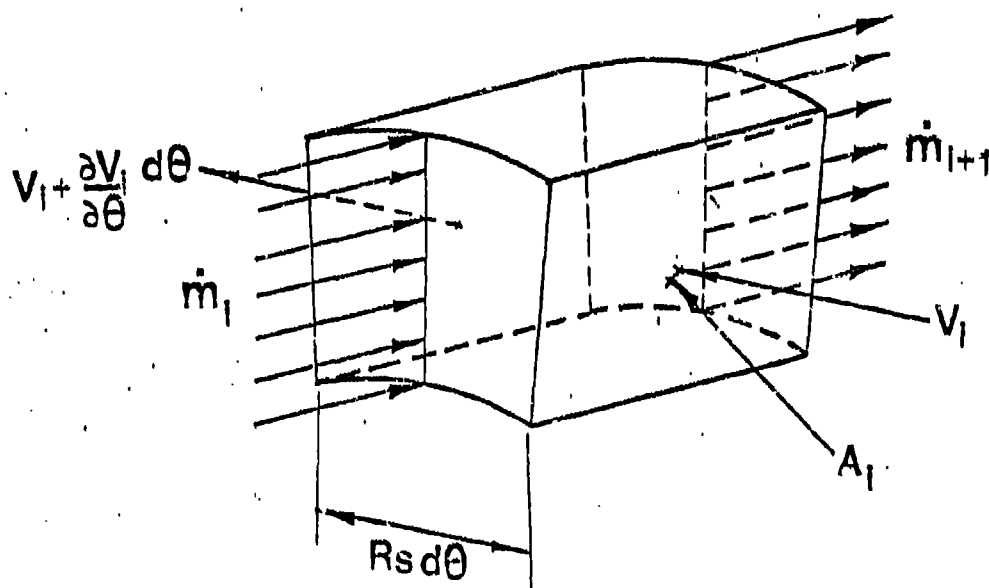


Figure 3
Cavity Control Volume

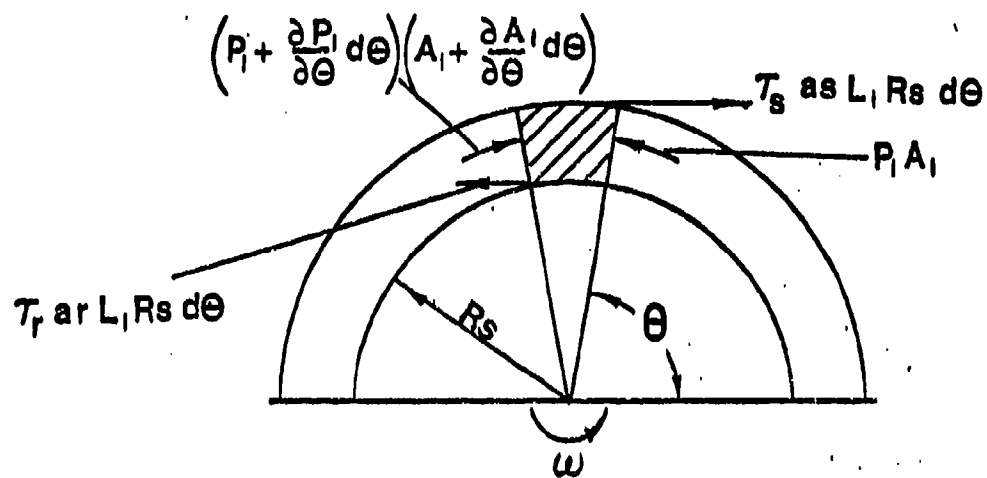


Figure 4
Forces on Control Volume

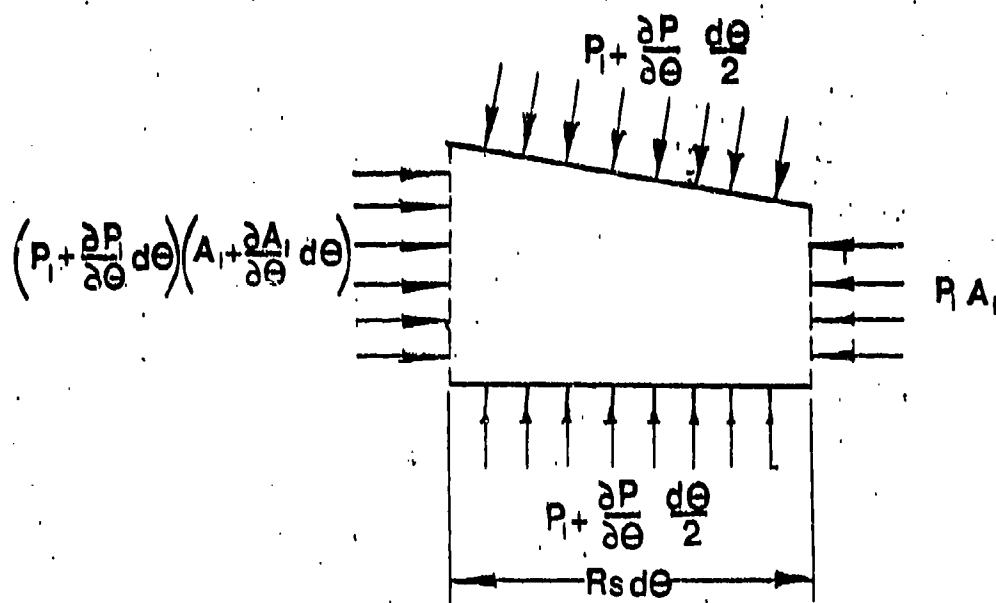


Figure 5
Forces on Control Volume

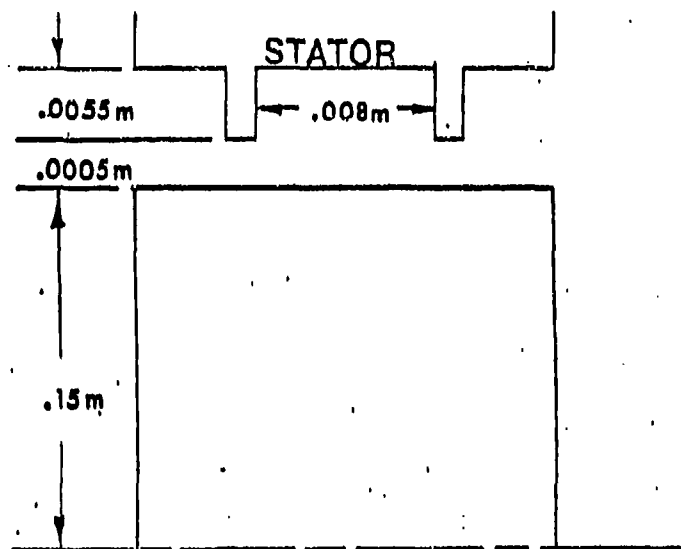


Figure 6
Configuration used for experiment

* E ₀	U	NT	C(m)	L(m)	B(m)	Rs(m)	P _r (bar)	P _s (bar)	EXP. K _{xy} (N/mm)	CALC. K _{xy} (N/mm)	% Error
0.023	0.0	18	.00025	.005	.0025	0.15	2.947	0.943	257	233	-9
0.024	0.0	18	.00025	.005	.0025	0.15	1.43	0.943	75	69	-8
0.038	0.0	18	.00025	.005	.006	0.15	2.947	0.943	157	142	-10
0.018	0.0	18	.00025	.005	.006	0.15	1.43	0.943	27	26	-4
0.04	0.0	18	.00058	.005	.006	0.075	1.925	0.943	29	20	-31
0.04	0.0	18	.00058	.005	.006	0.075	2.418	0.943	41	28	-32
0.04	0.0	9	.00058	.010	.006	0.075	1.925	0.943	29	16	-45
0.04	0.0	9	.00058	.010	.006	0.075	2.418	0.943	41	23	-44

Table 1. Comparison of data for various geometries operating conditions for a seal with teeth on the stator and no shaft rotation. [9, 10]

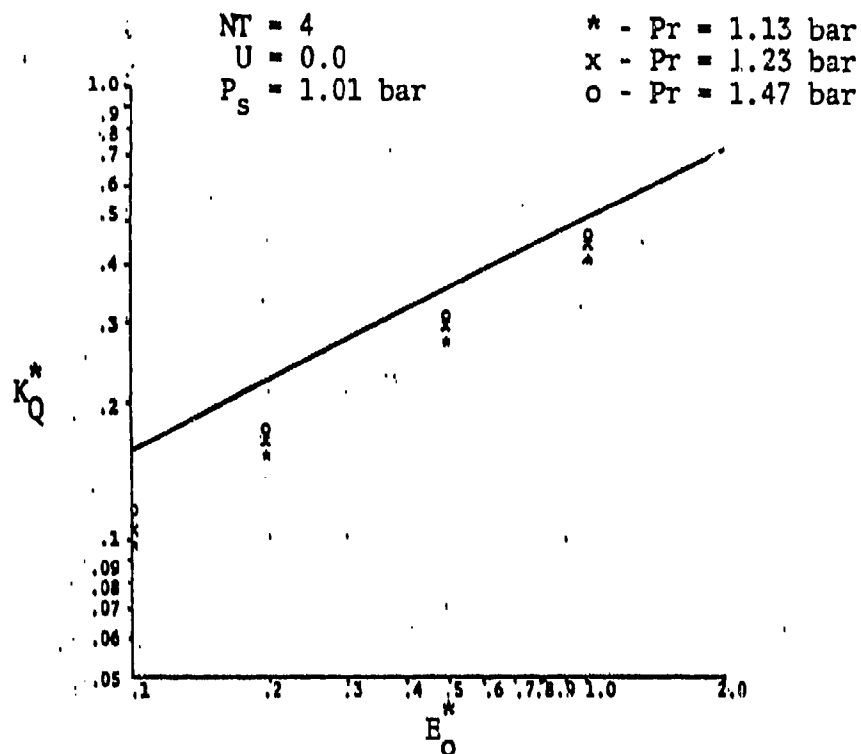


Figure 7. Comparison to data of [8] for seal in figure 6.

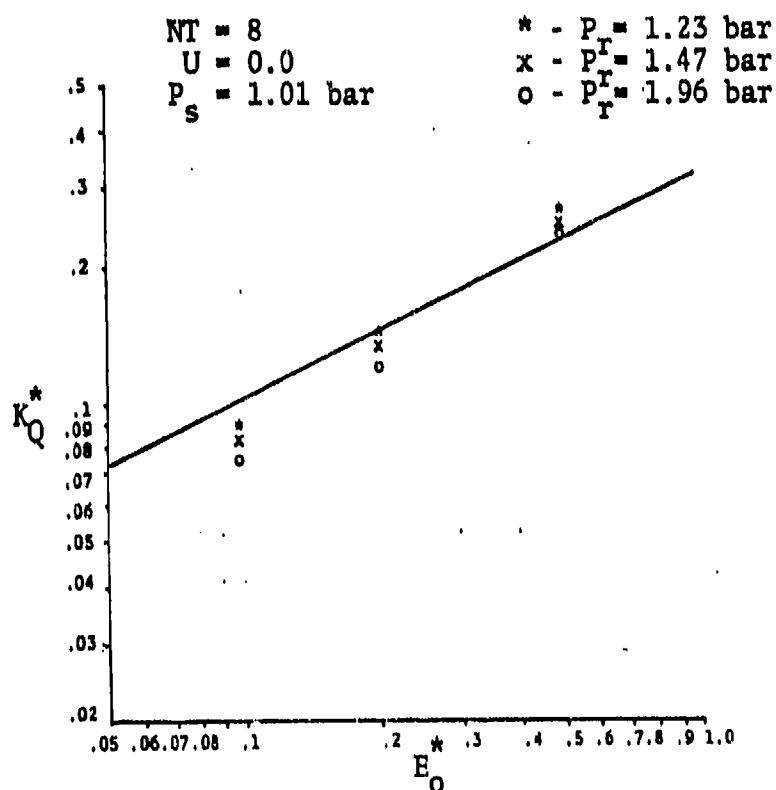


Figure 8. Comparison to data of [8] for seal in figure 6.

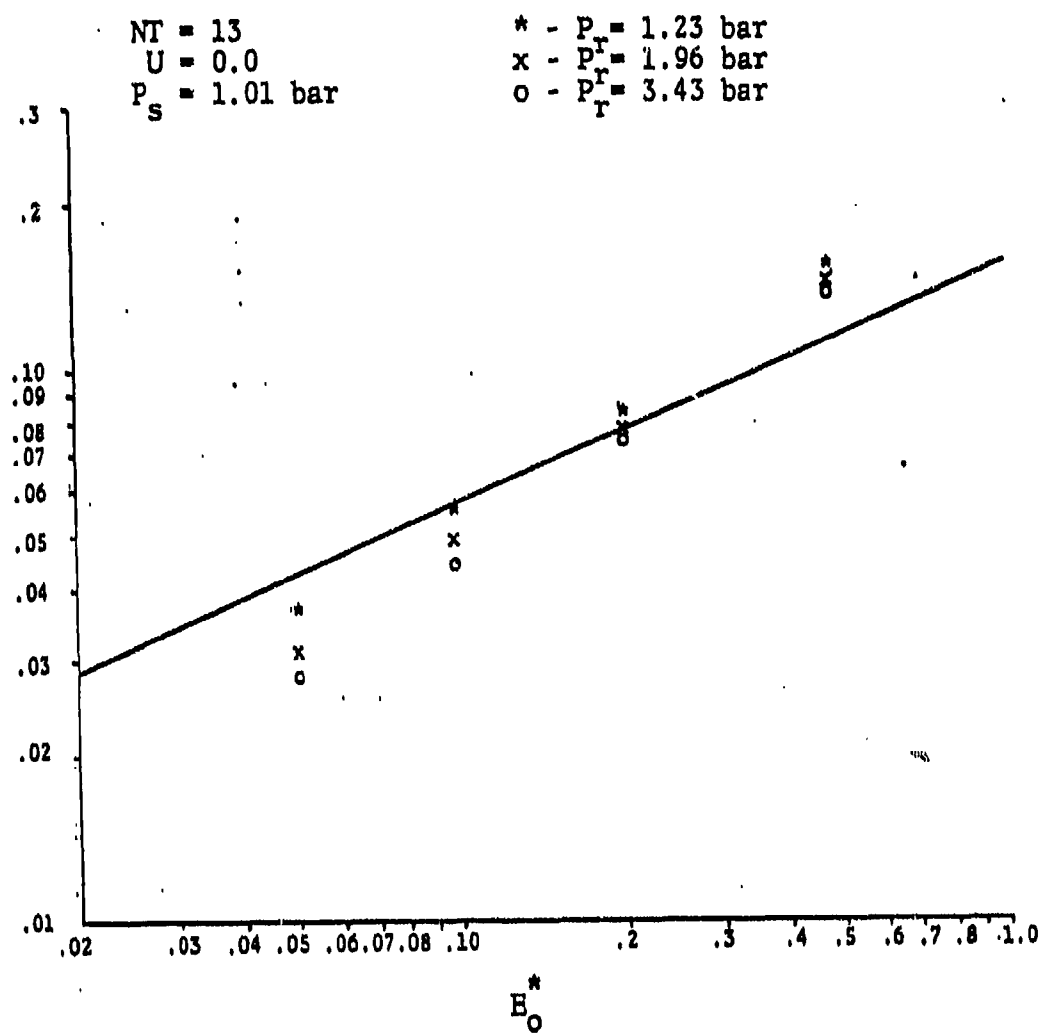


Figure 9. Comparison to data of [8] for seal in figure 6.

Appendix A

Definition of the First-order Continuity and Momentum Equation Coefficients

$$G_1 = \frac{A_{oi}}{RT}$$

$$G_2 = \frac{P_{oi} L}{RT}$$

$$G_3 = \frac{\dot{m}_o P_{oi}}{P_{oi-1}^2 - P_{oi+1}^2} - \frac{\dot{m}_o \mu_{1i+1}}{\pi} (5 - 4s_{1i+1}) \frac{\gamma-1}{\gamma P_{oi-1}} \frac{P_{oi}}{P_{oi+1}}^{\frac{1}{2}} + \frac{\dot{m}_o \mu_{1i}}{\pi} (5 - 4s_{1i}) \frac{\gamma-1}{\gamma P_{oi}} \frac{P_{oi}}{P_{oi+1}}$$

$$G_4 = \frac{-\dot{m}_o P_{oi-1}}{P_{oi-1}^2 - P_{oi}^2} + \frac{\dot{m}_o}{\pi} \mu_{1i} (4s_i - 5) \left[\frac{1}{P_{oi}} \left(\frac{\gamma-1}{\gamma} \right) \left(\frac{P_{oi-1}}{P_{oi}} \right)^{\frac{\gamma-1}{\gamma}} - \frac{1}{\gamma} \right]$$

$$G_5 = \frac{-\dot{m}_o P_{oi+1}}{P_{oi}^2 - P_{oi+1}^2} + \frac{\dot{m}_o}{\pi} \mu_{1i} (4s_i - 5) \left[\frac{1}{P_{oi+1}} \left(\frac{\gamma-1}{\gamma} \right) \left(\frac{P_{oi}}{P_{oi+1}} \right)^{\frac{\gamma-1}{\gamma}} - \frac{1}{\gamma} \right]$$

$$G_6 = \dot{m}_o \left(\frac{C_{ri} - C_{ri+1}}{C_{ri+1} C_{ri}} \right)$$

$$X_1 = \frac{P_{oi} A_{oi}}{RT}$$

$$X_2 = \dot{m}_o + \frac{\tau_{si} a_{si} L_i (2+ms)}{V_{oi}} + \frac{\tau_{ri} a_{ri} L_i (2+mr)}{(Rw - V_{oi})}$$

$$X_3 = \frac{\tau_{si} a_{si} L_i}{P_{oi}} - \frac{\tau_{ri} a_{ri} L_i}{P_{oi}} - \frac{\dot{m}_o P_{oi}}{P_{oi-1}^2 - P_{oi}^2} (V_{oi} - V_{oi-1}) P_{oi} + \frac{\dot{m}_o}{\pi} \mu_{1i} (4s_i - 5)$$

$$\left[\frac{1}{P_{oi}} \left(\frac{\gamma-1}{\gamma} \right) \left(\frac{P_{oi-1}}{P_{oi}} \right)^{\frac{\gamma-1}{\gamma}} - \frac{1}{\gamma} \right] (V_{oi} - V_{oi-1})$$

$$X_4 = \frac{\dot{m}_o P_{oi-1}}{P_{oi-1}^2 - P_{oi}^2} (V_{oi} - V_{oi-1}) - \frac{\dot{m}_o}{\pi} (V_{oi} - V_{oi-1}) \mu_{1i} (4s_i - 5)$$

$$\left[\frac{1}{P_{oi}} \left(\frac{\gamma-1}{\gamma} \right) \left(\frac{P_{oi-1}}{P_{oi}} \right)^{\frac{\gamma-1}{\gamma}} - \frac{1}{\gamma} \right]$$

$$X_5 = \frac{-\dot{m}_o}{Cr_1} (V_{oi} - V_{oi-1}) - \frac{ms\tau_{si}as_iL_iD_i}{2(Cr_1+B_1)^2} + \frac{\tau_{ri}axmr_iL_iD_i}{2(Cr_1+B_1)^2}$$

A₁₋₁ MATRIX

$$a_{1,2} = a_{2,1} = a_{3,4} = a_{4,3} = G_4$$

$$a_{5,2} = a_{6,1} = a_{7,4} = a_{8,3} = X_4$$

$$a_{5,6} = a_{6,5} = a_{7,8} = a_{8,7} = \dot{m}_0$$

The remaining elements are zero

A₁ MATRIX

$$a_{1,1} = G_1 \left(\omega + \frac{V_{o1}}{R_s} \right)$$

$$a_{2,2} = -G_1 \left(\omega + \frac{V_{o1}}{R_s} \right)$$

$$a_{3,3} = G_1 \left(\frac{V_{o1}}{R_s} - \omega \right)$$

$$a_{4,4} = -G_1 \left(\frac{V_{o1}}{R_s} - \omega \right)$$

$$a_{1,2} = a_{2,1} = a_{3,4} = a_{4,3} = G_3$$

$$a_{5,2} = a_{6,1} = a_{7,4} = a_{8,3} = X_3$$

$$a_{5,1} = a_{7,3} = \frac{A_{o1}}{R_s}$$

$$a_{6,2} = a_{8,4} = -\frac{A_{o1}}{R_s}$$

$$a_{5,5} = X_1 \left(\omega + \frac{V_{o1}}{R_s} \right)$$

$$a_{6,6} = -X_1 \left(\omega + \frac{V_{o1}}{R_s} \right)$$

$$a_{7,7} = X_1 \left(\frac{V_{o1}}{R_s} - \omega \right)$$

$$a_{8,8} = X_1 \left(\omega - \frac{V_{o1}}{R_s} \right)$$

$$a_{5,6} = a_{6,5} = a_{7,8} = a_{8,7} = X_2$$

$$a_{1,5} = a_{3,7} = G_1 \frac{P_{o1}}{R_s}$$

$$a_{2,6} = a_{4,8} = -G_1 \frac{P_{o1}}{R_s}$$

The remaining elements are zero.

A₁₊₁ MATRIX

$$a_{1,2} = a_{2,1} = a_{3,4} = a_{4,3} = G_5$$

Appendix B

Separation of the Continuity and Momentum Equations and Definition of the System Matrix Elements

CONTINUITY:

$$\begin{aligned}
 \cos(\theta + \omega t): & \quad G_{11} P_{s1}^+ \left(\omega + \frac{V_{o1}}{R_s} \right) + G_{11} \frac{P_{o1}}{R_s} V_{s1}^+ + G_{31} P_{c1}^+ + G_{41} P_{c1-1}^+ \\
 & \quad + G_5 P_{c1+1}^+ = \frac{G_{61}}{2} (a - b) \\
 \sin(\theta + \omega t): & \quad -G_{11} P_{c1}^+ \left(\frac{V_{o1}}{R_s} + \omega \right) - G_{11} \frac{P_{o1}}{R_s} V_{c1}^+ + G_{31} P_{s1}^+ + G_{41} P_{s1-1}^+ + G_{51} P_{s1+1}^+ \\
 & \quad + \frac{G_{61}}{2} \left(\frac{V_{o1}}{R_s} + \omega \right) (b - a) \\
 \cos(\theta - \omega t): & \quad G_{11} \left(\frac{V_{o1}}{R_s} - \omega \right) P_{s1}^- + G_{11} \frac{P_{o1}}{R_s} V_{s1}^- + G_{31} P_{c1}^- + G_{41} P_{c1-1}^- + G_{51} P_{c1+1}^- \\
 & \quad + \frac{G_{61}}{2} (a + b) \\
 \sin(\theta - \omega t): & \quad G_{11} \left(\omega - \frac{V_{o1}}{R_s} \right) P_{c1}^- - \frac{G_{11} P_{o1}}{R_s} V_{c1}^- + G_{31} P_{s1}^- + G_{41} P_{s1-1}^- + G_{51} P_{s1+1}^- \\
 & \quad + G_{51} P_{s1-1}^- = \frac{G_{61}}{2} \left(\omega - \frac{V_{o1}}{R_s} \right) (a + b)
 \end{aligned}$$

MOMENTUM:

$$\begin{aligned}
 \cos(\theta + \omega t): & \quad X_{11} \left(\omega + \frac{V_{o1}}{R_s} \right) V_{s1}^+ + \frac{A_{o1}}{R_s} P_{s1}^+ + X_{21} V_{c1}^+ - m_o V_{c1-1}^+ + X_{31} P_{c1}^+ \\
 & \quad + X_{41} P_{c1-1}^+ = \frac{X_{51}}{2} (b - a) \\
 \sin(\theta + \omega t): & \quad -X_{11} \left(\omega + \frac{V_{o1}}{R_s} \right) V_{c1}^+ - \frac{A_{o1}}{R_s} P_{c1}^+ + X_{21} V_{s1}^+ - m_o V_{s1-1}^+ + X_{31} P_{s1}^+ + X_{41} P_{s1-1}^+ \\
 \cos(\theta - \omega t): & \quad X_{11} \left(\frac{V_{o1}}{R_s} - \omega \right) V_{s1}^- + \frac{A_{o1}}{R_s} P_{s1}^- + X_{21} V_{c1}^- - m_o V_{c1-1}^- + X_{31} P_{c1}^- \\
 & \quad + X_{41} P_{c1-1}^- = \frac{-X_{51}}{2} (a + b) \\
 \sin(\theta - \omega t): & \quad X_{11} \left(\omega - \frac{V_{o1}}{R_s} \right) V_{c1}^- - \frac{A_{o1}}{R_s} P_{c1}^- + X_{21} V_{s1}^- - m_o V_{s1-1}^- + X_{31} P_{s1}^- + X_{41} P_{s1-1}^-
 \end{aligned}$$

THE REMAINING ELEMENTS ARE ZERO

B and C Column Vectors

$$B = \begin{bmatrix} \frac{G_6}{2} \\ \frac{-G_2}{2} \left(\frac{V_{o1}}{R_s} + \omega \right) \\ \frac{G_6}{2} \\ \frac{G_2}{2} \left(\omega - \frac{V_{o1}}{R_s} \right) \\ \frac{-X_5}{2} \\ 0 \\ \frac{-X_5}{2} \\ 0 \end{bmatrix}$$

$$C = \begin{bmatrix} \frac{-G_6}{2} \\ \frac{G_2}{2} \left(\frac{V_{o1}}{R_s} + \omega \right) \\ \frac{G_6}{2} \\ \frac{G_2}{2} \left(\omega - \frac{V_{o1}}{R_s} \right) \\ \frac{X_5}{2} \\ 0 \\ \frac{X_5}{2} \\ 0 \end{bmatrix}$$

A COMPARISON OF EXPERIMENTAL AND THEORETICAL RESULTS FOR
LEAKAGE, PRESSURE DISTRIBUTION, AND ROTORDYNAMIC COEFFICIENTS
FOR ANNULAR GAS SEALS

PROGRESS REPORT
NASA CONTRACT NAS8-33716

Prepared by
COLBY GRAN NICKS

Principal Investigator
Dara W. Childs, Ph.D, P.E.

September 1984

ABSTRACT

A Comparison of Experimental and Theoretical Results for Leakage, Pressure Distribution, and Rotordynamic Coefficients for Annular Gas Seals. (December 1984)

Colby Oran Nicks, B.S., Virginia Polytechnic Institute and State University

Chairman of Advisory Committee: Dr. Dara Childs

This thesis concerns a study of annular gas seals which is currently in progress at Texas A&M University. A brief discussion of the importance of seal behavior in rotordynamics is presented, as is a review of current annular seal theory. An outline of Nelson's analytical-computational method for determining rotordynamic coefficients for this type of compressible-flow seal is included. Various means for the experimental identification of the dynamic coefficients are outlined, and the method employed at the TAMU test facility is explained. The TAMU test apparatus is described, and the test procedures are discussed. Experimental results, including leakage, entrance-loss coefficients, pressure distributions, and rotordynamic coefficients for a smooth and a honeycomb constant-clearance seal are presented and compared to theoretical results from Nelson's analysis. The results for both seals show little sensitivity to the running speed over the test range. Agreement between test results and theory for leakage through the seal is satisfactory. Test results for direct stiffness show a greater sensitivity to fluid prerotation than predicted. Test results show that the deliberately-roughened surface of the honeycomb seal provides improved stability versus the smooth seal.

DEDICATION

This thesis is dedicated to my wife Robin. Her love, support, and sacrifices have made it all possible.

ACKNOWLEDGEMENTS

It is appropriate to acknowledge the contributions that my co-workers have made to this project. Thanks go to Keith Hale and Dean Nunez for their dedication to making the apparatus and facility operate as smoothly as it has. Also, my gratitude goes out to Joe Scharrer and David Moyer for their assistance in the computational aspects of the program. I would also like to express my appreciation to David Elrod for his help in reducing the data to a manageable form, and to Ann Owens for her assistance with the written thesis work. Dr. Clay Nelson should not be overlooked for the contribution of his analytical model. Finally, thanks go to my advisor, Dr. Dara Childs, for his patience and guidance on this project.

TABLE OF CONTENTS

CHAPTER		Page
I	INTRODUCTION	1
II	ANNULAR SEAL ANALYSIS REVIEW	4
III	NELSON'S ANALYSIS	8
IV	TEST CONCEPTS	13
V	TEST APPARATUS OVERVIEW	22
VI	TEST HARDWARE	23
	Static Displacement Control	23
	Dynamic Displacement Control	26
	Pressure Ratio	28
	Inlet Circumferential Velocity Control	28
	Seal Configuration	30
	Rotational Speed	30
VII	INSTRUMENTATION	38
	Rotor Motion Measurements	38
	Reaction-Force Measurements	38
	Fluid Flow Measurements	39
VIII	DATA ACQUISITION AND REDUCTION	42
IX	TEST PROCEDURES	47
X	RESULTS	49
	Static Results	53
	Dynamic Results	65
	Dynamic Results-Smooth Seal	73
	Dynamic Results-Honeycomb Seal	76
XI	CONCLUSIONS	86
XII	REFERENCES	88
XIII	VITA	90

LIST OF TABLES

	Page
Table 1. Test seal specifications.	50
Table 2. Friction-factor data.	52
Table 3. Theory versus experiment leakage comparison. . . .	56

LIST OF FIGURES

	Page
Fig. 1 Small motion of a seal rotor about an eccentric position.	5
Fig. 2 Small motion of a seal rotor about a centered position.	5
Fig. 3 Empirical entrance-loss relationship used in Nelson's analysis.	10
Fig. 4 Static displacement method used for stiffness determination.	14
Fig. 5 Synchronous rotation and precession method used for equivalent coefficient identification.	15
Fig. 6 Independent rotation and precession method used for coefficient identification.	17
Fig. 7 External shaker method used for coefficient identification.	19
Fig. 8 Components used for static and dynamic displacement of seal rotor.	24
Fig. 9 Test apparatus.	25
Fig. 10 Shaking motion used for rotordynamic coefficient identification.	27
Fig. 11 Inlet guide vane detail.	29
Fig. 12 Cross-sectional view of test section showing smooth stator.	31
Fig. 13 Detail of smooth stator.	32
Fig. 14 Cross-sectional view of test section showing honeycomb stator.	33
Fig. 15 Detail of honeycomb stator.	34
Fig. 16 Test apparatus assembly.	36
Fig. 17 Exploded view of test apparatus.	37
Fig. 18 Signal conditioning schematic for data acquisition. .	43
Fig. 19 Honeycomb stator insert detail.	51

	Page
Fig. 20 Smooth seal leakage.	54
Fig. 21 Honeycomb seal leakage.	55
Fig. 22 Axial pressure gradient in smooth seal with no prerotation, unchoked flow, ten running speeds. . . .	57
Fig. 23 Axial pressure gradient in smooth seal with prerotation in the direction of rotor rotation. . . .	59
Fig. 24 Axial pressure gradient in smooth seal with no prerotation.	60
Fig. 25 Axial pressure gradient in smooth seal with prerotation opposing rotor rotation.	61
Fig. 26 Axial pressure gradient in honeycomb seal with prerotation in the direction of rotor rotation. . . .	62
Fig. 27 Axial pressure gradient in honeycomb seal with no prerotation.	63
Fig. 28 Axial pressure gradient in honeycomb seal with prerotation opposing rotor rotation.	64
Fig. 29 Entrance-loss for smooth seal, prerotation in direction of rotor rotation.	66
Fig. 30 Entrance-loss for smooth seal, no prerotation. . . .	67
Fig. 31 Entrance-loss for smooth seal, prerotation opposing rotation.	68
Fig. 32 Entrance-loss for honeycomb seal, prerotation in direction of rotor rotation.	69
Fig. 33 Entrance-loss for honeycomb seal, no prerotation. . .	70
Fig. 34 Entrance-loss for honeycomb seal, prerotation opposing rotor rotation.	71
Fig. 35 Relative transfer function of test apparatus.	72
Fig. 36 Direct stiffness of smooth seal.	74
Fig. 37 Cross-coupled stiffness of smooth seal.	75
Fig. 38 Direct damping of smooth seal.	77
Fig. 39 Cross-coupled damping of smooth seal.	78

	Page
Fig. 40 Direct stiffness of honeycomb seal.	79
Fig. 41 Cross-coupled stiffness of honeycomb seal.	80
Fig. 42 Direct damping of honeycomb seal.	82
Fig. 43 Cross-coupled damping of honeycomb seal.	83
Fig. 44 Whirl frequency ratio for smooth and honeycomb seals.	84

NOMENCLATURE

A, B	= Fourier coefficients for rotor motion
C, c	= direct and cross-coupled stiffness coefficients (FT/L)
e_0	= displacement of seal rotor from centered position (L)
K, k	= direct and cross-coupled stiffness coefficients (F/L)
\bar{K}	= entrance-loss coefficient
M, m	= direct and cross-coupled added-mass coefficients (M)
m	= fluid mass flow rate (M/T)
n_s, m_s	= stator Hirs coefficients
n_r, m_r	= rotor Hirs coefficients
p	= fluid pressure (F/L ²)
R	= seal radius (L)
R_a	= $2\rho UC/\mu$ = nominal axial Reynolds number
U	= mean fluid flow velocity (L/T)
X, Y	= radial seal displacements (L)
γ	= ratio of specific heats for air
ϵ_0	= e_0 / C_r = equilibrium eccentricity ratio
ρ	= fluid density (M/L ³)
λ	= Fanning friction-factor
τ	= fluid shear stress (F/L ²)
ω	= shaft angular velocity (1/T)
Ω	= shaft precessional velocity (1/T)
μ	= fluid viscosity (FT/L ²)

INTRODUCTION

With turbomachinery design trends tending toward increased speeds and loadings, lighter weight, and reduced clearances between rotating and stationary parts, considerable concern with instability and synchronous response has arisen. Synchronous response refers to vibration of the turbomachine rotor assembly at a frequency coincident with the rotational speed. Characteristically, the vibration amplitude increases to a maximum at each critical speed (coincidence of the running speed with a rotor's damped natural frequency), and then decreases to a relatively steady level. Operation of turbomachines at rotational speeds above any of the critical speeds requires the rotor to traverse them during start-up and shut-down. Therefore, in order to limit the peak synchronous vibration levels, the machine designer aspires to introduce damping into the rotor system.

In contrast to synchronous vibration, "unstable" or "self-excited" motion is typically subsynchronous. This motion takes the form of whirling of the rotor shaft at a natural frequency less than the rotational speed. The exciting force for this whirling motion is a tangential force acting on the rotor due to some fluid or friction mechanism. This vibration often occurs with large amplitudes which sustain or grow as running speed increases. At best, this self-excited whirling prevents further speed increases; at worst, it results in damage to or catastrophic failure of the equipment. One of the rotordynamic force mechanisms which plays a role in self-excited rotor motion and synchronous response is that of the forces developed by Journal Model: ASME Journal of Lubrication Technology

annular seals. Until recently, most investigations of annular seals in turbomachinery have been concerned with reducing the leakage of the working fluid through the seal (i.e., improving the sealing effect). However, recent experiences have shown that forces developed by these seals can have considerable influence on the stability and synchronous response of rotating machinery. Black et al. [1-3] have demonstrated the critical effects that forces developed by neck-ring and interstage seals have on the rotordynamic behavior of pumps. Also, stability difficulties with the Space Shuttle Main Engine (SSME) high-pressure fuel turbopump [4] have prompted further research into these forces developed by liquid seals.

Experiences have shown that various gas seal configurations can have similar influences on the rotordynamic behavior of turbomachinery. In the high-pressure oxygen turbopump of the SSME, for example, initial vibration problems were remedied by changing the turbine interstage seal from a stepped-labyrinth configuration to a convergent taper seal with a honeycomb stator and a smooth rotor[5]. A lack of experimental data to completely explain this and other gas seal behavior makes obvious the need for research in this area.

The purpose of this report is twofold. It describes the test facility and initial test program developed to experimentally measure the fluid forces induced by annular gas seals, and it provides a comparison of theoretically predicted and experimentally obtained data for smooth and honeycomb seals. The leakage of the working fluid through the seal, the pressure gradient along the seal length, entrance pressure-loss data, and rotordynamic coefficients provide a basis for comparison. A short discussion on seal theory is included, and various

rotordynamic coefficient identification schemes are described. The work presented herein is intended to add to the rapidly expanding database on seal forces, and to determine the validity of one theoretical analysis for predicting those forces.

ANNULAR SEAL ANALYSIS REVIEW

As related to rotordynamics, seal analysis has the objective of determining the reaction forces acting on the rotor arising from shaft motion within the seal. Due to similarities between plain journal bearings and annular seals, seal analysis is generally based on governing equations which have previously been developed for bearings.

Annular seals and plain bearings are geometrically similar, but seals typically have radial clearance-to-radius ratios on the order of 0.005, versus C_r/R ratios of 0.001 for bearings. Due to seal clearances and pressure differentials, fully-developed turbulent flow normally exists. Also, seals are nominally designed to operate in a centered position. Journal bearings, on the other hand, have operating eccentricities which vary with running speed and load. Therefore, most of the rotordynamic work for bearings has been done to determine dynamic coefficient versus eccentricity relationships.

Two linearized seal models, expressed in terms of dynamic coefficients, have been suggested for the motion/reaction-force relationship. For small motions of the rotor about an arbitrary position in the seal, as shown in Fig.1, the relation can be written

$$-\begin{Bmatrix} F_X \\ F_Y \end{Bmatrix} = \begin{Bmatrix} K_{XX}(\epsilon_0) & K_{XY}(\epsilon_0) \\ K_{YX}(\epsilon_0) & K_{YY}(\epsilon_0) \end{Bmatrix} \begin{Bmatrix} X \\ Y \end{Bmatrix} + \begin{Bmatrix} C_{XX}(\epsilon_0) & C_{XY}(\epsilon_0) \\ C_{YX}(\epsilon_0) & C_{YY}(\epsilon_0) \end{Bmatrix} \begin{Bmatrix} \dot{X} \\ \dot{Y} \end{Bmatrix} + \begin{Bmatrix} M_{XX}(\epsilon_0) & M_{XY}(\epsilon_0) \\ M_{YX}(\epsilon_0) & M_{YY}(\epsilon_0) \end{Bmatrix} \begin{Bmatrix} \ddot{X} \\ \ddot{Y} \end{Bmatrix} \quad (1)$$

where the dynamic coefficients $\{K_{XX}, K_{YY}, C_{XX}, C_{YY}, M_{XX}, M_{YY}\}$ and $\{K_{XY}, K_{YX}, C_{XY}, C_{YX}, M_{XY}, M_{YX}\}$ represent the "direct" and "cross-coupled" stiffness, damping, and added-mass terms, respectively. These

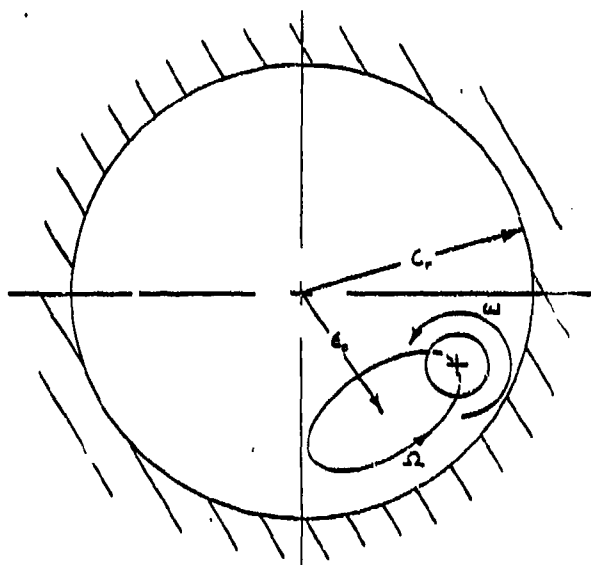


Fig. 1 Small motion of a seal rotor about an eccentric position; ω is the rotor spin speed, Ω is the precessional orbit frequency.

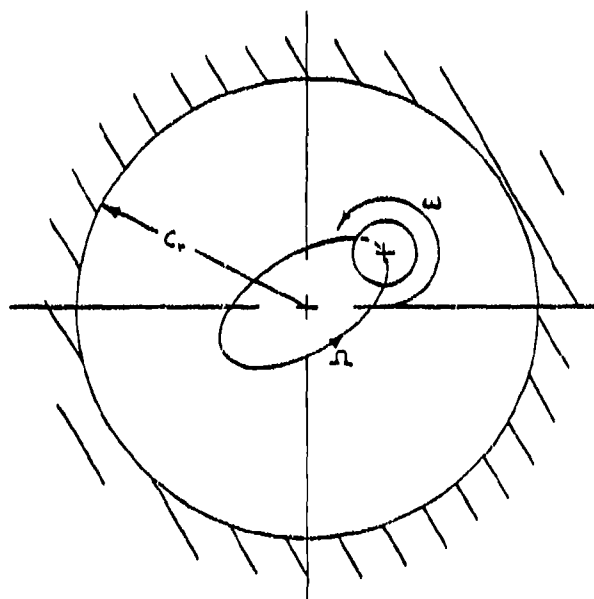


Fig. 2 Small motion of a seal rotor about a centered position; ω is the rotor spin speed, Ω is the precessional orbit frequency.

coefficients are functions of the equilibrium eccentricity ratio $e_0 = e_0 / C_r$, where the eccentricity ratio e_0 equals the displacement (e_0) of the rotor from the centered position divided by the nominal radial clearance (C_r). The term "cross-coupled" refers to the coupling effect exhibited by the off-diagonal terms; specifically, motion in one plane introduces reaction forces in an orthogonal one. These cross-coupled terms arise from the fluid's circumferential velocity component, and show a strong dependency on both the magnitude and direction (with respect to rotor rotation) of the velocity. This circumferential velocity component may arise from the prerotation of the fluid as it enters the seal due to some rotating element upstream, or it may develop as the fluid passes through the seal, with rotor shear forces "dragging" the viscous fluid around its periphery. The cross-coupled stiffness term usually produces a destabilizing force component, and therefore is of considerable interest. The cross-coupled damping and added-mass terms are generally much less influential than the cross-coupled stiffness term with respect to stability. For no fluid rotation, these cross-coupled terms are zero.

The second linearized seal model applies for small motions of the rotor about a centered position in the seal, as shown in Fig. 2. This model can be expressed

$$-\begin{Bmatrix} F_X \\ F_Y \end{Bmatrix} = \begin{bmatrix} K & k \\ -k & K \end{bmatrix} \begin{Bmatrix} X \\ Y \end{Bmatrix} + \begin{bmatrix} C & c \\ -c & C \end{bmatrix} \begin{Bmatrix} \dot{X} \\ \dot{Y} \end{Bmatrix} + \begin{bmatrix} M & m \\ -m & M \end{bmatrix} \begin{Bmatrix} \ddot{X} \\ \ddot{Y} \end{Bmatrix} \quad (2)$$

where the dynamic coefficient matrices are skew-symmetric.

Theoretical work on annular seals has been done for both incompressible and compressible fluids. Black et al. [6] have developed

analytical "short-seal" solutions for incompressible seals, which account for circumferential fluid flow due to wall shear stresses but not pressure perturbations. The analysis employs a bulk-flow assumption and accounts for fluid prerotation as it enters the seal. Childs' [7] incompressible seal analysis provides "finite-length" solutions, in which both shear and pressure-induced flow are included. Childs' utilizes Hirs' [8] turbulent bulk-flow model, and accounts for inlet swirl as well as perturbations in axial and circumferential Reynolds numbers due to clearance perturbations.

Compressible flow in seals has been analyzed by Fleming [9, 10] and Nelson [11, 12]. Fleming presents a short seal solution for the leakage, direct stiffness, and direct damping coefficients for straight and tapered, smooth, annular gas seals, but does not include the cross-coupled damping terms. Nelson, whose analysis is used for comparison in this report, analyzes both smooth and surface-roughened annular seals in the straight and tapered configurations. An outline of Nelson's analysis is included in the section that follows.

NELSON'S ANALYSIS

Nelson [11, 12] has developed an analysis which provides both static and dynamic results for annular gas seals. The static results include fluid leakage through the seal, pressure gradient along the seal axis, and the fluid axial and circumferential velocities through the seal. Dynamic data provided by the analysis consists of the rotordynamic coefficients (direct and cross-coupled stiffness and damping terms) for small rotor motion about a centered position (equation(2)). Nelson assumes that the added-mass terms are negligible for gas seals, and, hence, equation(2) is written

$$-\begin{Bmatrix} \ddot{F}_X \\ \ddot{F}_Y \end{Bmatrix} = \begin{bmatrix} K & k \\ -k & K \end{bmatrix} \begin{Bmatrix} X \\ Y \end{Bmatrix} + \begin{bmatrix} C & c \\ -c & C \end{bmatrix} \begin{Bmatrix} \dot{X} \\ \dot{Y} \end{Bmatrix} \quad (3)$$

Nelson utilizes a modified Hirs' [8] turbulent bulk-flow fluid model to develop governing axial and circumferential momentum equations, and his model is completed by the continuity and energy equations. Hirs' model defines the wall shear stress τ_w as

$$\tau_w = 1/2 \rho U_m^2 \text{no}(2\rho U_m H / \mu)^{m_0} = 1/2 \rho U_m^2 \text{no} R_a^{m_0} \quad (4)$$

where U_m is the mean flow velocity relative to the surface upon which the shear stress acts, and H is the local seal clearance. Hirs' formulation assumes that the surface roughness is the same on the rotor and stator. However, if the bulk-flow velocities relative to the rotor and stator are substituted in equation (4), the shear stresses at the rotor and stator are, respectively,

$$\begin{aligned}\tau_r &= 1/2 \rho U_r^2 n_r (2\rho U_r H / \mu) m_r \\ \tau_s &= 1/2 \rho U_s^2 n_s (2\rho U_s H / \mu) m_s\end{aligned}\quad (5)$$

Hence, different surface roughnesses in the seal elements can be accounted for via the empirical coefficients m_r , n_r and m_s, n_s for the rotor and stator surfaces. These coefficients may be calculated from static-pressure-gradient test data, and are then provided as input parameters for Nelson's analysis.

Assuming small motion of the rotor about a centered position, Nelson uses a perturbation analysis similar to that employed by Childs [7] to develop zeroth and first-order perturbation equations. The zeroth-order solution represents a zero-eccentricity flow condition, with rotor rotation but without precession. This solution is iterative and yields the mass-leakage flow rate, and the axial distribution of pressure, axial velocity, density, and circumferential velocity.

An iterative solution scheme is employed, using initial guesses for the zeroth-order seal entrance Mach number and entrance pressure-loss coefficient. The entrance-loss relationship is defined by

$$p_0(0) = 1 / \{1 + [(\gamma-1)(\bar{k}+1)M_0^2(0)] / 2\}^{\gamma/(\gamma-1)} \quad (6)$$

where $p_0(0)$ is the seal entrance/reservoir pressure ratio and $M_0(0)$ is the entrance Mach number. The entrance Mach number is iteratively adjusted, and the loss coefficient \bar{k} is recalculated according to a curve fit by Deissler [13]

$$\bar{k} + 1 = \sqrt{5.3 / \log_{10} Ra} \quad (7)$$

which is plotted in Fig. 3. At axial Reynolds numbers above 200,000, \bar{k} is equated to zero. The iterative solution procedure for $M_0(0)$ and \bar{k} continues until either:

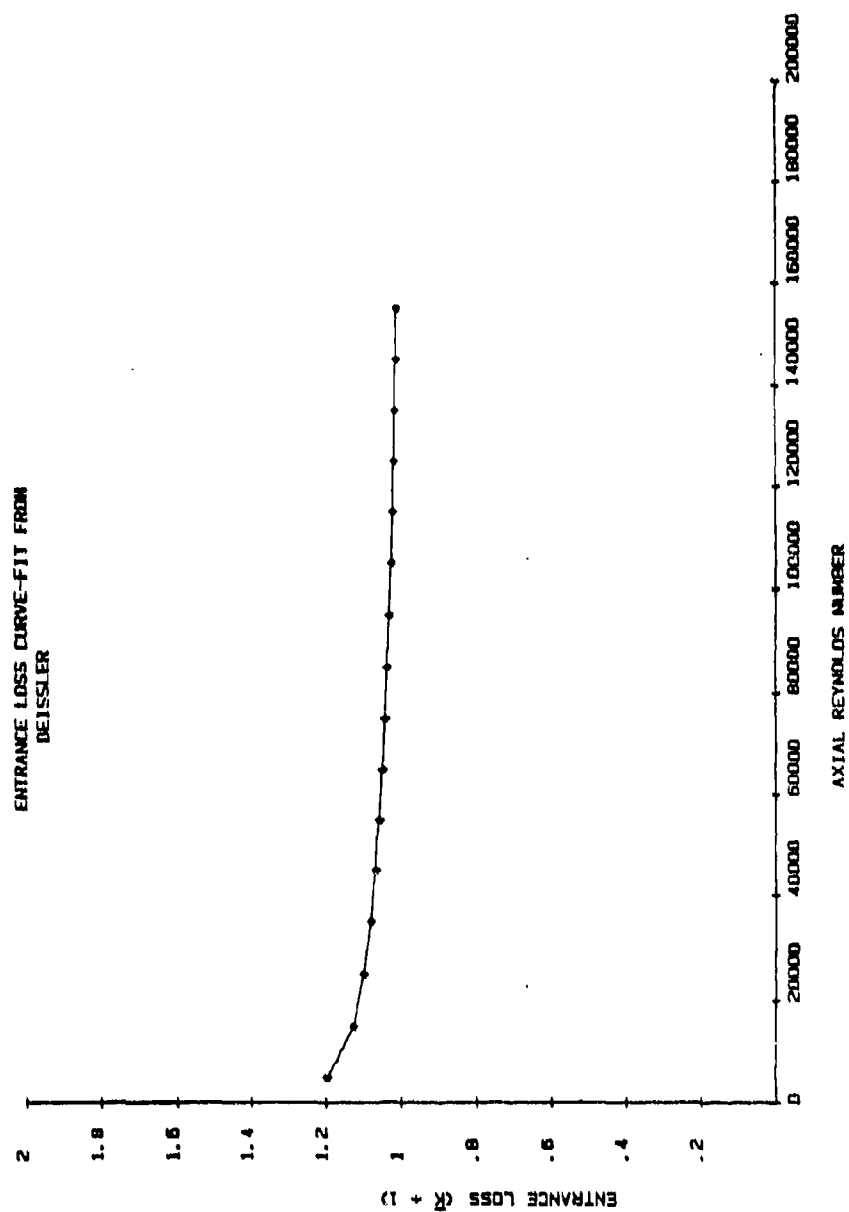


Fig. 3 Empirical entrance loss-relationship used in Nelson's analysis.

- 1) the Mach number at the exit reaches unity and the exit pressure is greater than the sump pressure (choked flow), or
- 2) the exit pressure equals the sump pressure and the exit Mach number is less than unity (unchoked flow).

The pressure, density, and velocity distribution and their derivatives which are determined in the zeroth-order solution are used in defining coefficients of the first-order perturbation equations. These equations define the pressure, density, and axial and circumferential velocity perturbations due to rotor motion, and are transformed to sixteen ordinary differential equations in the axial coordinate z . The four physical boundary conditions required for the solution of these equations depend on the perturbation conditions that are specified at the seal entrance and exit. The inlet circumferential velocity perturbation is zero. Expansion of the entrance pressure-loss relationship of equation (6) yields a second boundary condition. For choked flow, the first-order perturbation in the exit Mach number is zero, while for unchoked flow, the first-order perturbation in the exit pressure is zero.

Application of these boundary conditions and numerical integration of the ordinary differential equations provides the first-order solution. Integration of the first-order pressure solution along and around the seal periphery yields the direct and cross-coupled stiffness and damping coefficients, K , k , C , and c , respectively.

The input parameters which can be varied in Nelson's analysis include:

- 1) reservoir pressure and temperature,
- 2) sump pressure,

- 3) seal geometry (i.e. radius, length, clearances),
- 4) rotor rotational speed and precession rate,
- 5) entrance circumferential velocity of fluid,
- 6) rotor and stator surface roughness (Hirs constants),
- 7) empirical entrance-loss relationship, e.g., Deissler's, equation (16), and
- 8) fluid viscosity, gas constant, and ratio of specific heats.

It is apparent that a large amount of theoretical data can be generated to determine the influence that these various parameters have on the fluid forces in annular gas seals. However, there is a lack of experimental data with which to compare the results of Nelson's analysis. Currently, test results due to Wachter and Benckert [14] exist for labyrinth seals, a special class of non-contacting seals which have stepped surfaces or "teeth" on the rotor, stator, or both. Experimental results for smooth and/or surface-roughened gas seals are limited to data for honeycomb seals also published by Wachter and Benckert. Hence, the need for a test apparatus which can be used to study the effects of the same variables provided for in Nelson's analysis is obvious. The experimental data generated by such an apparatus would be valuable for comparison to both Nelson's theories and others which may be developed in the future.

TEST CONCEPTS

A number of test programs have been implemented to measure the stabilizing and destabilizing fluid forces which are developed by turbomachinery elements. Some are concerned mainly with the study of seal forces, while others examine the forces developed by centrifugal pump impellers. In each case, reaction force and relative motion measurements are used for rotordynamic coefficient identification. Four general approaches have been employed, and will be reviewed here.

Wachter and Benckert [14] employ a static displacement method for determining stiffness coefficients. In this method, as shown in Fig. 4, the rotor is displaced statically to some measured eccentric position while a pressure differential forces the working fluid past the seal. By measuring the reaction force components which are parallel and perpendicular to the static displacement vector, the direct and cross-coupled stiffnesses can be determined. Referring to equation (2) for small rotor motion about a centered position, a static rotor displacement in the X-direction yields

$$K = -F_x/e_o, k = F_y/e_o \quad (8)$$

Since this static displacement method has no dynamic motion, no damping or added-mass terms can be evaluated.

A second approach to rotordynamic coefficient identification is utilized by Childs[15]. Depicted in Fig.5, this method uses a circular orbit of the rotor within the seal. The rotor is mounted eccentrically on a shaft which rotates. Thus, the rotor precesses in a circular orbit at the same rate and direction as shaft rotation. This synchronous precession provides for the determination of the radial and tangential

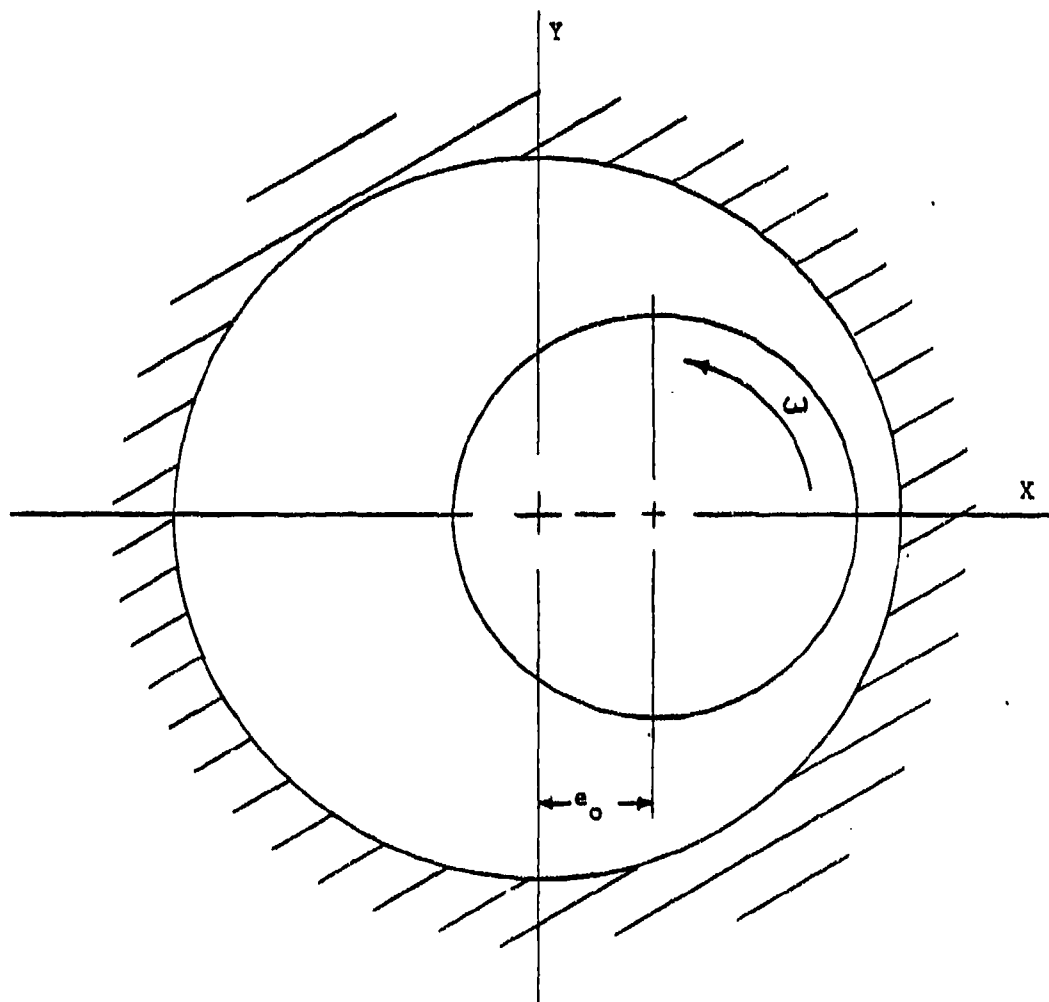


Fig. 4 Static displacement method used for stiffness determination.

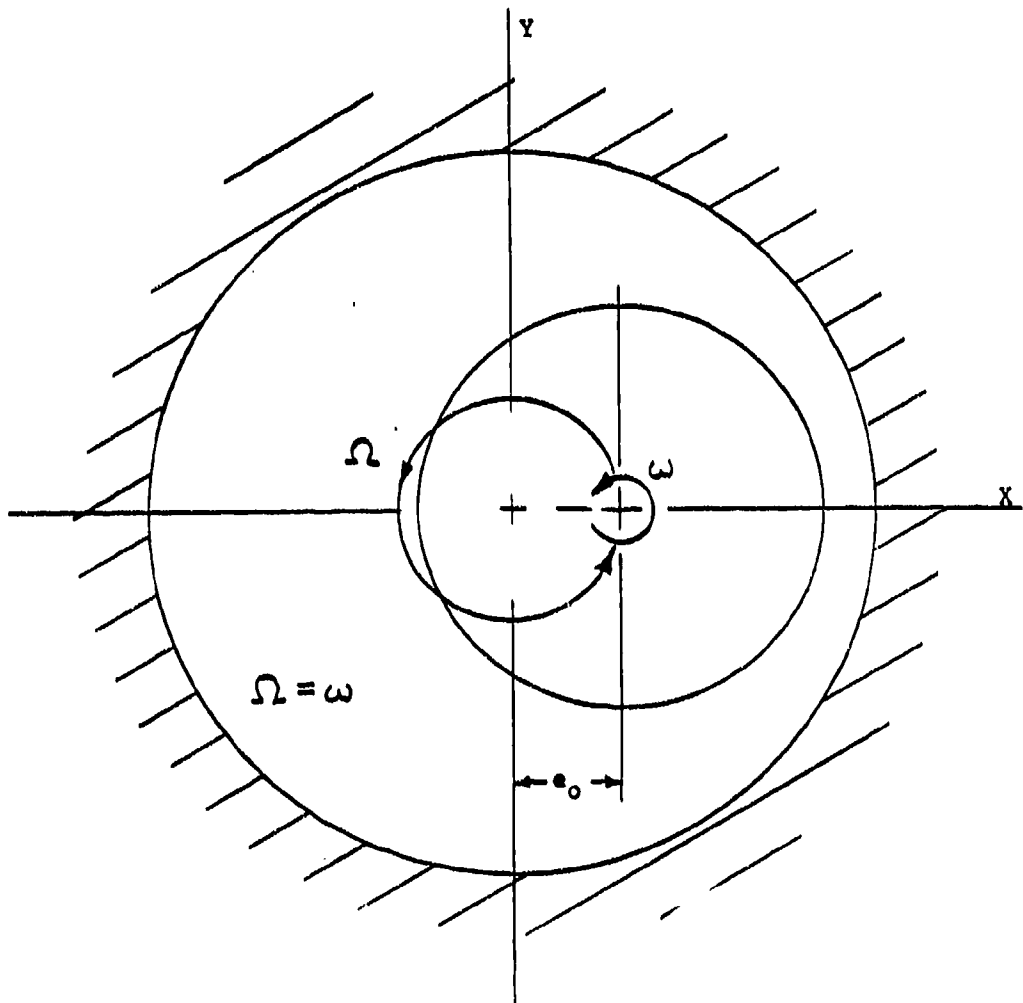


Fig. 5 Synchronous rotation and precession method used for equivalent coefficient identification.

components of the seal reaction force. The F_r and F components are obtained through integration of the measured pressure distribution along and around the seal periphery. Expressing measured rotor motion as

$$\begin{aligned} X &= e_0 \cos(\omega t) \\ Y &= e_0 \sin(\omega t) \end{aligned} \quad (9)$$

for small circular orbit of radius e_0 and precessional frequency $\omega = \Omega$, and substituting into equation (2) yields the radial and tangential force coefficient definitions

$$\begin{aligned} F_r / e_0 &= M\omega^2 - c\omega - K = -K_{ef} + M_{ef}\omega^2 \\ F / e_0 &= k - C\omega = -C_{ef}\omega \end{aligned} \quad (10)$$

where the cross-coupled mass coefficient is assumed negligible with respect to the influence of k and C . Because the cross-coupled coefficients k and c are linear functions of ω , identification of the individual dynamic coefficients is not possible in this method. However, equivalent direct stiffness, damping, and added-mass coefficients can be calculated as indicated in equation (10).

Independent rotation and precession control, as shown in Fig. 6, is a third testing method which is currently employed both in impeller and seal studies [16], [17], [18]. Various means are used to produce a circular orbit (precession) of the rotor or impeller at a rate different from its rotational speed. For a small circular orbit of radius e_0 and precessional frequency Ω , the measured precessional motion of the rotor is

$$\begin{aligned} X &= e_0 \cos(\Omega t) \\ Y &= e_0 \sin(\Omega t) \end{aligned}$$

The F_x and F_y reaction force components are measured and can be

components of the seal reaction force. The F_r and F components are obtained through integration of the measured pressure distribution along and around the seal periphery. Expressing measured rotor motion as

$$\begin{aligned} X &= e_0 \cos(\omega t) \\ Y &= e_0 \sin(\omega t) \end{aligned} \quad (9)$$

for small circular orbit of radius e_0 and precessional frequency $\omega = \Omega$, and substituting into equation (2) yields the radial and tangential force coefficient definitions

$$\begin{aligned} F_r / e_0 &= M\omega^2 - c\omega - K = -K_{ef} + M_{ef}\omega^2 \\ F / e_0 &= k - C\omega = -C_{ef}\omega \end{aligned} \quad (10)$$

where the cross-coupled mass coefficient is assumed negligible with respect to the influence of k and C . Because the cross-coupled coefficients k and c are linear functions of ω , identification of the individual dynamic coefficients is not possible in this method. However, equivalent direct stiffness, damping, and added-mass coefficients can be calculated as indicated in equation (10).

Independent rotation and precession control, as shown in Fig. 6, is a third testing method which is currently employed both in impeller and seal studies [16], [17], [18]. Various means are used to produce a circular orbit (precession) of the rotor or impeller at a rate different from its rotational speed. For a small circular orbit of radius e_0 and precessional frequency Ω , the measured precessional motion of the rotor is

$$\begin{aligned} X &= e_0 \cos(\Omega t) \\ Y &= e_0 \sin(\Omega t) \end{aligned}$$

The F_x and F_y reaction force components are measured and can be

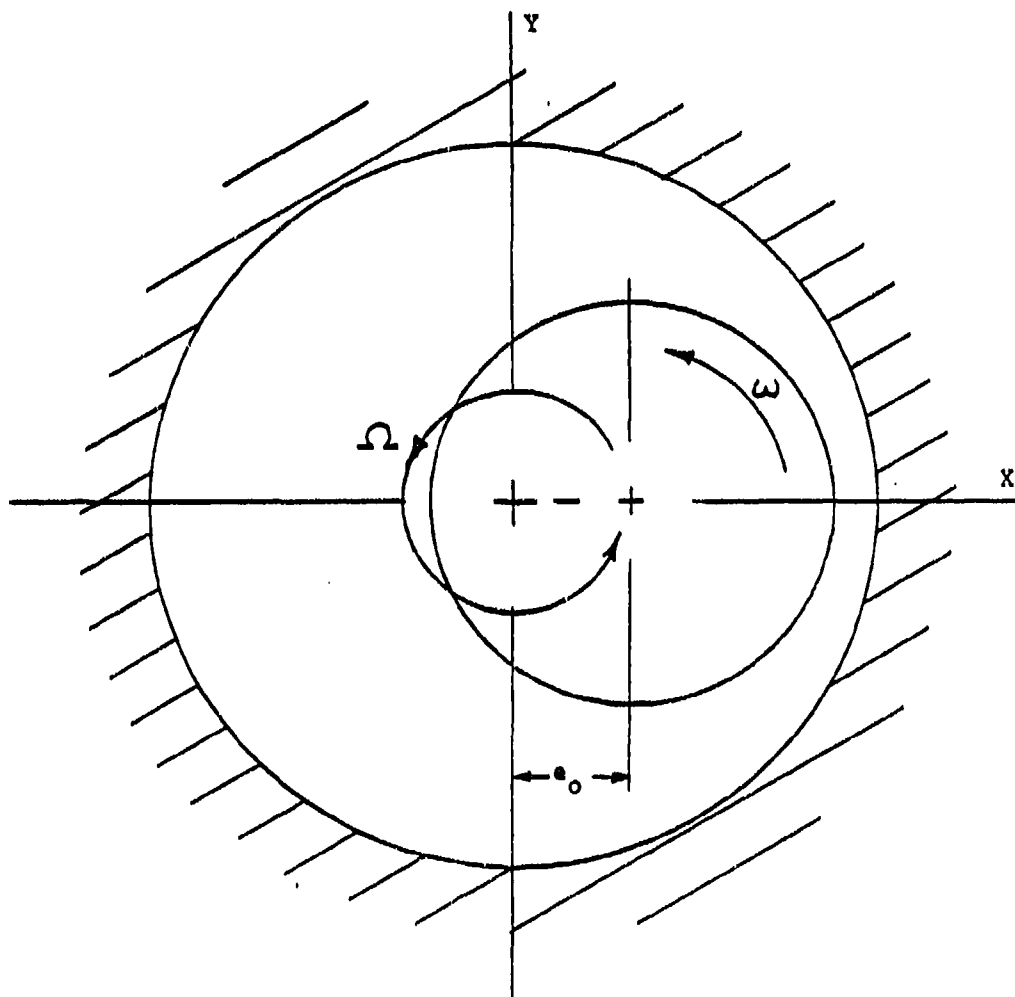


Fig. 6 Independent rotation and precession method used for coefficient identification.

expressed

$$\begin{aligned} F_X &= F_{XS} \sin(\Omega t) + F_{XC} \cos(\Omega t) \\ F_Y &= F_{YS} \sin(\Omega t) + F_{YC} \cos(\Omega t) \end{aligned} \quad (11)$$

By substituting these expressions into equation (2) and equating coefficients of sine and cosine terms, the following equations are obtained

$$\begin{aligned} -F_{XC} / e_0 &= K + c\Omega - M\Omega^2 & -F_{YC} / e_0 &= -k + C\Omega + m\Omega^2 \\ -F_{XS} / e_0 &= k - C\Omega - m\Omega^2 & -F_{YS} / e_0 &= K + c\Omega + M\Omega^2 \end{aligned} \quad (12)$$

Hence, by measuring the reaction force components and rotor motion at two different precession frequencies, eight equations in six unknowns are obtained, and the rotordynamic coefficients can be calculated.

A fourth testing method has been used by Iino and Kaneko [19] for determining dynamic coefficients, and this same method is employed at the TAMU gas seal test facility. An external hydraulic shaker is used to impart translatory harmonic motion to the rotating seal, and rotor motion relative to the stator and the reaction force components acting on the stator are measured.

Fig. 7 shows the manner in which the rotor could be positioned and oscillated in order to identify the dynamic coefficients of the seal for small motion about e_0 . If the added-mass terms are assumed negligible, equation (1) is rewritten

$$-\begin{Bmatrix} F_X \\ F_Y \end{Bmatrix} = \begin{bmatrix} K_{XX}(\epsilon_0) & K_{XY}(\epsilon_0) \\ K_{YX}(\epsilon_0) & K_{YY}(\epsilon_0) \end{bmatrix} \begin{Bmatrix} X \\ Y \end{Bmatrix} + \begin{bmatrix} C_{XX}(\epsilon_0) & C_{XY}(\epsilon_0) \\ C_{YX}(\epsilon_0) & C_{YY}(\epsilon_0) \end{bmatrix} \begin{Bmatrix} \dot{X} \\ \dot{Y} \end{Bmatrix} \quad (13)$$

First, harmonic horizontal motion of the rotor is assumed, where

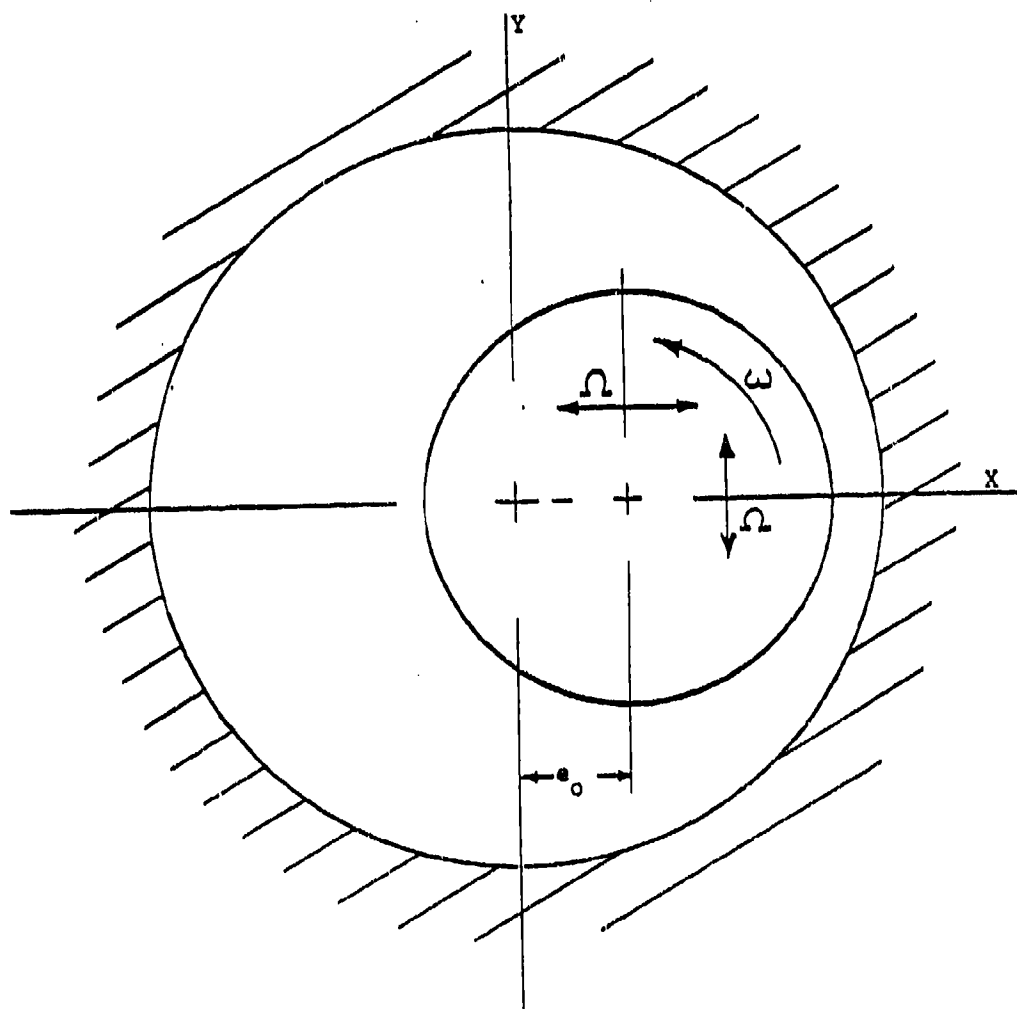


Fig. 7 External shaker method used for coefficient identification.

$$X = e_0 + A \sin(\Omega t) + B \cos(\Omega t)$$

$$\dot{X} = A\Omega \cos(\Omega t) - B\Omega \sin(\Omega t)$$

$$Y = \dot{Y} = 0$$

This yields small motion parallel to the static eccentricity vector, where Ω is the shaking frequency. In a similar fashion, the X and Y-direction force components can be expressed

$$\begin{aligned} F_X &= F_{XS} \sin(\Omega t) + F_{XC} \cos(\Omega t) \\ F_Y &= F_{YS} \sin(\Omega t) + F_{YC} \cos(\Omega t) \end{aligned} \quad (14)$$

Substituting these expressions into equation (13) and equating coefficients of sine and cosine terms yields the following four equations

$$\begin{aligned} F_{XS} &= K_{XX} A - C_{XX} B \\ F_{XC} &= K_{XX} B + C_{XX} A \\ F_{YS} &= K_{YX} A - C_{YX} B \\ F_{YC} &= K_{YX} B + C_{YX} A \end{aligned} \quad (15)$$

Solving this system of four equations in four unknowns defines the dynamic coefficients as

$$\begin{aligned} K_{XX}(\epsilon_0) &= (F_{XC} B + F_{XS} A) / (A^2 + B^2) \\ K_{YX}(\epsilon_0) &= (F_{YS} A + F_{YC} B) / (A^2 + B^2) \\ C_{XX}(\epsilon_0) &= (F_{XC} A - F_{XS} B) / \Omega(A^2 + B^2) \\ C_{YX}(\epsilon_0) &= (F_{YC} A - F_{YS} B) / \Omega(A^2 + B^2) \end{aligned} \quad (16)$$

Therefore, by measuring the reaction forces due to known rotor motion, determining the Fourier coefficients (A, B, F_{XS} , F_{XC} , F_{YS} , F_{YC}), and substituting into the above definitions, the indicated dynamic coefficients can be identified. If the rotor is shaken about a centered position, then the process is complete. Since the linearized model has skew-symmetric stiffness and damping matrices, all of the coefficients

are identified. If, however, the rotor is shaken about an eccentric position as initially postulated, then it must be shaken vertically about that same point in order to complete the identification process.

Assuming harmonic vertical motion of the rotor, as defined by

$$X = e_0, \dot{X} = 0,$$

$$Y = A \sin(\Omega t) + B \cos(\Omega t), \text{ and}$$

$$\dot{Y} = A\Omega \cos(\Omega t) - B\Omega \sin(\Omega t),$$

yields oscillatory motion that is perpendicular to the assumed static eccentricity vector. A similar process as before results in the coefficient definitions

$$\begin{aligned} K_{YY}(\epsilon_0) &= (F_{XS} A + F_{XC} B) / (A^2 + B^2) \\ K_{XY}(\epsilon_0) &= -(F_{YC} B + F_{YS} A) / (A^2 + B^2) \\ C_{YY}(\epsilon_0) &= (F_{XC} A - F_{XS} B) / \Omega(A^2 + B^2) \\ C_{XY}(\epsilon_0) &= (F_{YS} B - F_{YC} A) / \Omega(A^2 + B^2) \end{aligned} \quad (17)$$

All eight dynamic coefficients are thus determined by alternately shaking the rotor at one frequency Ω in directions which are parallel and perpendicular to the static eccentricity vector.

TEST APPARATUS OVERVIEW

Detailed design of the TAMU gas seal apparatus was carried out by J.B. Dressman of the University of Louisville. It is of the external shaker configuration, and the dynamic coefficient identification process is as described in the latter part of the preceding section.

Considering both the coefficient identification process and Nelson's analysis, some objectives for the design of the test apparatus are apparent. First, in order to determine the dynamic coefficients, the apparatus must provide for the necessary rotor motion within the seal, and measurement of the reaction-force components due to this motion must be possible. Secondly, it would be advantageous (for purposes of comparison) if the apparatus could provide the same variable seal parameters afforded by Nelson's analysis (i.e., pressures, seal geometry, rotor rotational speed, fluid prerotation, and rotor/stator surface roughness). With this capability, the influence of each independent parameter could be examined and compared for correlation between theoretical predictions and experimental results.

With these design objectives in mind, the discussion of the test apparatus is presented in three sections. The first section, Test Hardware, describes how the various seal parameters are physically executed and controlled. For example, the manner in which the dynamic "shaking" motion of the seal rotor is achieved and controlled is described in this section. The second section, Instrumentation, describes how these controlled parameters, such as rotor motion, are measured. Finally, the Data Acquisition and Reduction section explains how these measurements are used to provide the desired information.

TEST HARDWARE

This section deals only with the mechanical components and operation of the test apparatus. It is intended to provide answers to the following questions:

- 1) How is the static position of the seal rotor controlled?
- 2) How is the dynamic motion of the rotor executed and controlled?
- 3) How is compressed air obtained and supplied to the apparatus, and how is the pressure ratio across the seal controlled?
- 4) How is the incoming air prerotated before it enters the seal?
- 5) How are the seal rotor and stator mounted and replaced?
- 6) How is the seal rotor driven (rotated)?

Recalling the rotordynamic coefficient identification process described earlier, the external shaker method requires that the seal rotor be set in some static position and then be oscillated about that point. The test apparatus meets those requirements by providing independent static and dynamic displacement control, which are described below.

Static Displacement Control. The test apparatus is designed to provide control over the static eccentricity position both horizontally and vertically within the seal. The rotor shaft is suspended pendulum-fashion from an upper, rigidly mounted pivot shaft, as shown in Figs. 8 and 9. This arrangement allows a side-to-side (horizontal) motion of the rotor, and a cam within the pivot shaft allows vertical positioning of the rotor.

The cam which controls the vertical position of the rotor is driven

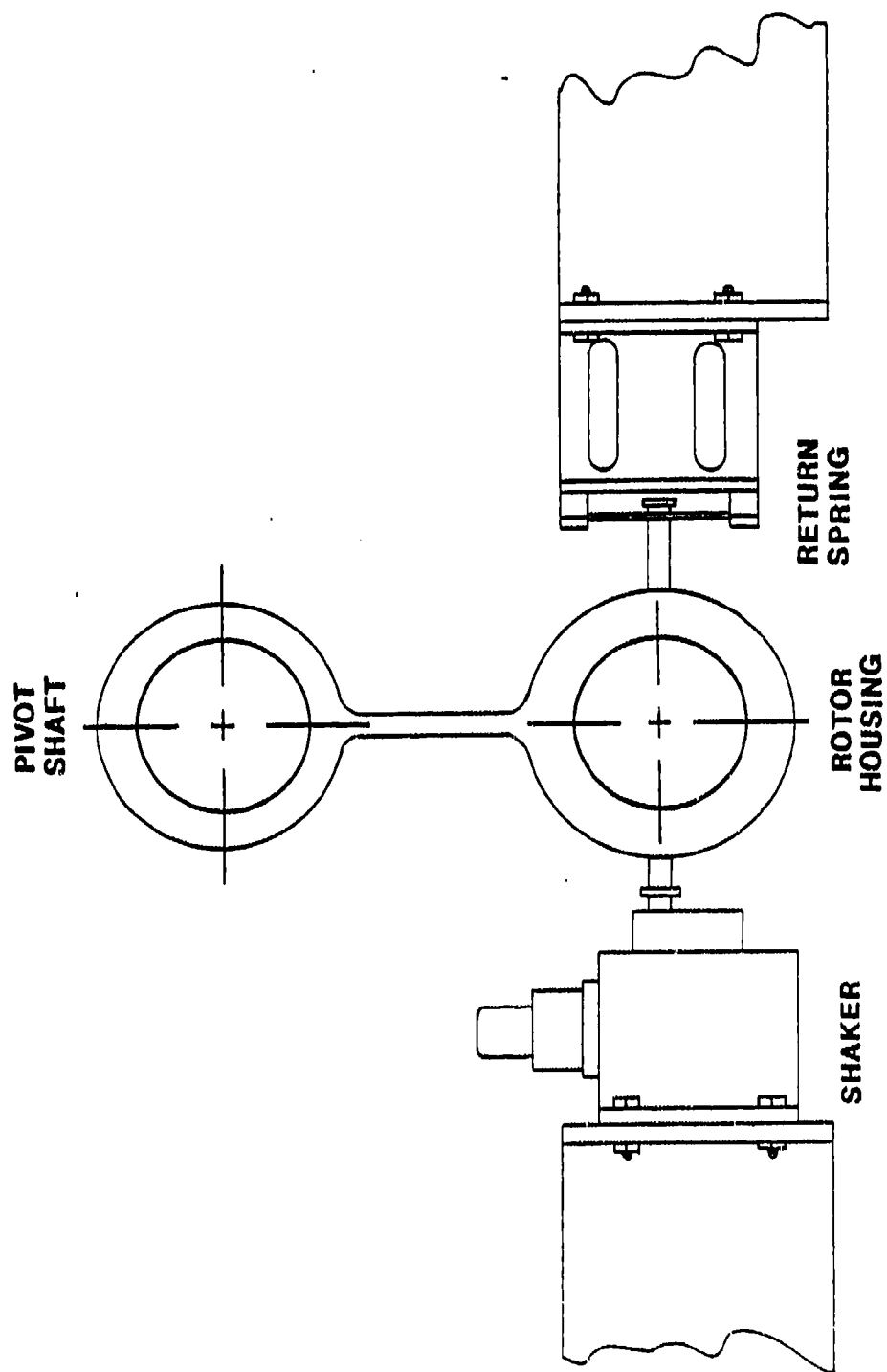


Fig. 8 Components used for static and dynamic displacement of seal rotor.

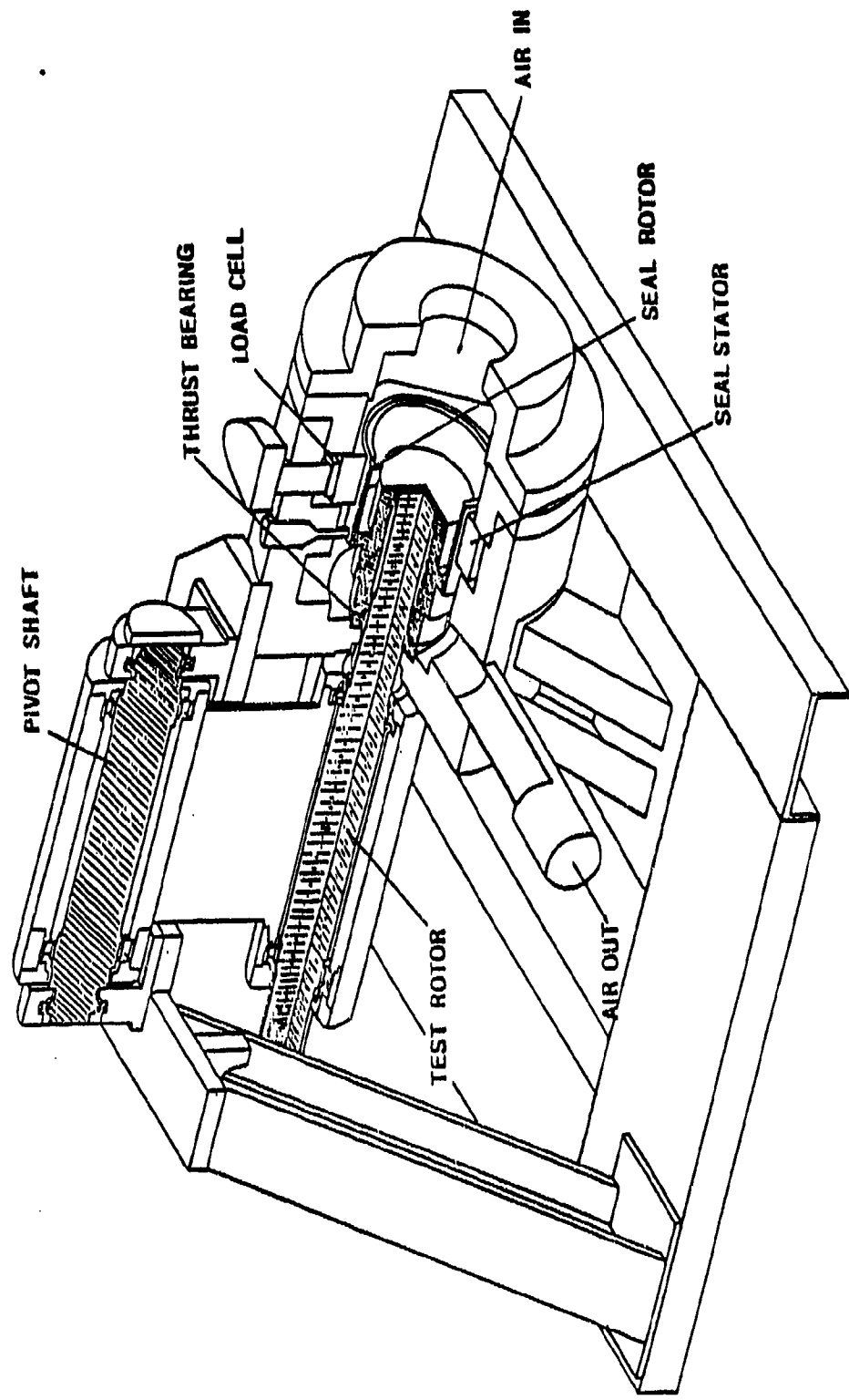


Fig. 9 Test apparatus.

by a remotely-operated DC gearhead motor, allowing accurate positioning of the rotor during testing. Horizontal positioning of the rotor is accomplished by a Zonic hydraulic shaker head and master controller, which provide independent static and dynamic displacement or force control. The shaker head is mounted on an I-beam support structure, and can supply up to 4450 N (1000 lbf) static and 4450 N dynamic force. As illustrated in Fig. 8, the shaker head output shaft acts on the rotor shaft bearing housing, and works against a return spring mounted on the opposite side of the bearing housing. The return spring maintains contact between the shaker head shaft and the bearing housing, thereby preventing hammering of the shaker shaft and the resulting loss of control over the horizontal motion of the rotor.

Dynamic Displacement Control. The dynamic motion of the seal rotor within the stator is horizontal. In addition to controlling the static horizontal position of the rotor, the Zonic shaker head moves the rotor through horizontal harmonic oscillations as the test is run. A Wavetek function generator provides the sinusoidal input signal to the Zonic controller, and both the amplitude and frequency of the rotor oscillations are controlled.

Although the test rig design provides for dynamic motion of the rotor only in the horizontal X-direction, all of the coefficients for either seal model (equation (3) or (13)) can still be determined. As Fig. 10 shows, the required rotor motion perpendicular to the static eccentricity vector can be accomplished in an equivalent manner by statically displacing it the same amount (e_0) in the vertical direction and continuing to shake horizontally.

In addition to providing control over the rotor's static position

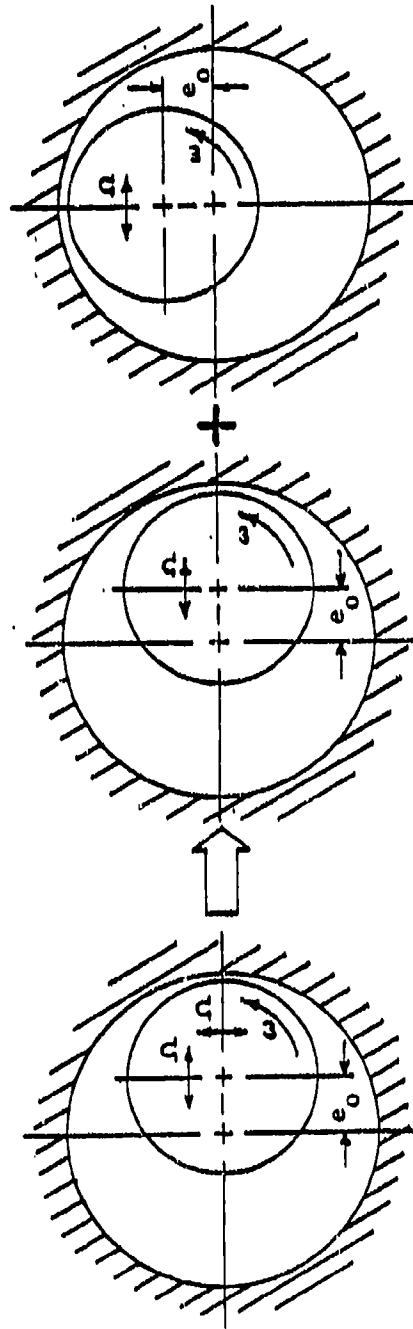


Fig. 10 Shaking motion used for rotordynamic coefficient identification.

and dynamic motion, the test apparatus allows other seal parameters to be controlled independently, providing insight into the influence these parameters have on seal behavior. These parameters coincide with the variable input parameters for Nelson's analysis, and they include:

- 1) pressure ratio across the seal,
- 2) prerotation of the incoming fluid,
- 3) seal configuration, and
- 4) rotor rotational speed.

Pressure Ratio. The inlet air pressure and attendant mass flow rate through the seal are controlled by an electric-over-pneumatically actuated Masoneilan Camflex II flow control valve located upstream of the test section. An Ingersoll-Rand SSR-2000 single stage screw compressor rated at $34 \text{ m}^3/\text{min}$ @ 929 kPa (1200 scfm @ 120 psig) provides compressed air, which is then filtered and dried before entering a surge tank. Losses through the dryers, filters, and piping result in an actual maximum inlet pressure to the test section of approximately 722 kPa (90 psig) and a maximum flow rate of $27 \text{ m}^3/\text{min}$ (950 scfm). A four-inch inlet pipe from the surge tank supplies the test rig, and after passing through the seal, the air exhausts to atmosphere through a manifold with muffler.

Inlet Circumferential Velocity Control. In order to determine the effects of fluid rotation on the rotordynamic coefficients, the test rig design also allows for prerotation of the incoming air as it enters the seal. This prerotation introduces a circumferential component to the air flow direction, and is accomplished by guide vanes which direct and accelerate the flow towards the annulus of the seal. The vanes are machined from brass disks, and Fig. 11 illustrates the vane

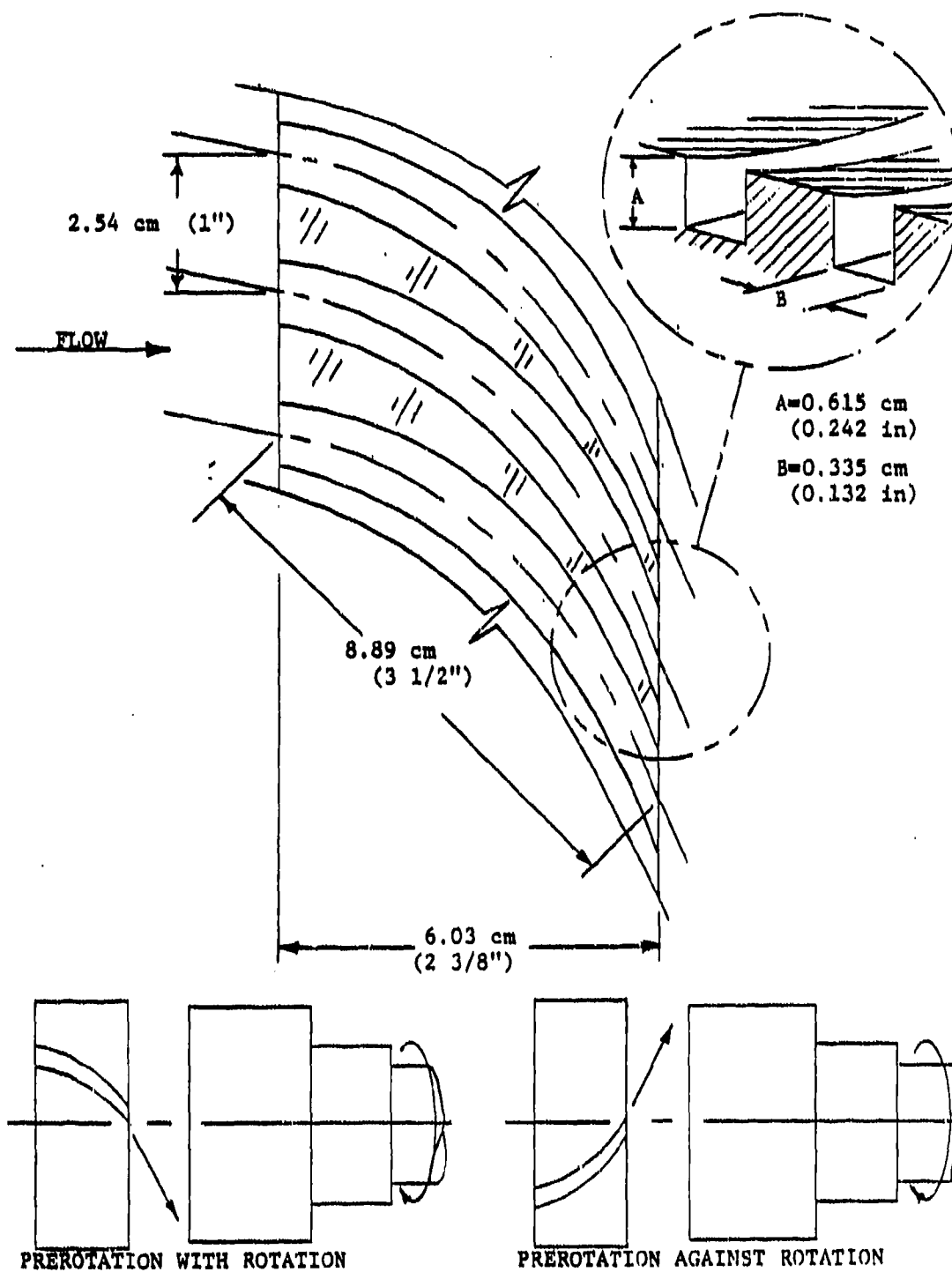


Fig. 11 Inlet guide vane detail.

configuration. Three sets of guide vanes are available; one rotates the flow in the direction of rotor rotation, another introduces no fluid rotation, and the third rotates the flow opposite the direction of rotor rotation.

Seal Configuration. The design of the test rig permits the installation of various rotor/stator combinations. As shown in Figs.12-15, the stator is supported in the test section housing by three Kistler quartz load cells in a trihedral configuration. Figs.12 and 13 show the smooth-rotor/smooth-stator seal, while the smooth-rotor/honeycomb-stator seal is illustrated in Figs.14 and 15. The seal rotor is press-fitted and secured axially by a bolt circle to the rotor shaft. Seals with different geometries (i.e., clearances, tapers, lengths) can be tested, as well as seals with different surface roughnesses. The replacement of these rotor/stator combinations can be accomplished with minimal downtime.

Rotational Speed. A Westinghouse 50-hp variable-speed electric motor drives the rotor shaft through a belt-driven jackshaft arrangement. This shaft is supported by two sets of Torrington hollow-roller bearings [20]. These bearings are extremely precise, radially preloaded, and have a predictable and repeatable radial stiffness. Axial thrust due to the pressure differential across the seal is absorbed by a flat, roller-type, caged thrust bearing at the rear of the rotor. Both the shaft and thrust bearings are lubricated by a positive-displacement gear-type oil pump.

Different jackshaft drive-pulleys can be fitted to provide up to a 4:1 speed increase from motor to rotor shaft, which would result in a rotor shaft speed range of 0-21,200 cpm. Current design limitations,

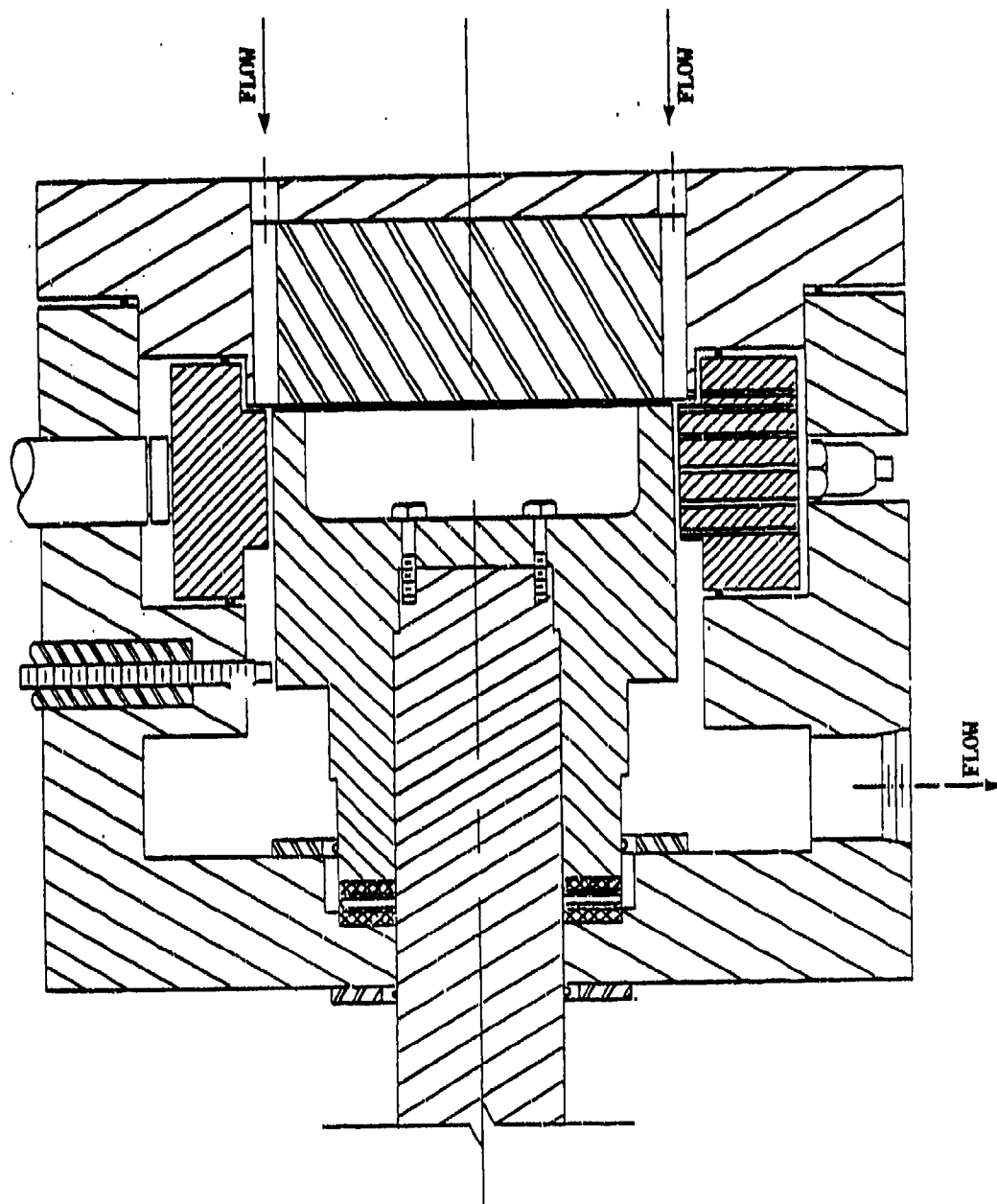


Fig. 12 Cross-sectional view of test section showing smooth stator.

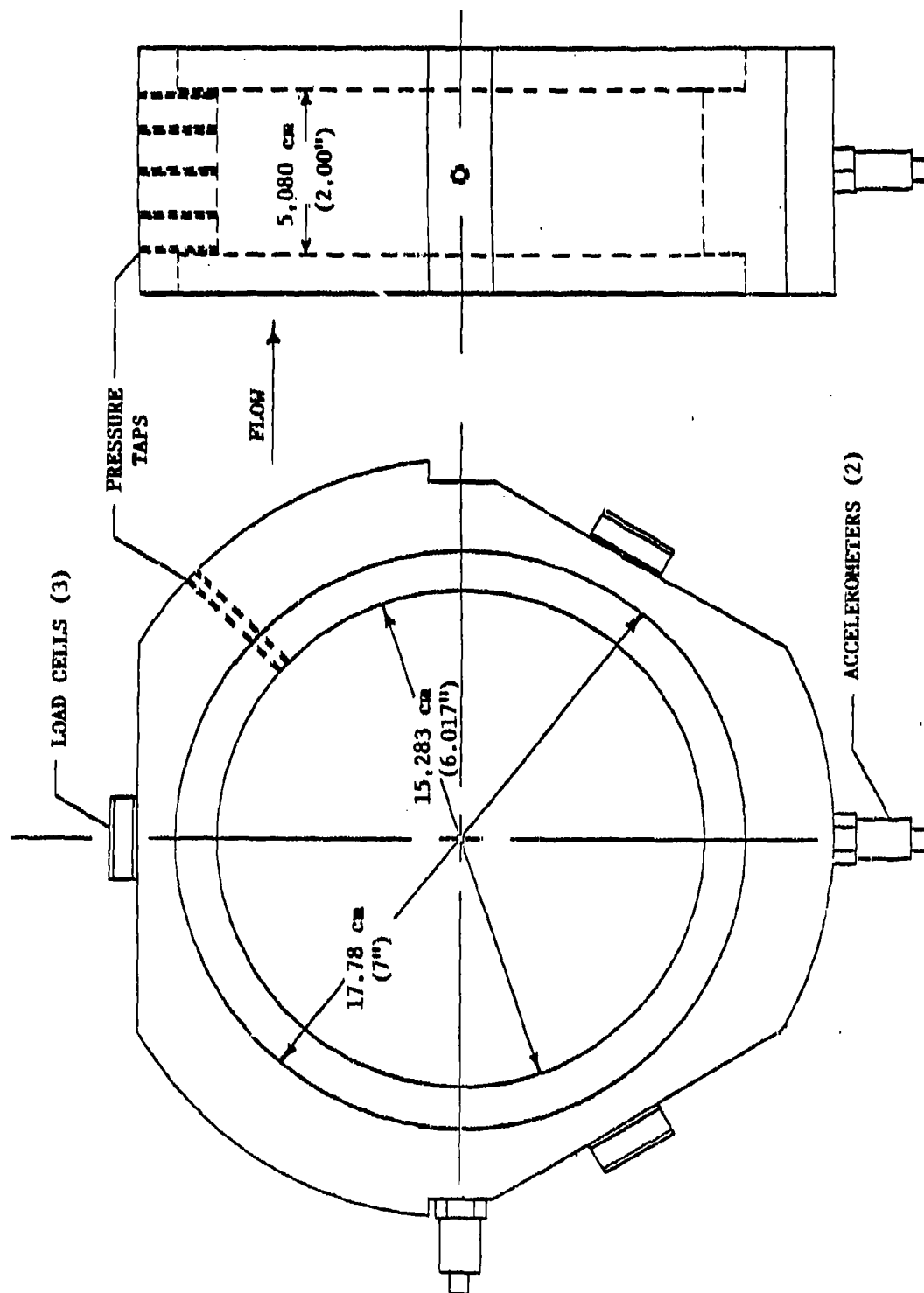


Fig. 13 Detail of smooth stator.

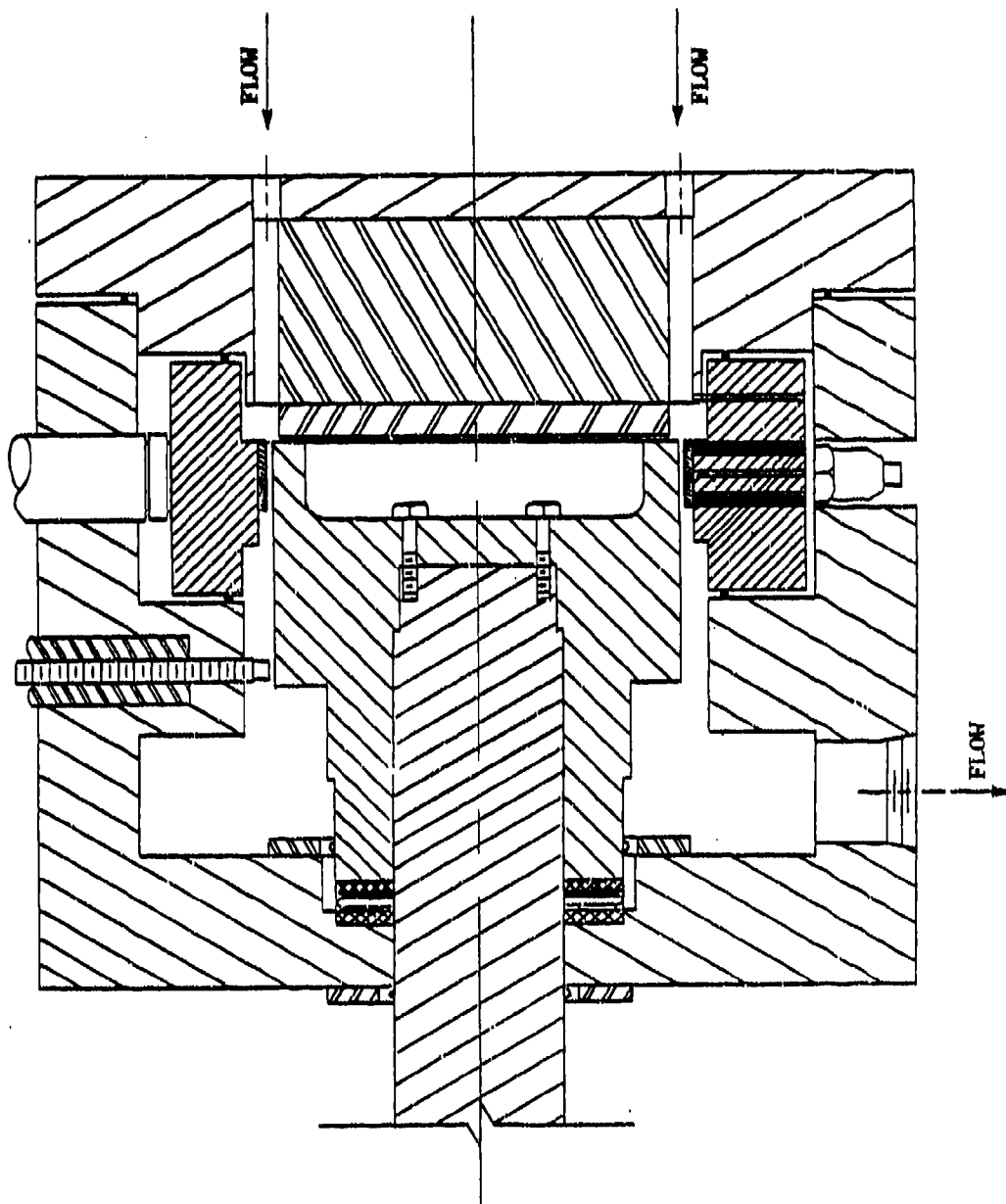


Fig. 14 Cross-sectional view of test section showing honeycomb stator.

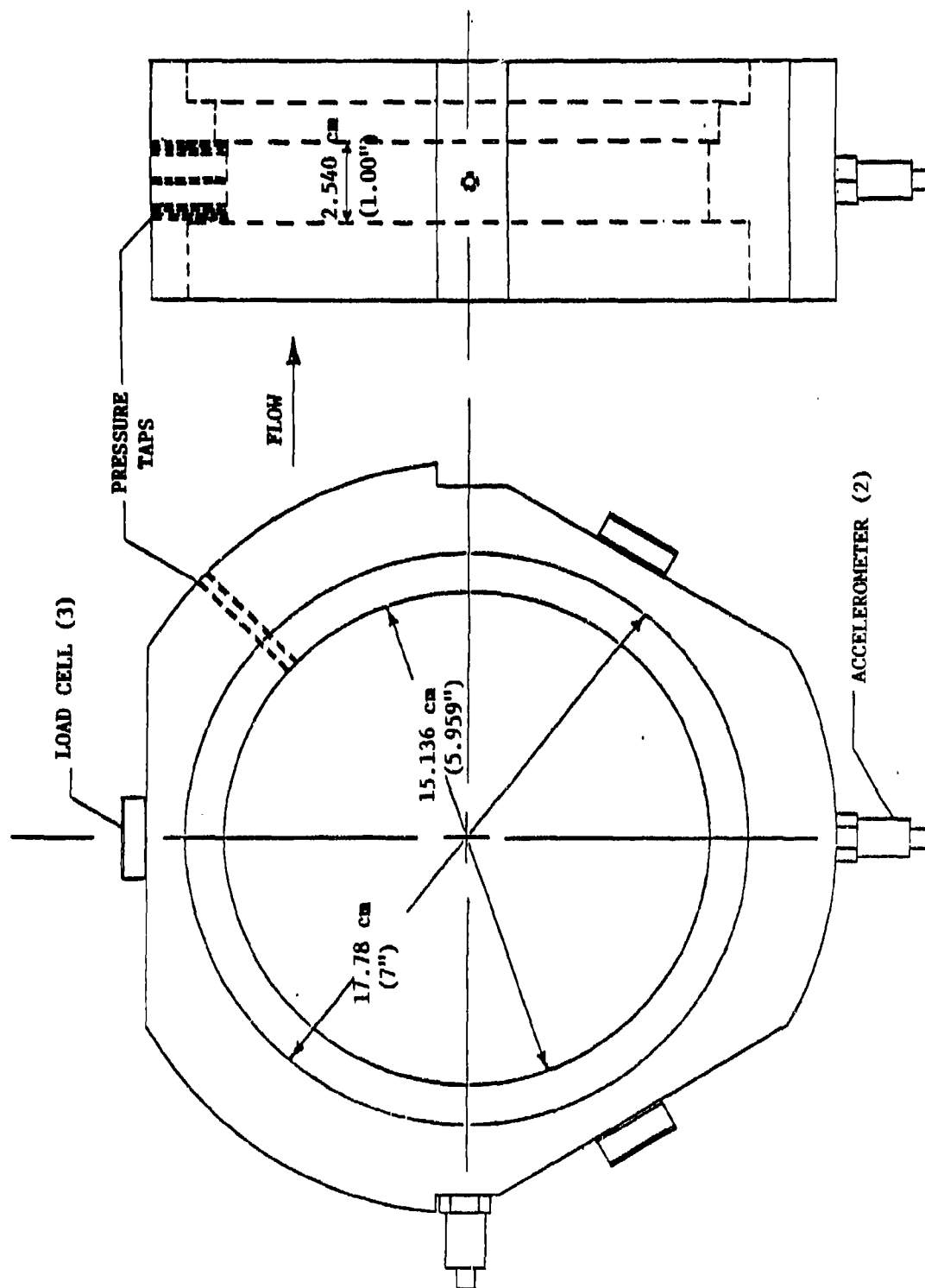


Fig. 15 Detail of honeycomb stator.

however, prevent the attainment of this upper rotational speed. High bearing temperatures, reduction of interference in the rotor-rotor shaft fitment due to inertia-induced radial growth of the rotor inside diameter, and excessive stresses in the drive-pulleys have served to limit shaft speed. The highest rotational speed attained at the time of this writing is 8500 opm, although design modifications to allow higher speeds are under investigation.

To conclude this discussion of the test hardware, two views of the complete test apparatus are included. Fig. 16 shows the assembled rig, while an exploded view is provided in Fig. 17.

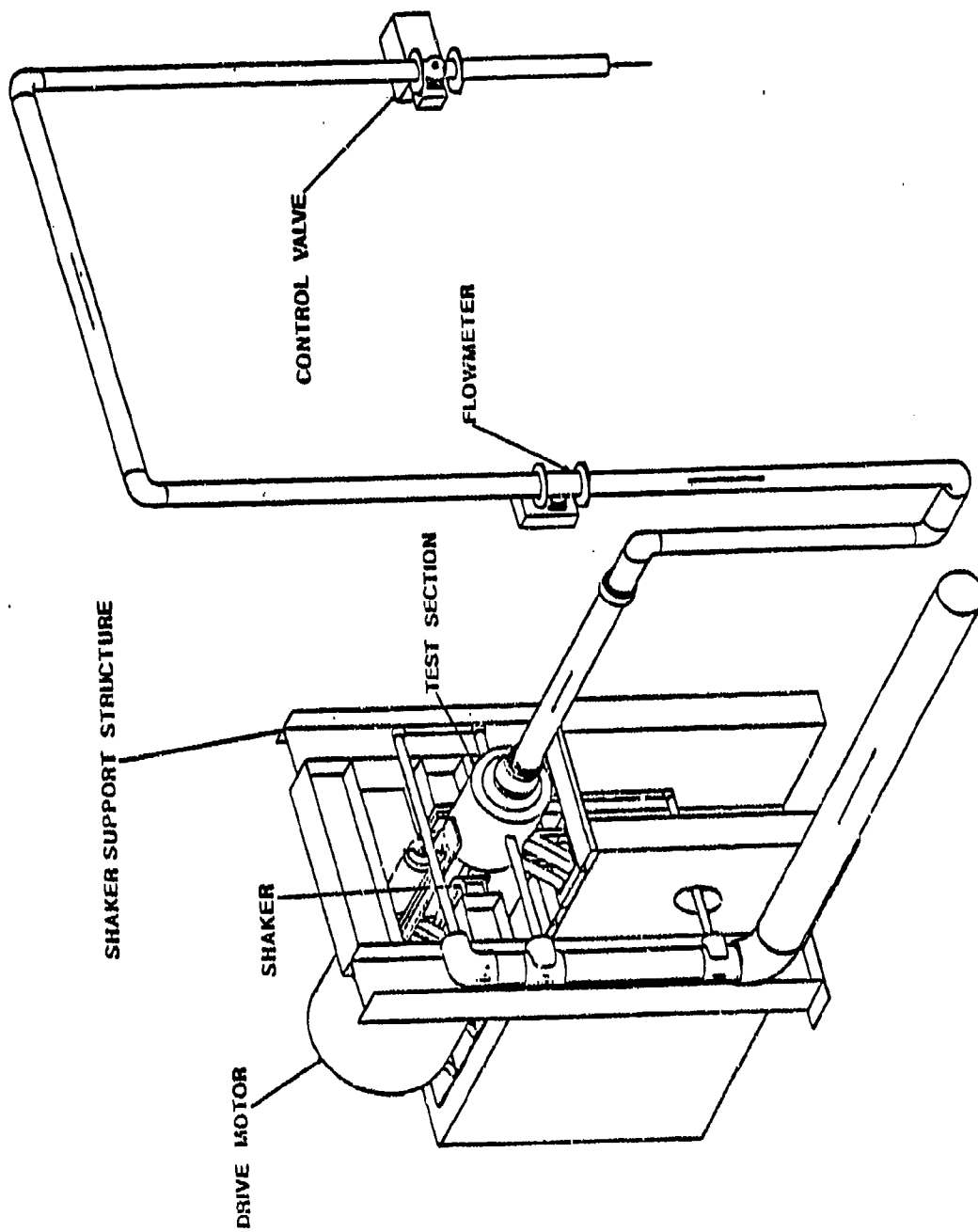


Fig. 16 Test apparatus assembly.

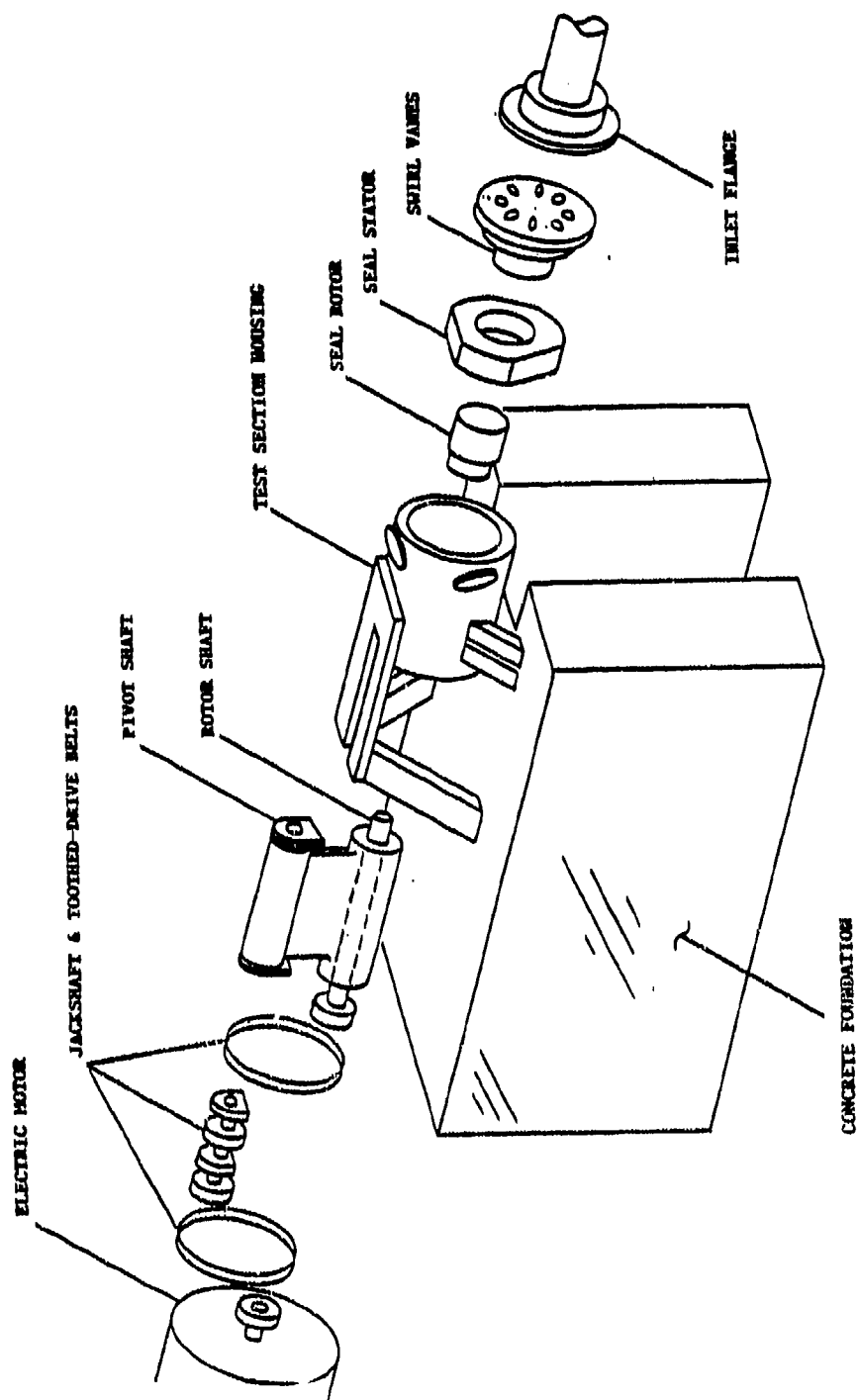


Fig. 17 Exploded view of test apparatus.

INSTRUMENTATION

Having discussed what seal parameters can be varied, and how the variations are implemented, the measurement of their respective effects can now be described. The types of measurements which are made can be grouped into three categories:

- 1) rotor motion,
- 2) reaction-force measurements, and
- 3) fluid flow measurements.

These categories are described individually in the sections that follow.

Rotor Motion Measurements. The position of the seal rotor within the stator is monitored by two Bently-Nevada eddy-current proximity probes, mounted in the test section housing. These probes are located 90 degrees apart, and correspond to the X and Y- directions. The proximity probes are used to determine the static position and dynamic motion of the rotor, and their resolution is 0.0025 mm (0.1 mil).

Reaction-Force Measurements. Reaction forces arise due to the static position and dynamic motion of the seal rotor within the stator. The reaction forces (F_x , F_y) exerted on the stator are measured by the three Kistler quartz load cells which support the stator in the test section housing. When the rotor is shaken, vibration is transmitted to the test section housing, both through the thrust bearing and through the housing mounts. The acceleration of the housing and stator generates unwanted inertial "ma" forces which are sensed by the load cells, in addition to those pressure forces developed by the relative motion of the seal rotor and stator. For this reason, PCB piezoelectric accelerometers with integral amplifiers are mounted in the X and Y-directions on the stator,

as shown in Figs. 13 and 15. These accels allow a (stator mass) x (stator acceleration) subtraction to the forces (F_x , F_y) indicated by the load cells. With this correction, which is described more fully in the next section, only the pressure forces due to relative seal motion are measured.

Force measurement resolution is a function of the stator mass and the resolution of the load cells and accelerometers. Accelerometer resolution is 0.005 g, which must be multiplied by the stator mass in order to obtain an equivalent force resolution. The masses of the stators used in the test program reported here are 11.4 kg (25.2 lb) and 3.94 kg (8.69 lb), corresponding to the smooth and honeycomb stators, respectively. Hence, force resolution for the accelerometers is 0.560 N (0.126 lb) and 0.191 N (0.043 lb), for each stator, respectively. Resolution of the load cells is 0.089 N (0.02 lb). Therefore, the resolution of the force measurement is limited by the accelerometers. With a stator with less mass, and/or accelerometers with greater sensitivity, force resolution could be improved.

Fluid Flow Measurements. Fluid flow measurements include the leakage (mass flow rate) of air through the seal, the pressure gradient along the seal axis, the inlet fluid circumferential velocity, and the entrance pressure loss.

Leakage is measured with a Fischer & Porter vortex flowmeter located in the piping upstream of the test section. Resolution of the flowmeter is 0.0014 m³ (0.05 acf), and pressures and temperatures up and downstream of the meter are measured for mass flow rate determination.

For measurement of the axial pressure gradient, the stator has pressure taps drilled along the length of the seal in the axial

direction. These pressures, as well as all others, are measured with a 0-1.034 MPa (0-150 psig) Scanivalve differential-type pressure transducer through a 48 port, remotely-controlled Scanivalve model J scanner. Transducer resolution is 0.552 kPa (0.08 psi).

In order to determine the circumferential velocity of the air as it enters the seal, the static pressure at the guide vane exit is measured. This pressure, in conjunction with the measured flowrate and inlet air temperature, is used to calculate a guide vane exit Mach number. A compressible flow continuity equation

$$\dot{m} = P_{ex} A_{ex} M_{ex} \left[(\gamma/R_g T_t) (1 + (\gamma-1)M_{ex}^2 / 2) \right]^{1/2} \quad (18)$$

is rearranged to provide a quadratic equation for M_{ex}

$$M_{ex}^2 = \{-1 + 1 + 4((\gamma-1)/2\gamma) (m R_g T_t / P_{ex} A_{ex})^2\} / (\gamma-1) \quad (19)$$

where γ is the ratio of specific heats and R_g is the gas constant for air, T_t is the stagnation temperature of the air, P_{ex} is the static pressure at the vane exit, and A_{ex} is the total exit area of the guide vanes. Since all of the variables in the equation are either known or measured, the vane exit Mach number, and therefore the velocity, can be found.

In order to determine the circumferential component of this inlet velocity, a flow turning angle correction, in accordance with Cohen[21], is employed. The correction has been developed from guide vane cascade tests, and accounts for the fact that the fluid generally is not turned through the full angle provided by the shape of the guide vanes. With this flow deviation angle calculation, the actual flow direction of the air leaving the vanes (and entering the seal) can be determined. Hence, the magnitude and direction of the inlet velocity is known, and the appropriate component is the measured inlet circumferential velocity.

The entrance pressure-loss coefficient, defined in equation (6), is determined from the measured pressures just upstream of and just inside the seal. An entrance Mach number is calculated in the same manner as outlined previously, using the measured pressure immediately inside the seal and the annular area between the rotor and stator. This entrance Mach number, and the ratio of the seal entrance/guide vane exit pressures are substituted into equation (6), and the entrance loss coefficient, \bar{k} , is determined.

DATA ACQUISITION AND REDUCTION

With the preceding explanations of how the seal parameters are varied, and how these parameters are measured, the discussion of how the raw data is processed and implemented can begin. Data acquisition is directed from a Hewlett-Packard 9816 (16-bit) computer with disk drive and 9.8 megabyte hard disk. The computer controls an H-P 6940B multiprogrammer which has 12-bit A/D and D/A converter boards and transfers control commands to and test data from the instrumentation.

As was previously stated, the major data groups are seal motion/reaction force data and fluid flow data. The motion/reaction force data are used for dynamic coefficient identification. The hardware involved includes the load cells, accelerometers, X-direction motion probe, a Sensotec analog filter unit, a tunable bandpass filter, and the A/D converter. The operation of these components is illustrated in Fig.18, and their outputs are used in a serial sampling scheme which provides the computer with the desired data for reduction. Recalling the discussion of the reaction force measurements in the preceding section, a (stator mass) \times (stator acceleration) subtraction from the indicated load cell forces is necessitated due to vibration of the stator and test section housing. This subtraction is performed with an analog circuit, and results in corrected F_x and F_y force components due to relative seal motion.

The forced oscillatory shaking motion of the seal rotor is the key to the operation of the serial synchronous sampling (SSS) routine which is employed. The frequency of the rotor oscillation is set by a function generator, and rotor motion is sensed by the X-direction motion probe.

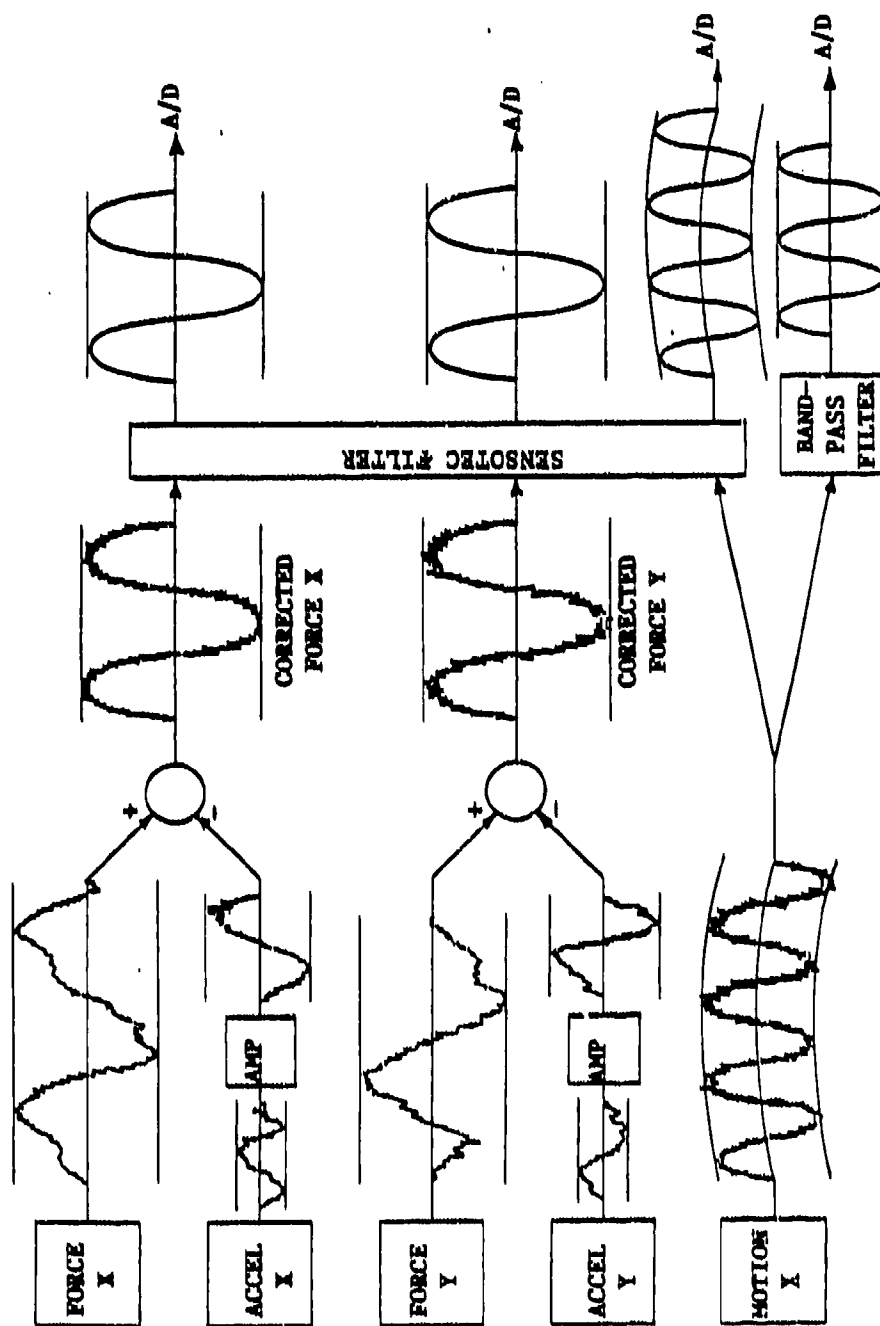


Fig. 18 Signal conditioning schematic for data acquisition.

The motion signal is filtered by the narrow bandpass filter, and is used as a trigger signal for the SSS routine. Upon the operator's command, the SSS routine is enabled, and the next positive-to-negative crossing of the filtered motion signal triggers a quartz crystal clock/timer. Ten cycles of the corrected $F_x(t)$ signal are sampled, at a rate of 100 samples/cycle. The second positive-to-negative crossing of the filtered motion signal triggers the timer and initiates the sampling of ten cycles of the $F_x(t)$ signal. Finally, the third positive-to-negative crossing triggers the timer again, and ten cycles of the corrected $X(t)$ signal are sampled. Thus, at every test condition, 1000 data points are obtained for $F_x(t_1)$, $F_y(t_1)$, and $X(t_1)$, and the data arrays are stored in computer memory.

Some important points need to be stressed concerning this force/motion data acquisition. First, the bandpass filter is used only to provide a steady signal to trigger the timer/clock. Any modulation of the motion signal due to rotor runout is eliminated by this filter, as long as the rotational frequency and shaking frequency do not coincide. Therefore, the shaking frequencies are selected to avoid coincidence with running speeds. However, the rotor motion and corrected force signals which are sampled and captured for coefficient identification are filtered only by a low-pass filter (500 Hz cutoff), and the effects of runout as well as shaking motion are present in the recorded data. A second point worth noting is that the sample rate is directly dependent on the shaking frequency. As the shaking frequency is increased, the sample rate (samples/second) also increases. In order to get the desired 100 samples/cycle, shaking frequencies must be chosen to correspond to discrete sample rates which are available. Hence, the

frequency at which the rotor is shaken is carefully chosen to provide the desired sampling rate and a steady trigger signal.

Most of the fluid flow data are used for the input parameters required by Nelson's analysis. The upstream (reservoir) pressure and temperature, downstream (sump) pressure, and the inlet circumferential velocity (determined as outlined earlier) are provided directly. The friction-factor values of the rotor and stator are supplied in the form of Hirs coefficients, which are obtained from the pressure distribution data in the manner described below.

Recalling the discussion of Hirs' turbulent bulk-flow fluid model, the model assumes that the wall shear stresses can be written as in equation (4). For the gas seals discussed here, an adiabatic, compressible flow with friction analysis is employed, and the measured pressure gradient and mass flow rate (leakage) data are used to calculate a friction factor coefficient, λ , for each test condition. From the λ versus R_m and w data, the Hirs coefficients m_r , n_r of the friction factor formula

$$\lambda = n_r R_m^{m_r} [1 + 1 / 4b^2]^{(1+m_r)/2}, \quad b = U / R_w \quad (20)$$

are calculated on a least-square basis. For the smooth-rotor/smooth-stator combination, the values are assumed to apply for both the rotor and stator. Hence, for this case, $m_r = m_s$ and $n_r = n_s$.

For the smooth-rotor/honeycomb-stator combination, a combined λ is measured, which is related to the rotor λ_r and (honeycomb) stator λ_s by

$$\lambda_0 = (\lambda_r + \lambda_s) / 2 \quad (21)$$

and hence,

$$\lambda_s = 2\lambda_0 - \lambda_r \quad (22)$$

Therefore, λ_s is determined from measured data for λ_o and a calculated value for λ_r from Equation (21) with experimentally determined values for m_r and n_r . Then, as before, the λ_s versus R_a and ω data are used to calculate the Hirs coefficients for the honeycomb stator.

As stated previously, the Hirs coefficients for the seal rotor and stator are required input parameters for Nelson's analysis, as are the fluid flow conditions up and downstream of the seal and the rotational speed of the rotor. The appropriate input parameters for each specific test case can be provided for Nelson's analysis from static test results and measurements. In this manner, a point-by-point comparison of theoretical predictions to experimental results can be made for leakage through the seal, axial - pressure distribution, entrance - loss coefficient, and rotordynamic coefficients.

TEST PROCEDURES

At the start of each day's testing, the force, pressure, and flowmeter systems are calibrated. The total system, from transducer to computer, is calibrated for each of these variables. The force system calibration utilizes a system of pulleys and known weights applied in the X and Y-directions. An air-operated dead-weight pressure tester is used for pressure system calibration, and flowmeter system calibration is achieved with an internal precision quartz clock which simulates a known flowrate.

All of the tests performed to date have been made with the rotor executing small motion about a centered position. A typical test begins by centering the seal rotor in the stator with the Zonic hydraulic shaker, starting airflow through the seal, setting the rotational speed of the rotor, and then beginning the shaking motion of the rotor. Data points are taken at rotational speeds of 200, 500, and 1000-8000 rpm, in 1000 rpm increments. At each rotational speed, the inlet pressure is varied and data points are taken at one unchoked flow and four choked flow conditions. For each test case (i.e., one particular running speed, shaking frequency, inlet pressure, and prerotation condition), the measured leakage, rotordynamic coefficients, axial pressure distribution, and entrance loss coefficient are determined and recorded.

This test sequence is followed for each of three different shaking frequencies, and for three inlet swirl directions (with rotor rotation, opposite rotation, and no rotation). Therefore, fifty data points are taken per test (i.e. one shaking frequency and inlet swirl combination),

with a total of nine tests (for small motion about a centered position) made per seal.

RESULTS

The test results reported here were developed as part of an extended, joint NASA-USAF funded research program for annular gas seal studies. Tests were carried out on a smooth-rotor/smooth-stator seal and a smooth-rotor/honeycomb-stator seal. The dimensions and pertinent data for each are included in Table 1. The honeycomb stator insert, provided by the Rocketdyne division of Rockwell International, is the turbine interstage seal of the HPOTP (High-Pressure Oxygen Turbopump) of the SSME (Space Shuttle Main Engine). Fig. 19 illustrates the honeycomb configuration.

The test program had the following objectives:

- 1) Acquire leakage, friction factor, and entrance-loss data for smooth and honeycomb seals.
- 2) Compare predictions from current theory to test results.
- 3) Compare the stability performances of a smooth-rotor/honeycomb-stator and a smooth constant-clearance annular seal.

The Hirs coefficients for both seals were determined in the manner described previously. The values of these coefficients are listed in Table 2. Relative roughness values based on measured Hirs coefficients as suggested by Colebrook [22] are also included. Colebrook's formulation,

$$(4 \text{ ns} R_a \text{ ms})^{-1/2} = -2 \log \left(\left((\epsilon/2C) / 3.7 \right) + \left(2.51 / (R_a \sqrt{4 \text{ ns} R_a \text{ ms}}) \right) \right) \quad (23)$$

is a curve-fit of experimental data obtained for fluid flow through pipes with various wall roughnesses. The appropriate stator coefficients are substituted to obtain the relative roughness $(\epsilon/2C)$

Table 1. Test seal specifications.

	<u>Smooth-rotor/ smooth stator</u>	<u>Smooth-rotor/ honeycomb stator</u>
<u>Rotor</u>		
Diameter:	15.136 cm (5.959 in)	14.453 cm (5.690 in)
Material:	304 Stainless steel	304 Stainless steel
Surface roughness:	0.102 μ m (4 μ in)	0.127 μ m (5 μ in)
<u>Stator</u>		
Diameter:	15.283 cm (6.017 in)	14.614 cm (5.754 in)
Material:	304 Stainless steel	6061-T6 Aluminum
Surface roughness:	0.140 μ m (5.5 μ in)	1.575 mm (0.062 in) Comb
Radial clearance:	0.7366 mm (29 mil)	0.8065 mm (31.8 mil)
Seal length:	5.080 cm (2.00 in)	2.540 cm (1.00 in)

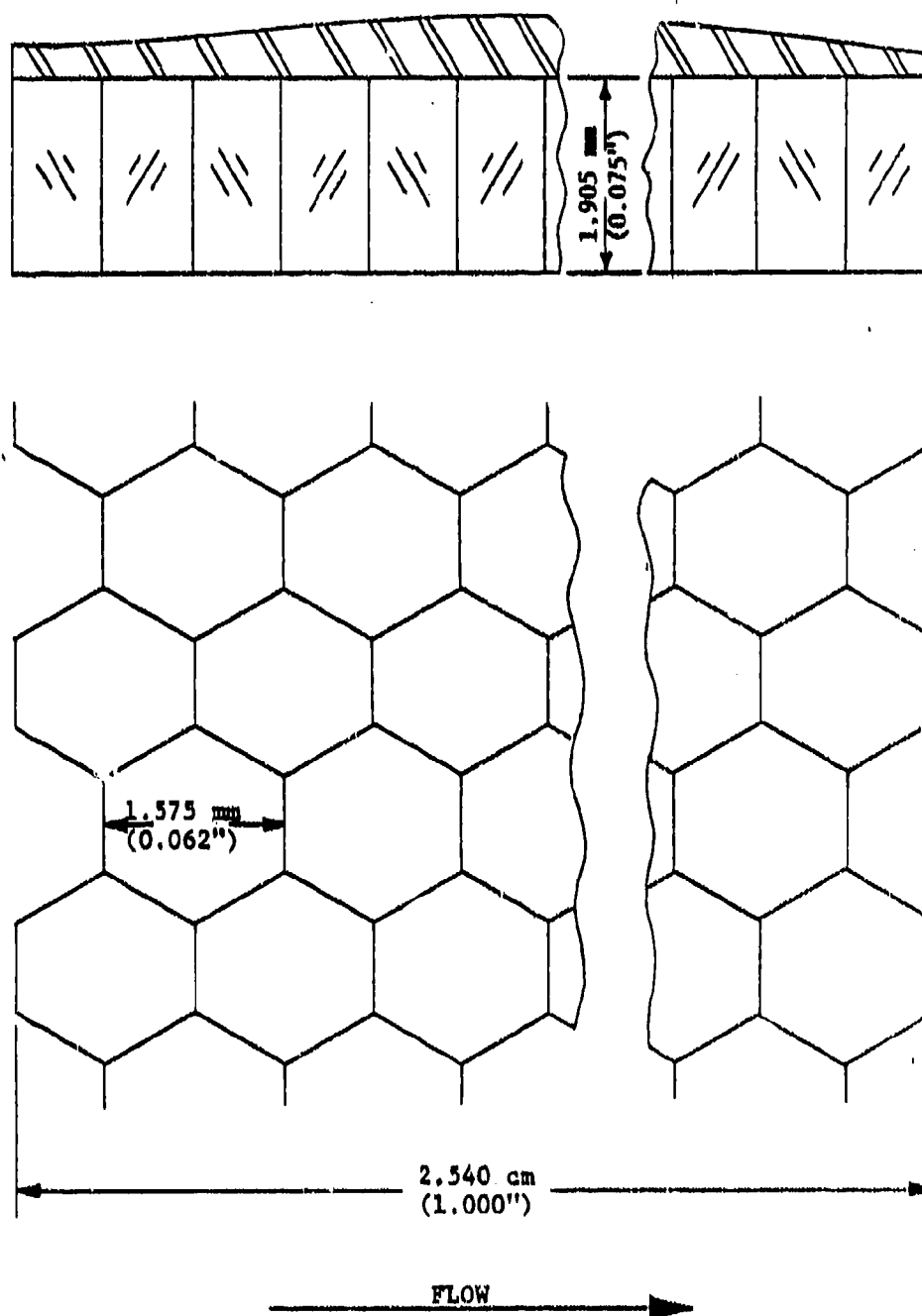


Fig. 19 Honeycomb stator insert detail.

Table 2. Friction-factor data.

	<u>Smooth-rotor/ smooth-stator</u>	<u>Smooth-rotor/ honeycomb-stator</u>
<u>Hirs coefficients</u>		
Rotor ns:	0.187	0.187
Rotor ms:	-0.333	-0.333
Stator ns:	0.187	0.187
Stator ms:	-0.333	-0.0778
<u>Relative roughness $\epsilon/2C$</u>		
Rotor:	1.44×10^{-4}	1.44×10^{-4}
Stator:	1.44×10^{-4}	4.93×10^{-4}

(Note: The relative roughness values shown are averages over an axial Reynolds number range of 20,000 - 80,000.)

140

values. It should be noted that friction factor data for honeycomb seals have not been previously published.

The results provided here are grouped in static (leakage, pressure distribution, entrance loss coefficient) and dynamic (rotordynamic coefficient) sections. A one-to-one comparison of the smooth and honeycomb seal configuration is precluded, however, due to differences in seal length, nominal clearance, and inlet guide vane configuration, as illustrated in Figs. 12 and 14.

Static Results. Figs. 20 and 21 and Table 3 show a comparison of the theoretical and experimental leakage through the seal for various fluid prerotation conditions. The figures show the leakage at various pressure ratios (reservoir pressure / sump pressure). In the table, the leakage has been averaged over all speeds and pressure ratios, and is presented in ratio form (Theory/Experiment). The comparison shows that for both the smooth and the honeycomb seal, leakage is underpredicted for the non-prerotated case. Conversely, for fluid prerotation either in or opposing the direction of rotor rotation, the leakage is overpredicted for both seals. The maximum error is approximately 7.5%, occurring for the smooth seal with prerotation in the direction of rotor rotation. Average error for the smooth seal is 1.7%, and for the honeycomb seal is 1%.

The pressure gradient plots are included in Figs. 22-28. Fig. 22 illustrates the negligible effect of running speed on the pressure distribution in the seal. This plot has ten curves (corresponding to the ten rotational speed increments) plotted. This accounts for the heavy lines which appear in some cases. This particular plot is of the experimental data for the non-prerotated smooth seal case, however,

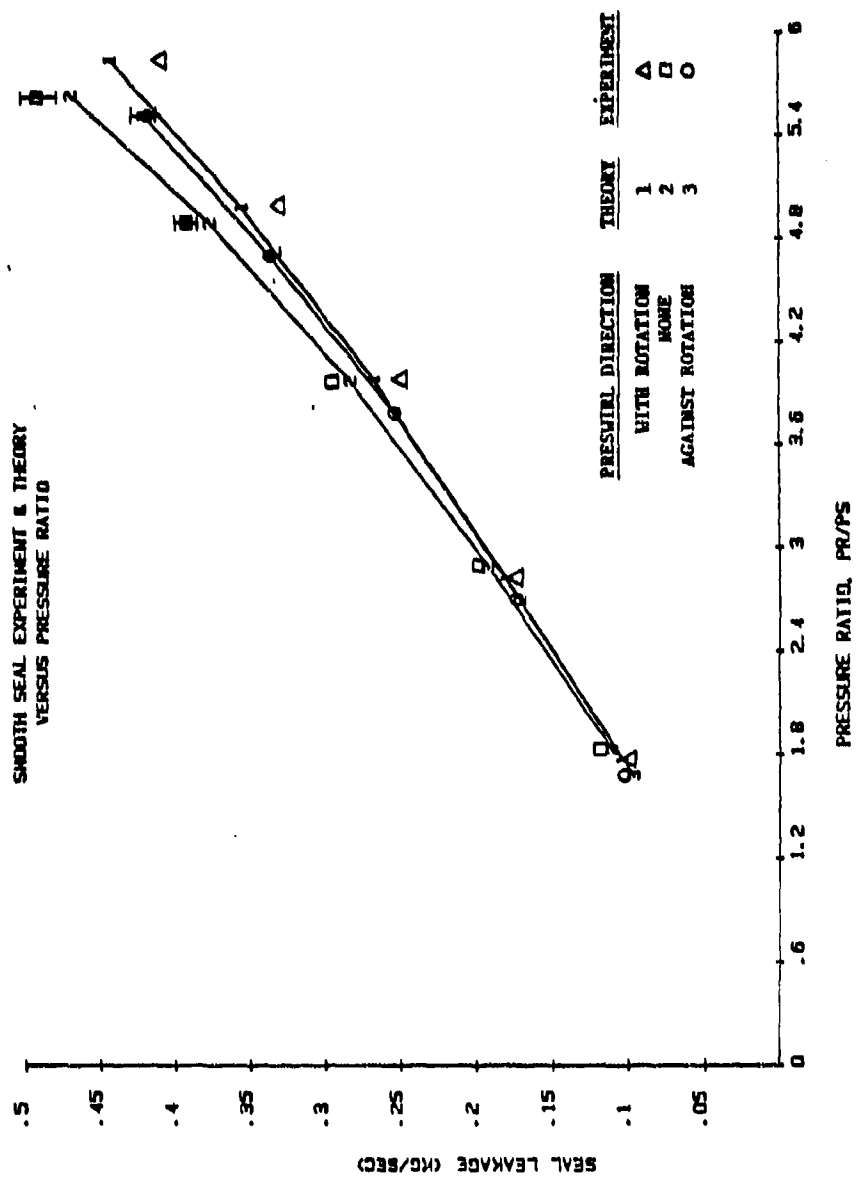


Fig. 20 Smooth seal leakage.

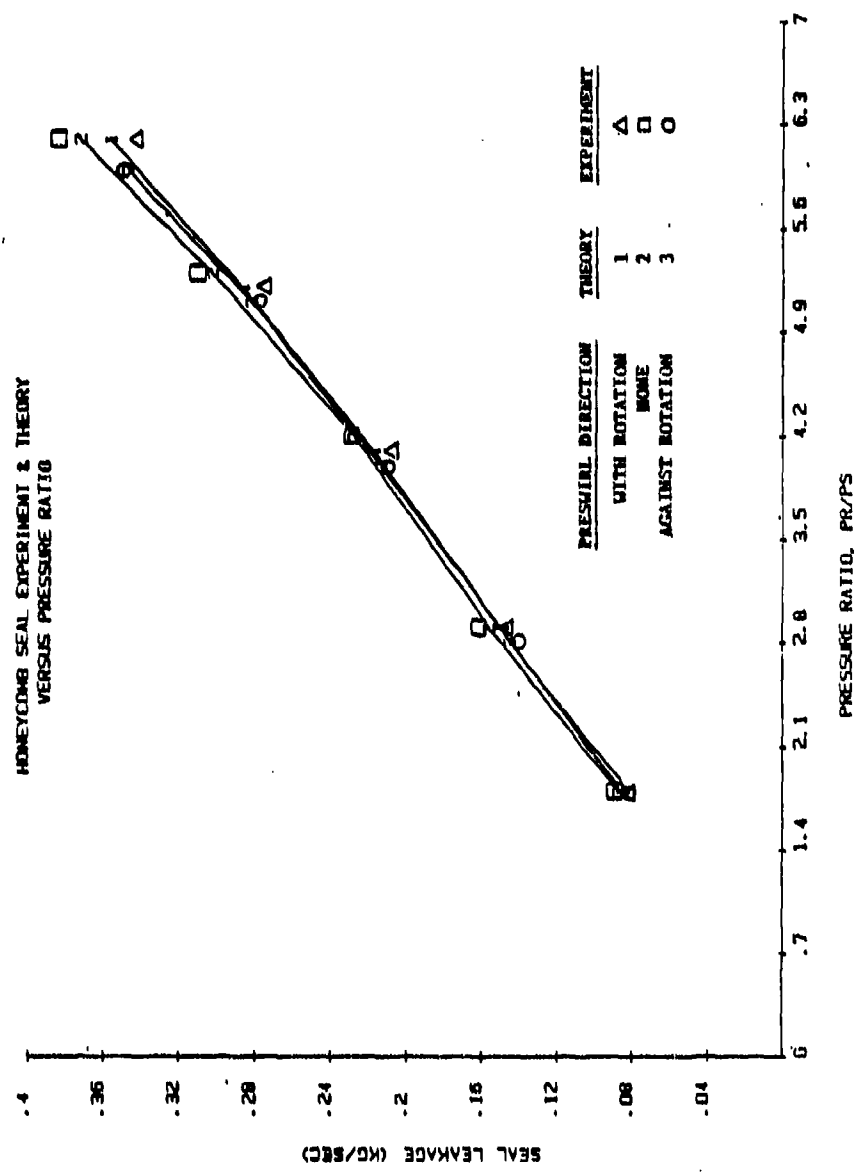


Fig. 21 Honeycomb seal leakage

Table 3. Theory versus experiment leakage comparison.
(Theory/Experiment)

<u>Fluid prerotation direction</u>	<u>Smooth-rotor/ smooth-stator</u>	<u>Smooth-rotor/ honeycomb-stator</u>
With rotor rotation	1.075	1.047
(standard deviation)	0.012	0.008
No prerotation	0.9684	0.9712
(standard deviation)	0.012	0.005
Opposite rotor rotation	1.007	1.013
(standard deviation)	0.012	0.004

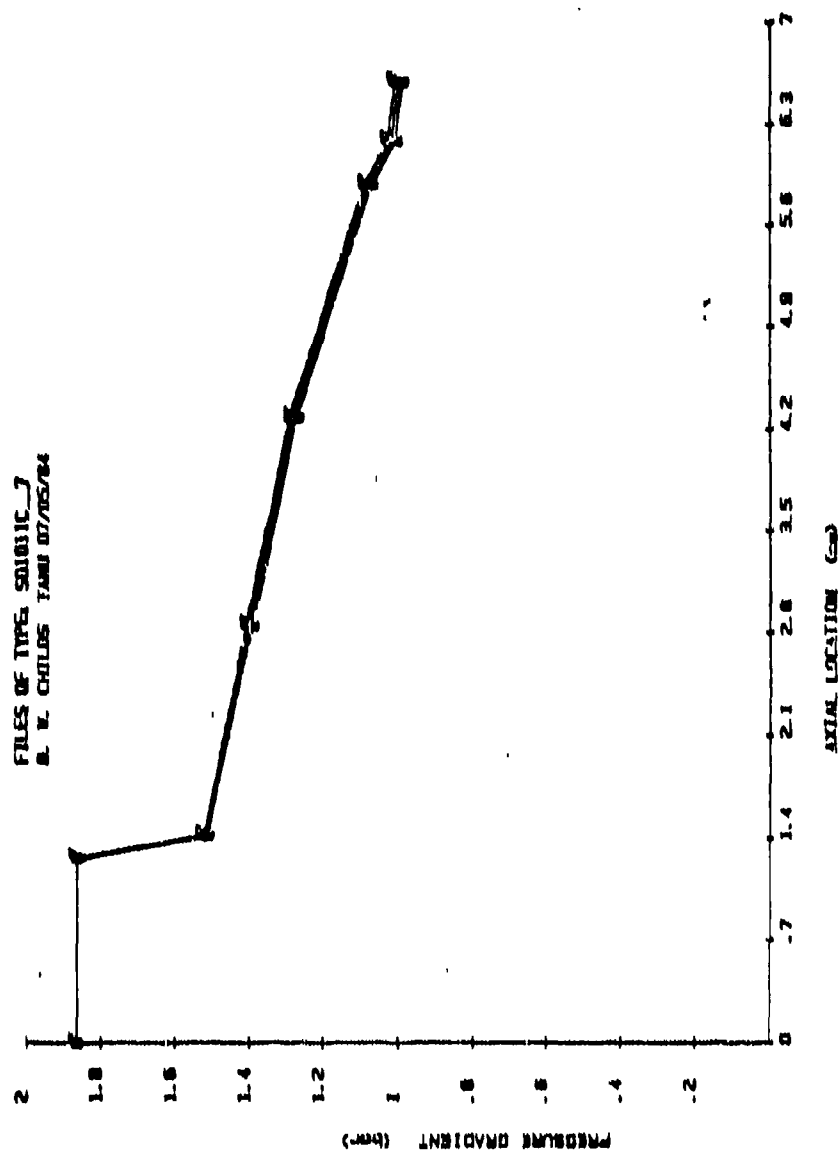


Fig. 22 Axial pressure gradient in smooth seal with no prerotation, unchoked flow, ten running speeds.

none of the pressure plots show any appreciable variation due to running speed.

Figs. 23-28 show the theoretical and experimental pressure data for each of the seals under various prerotation conditions. Due to the absence of running speed dependence, only one speed is plotted for each inlet pressure condition. The numbers on the plotted lines refer to the inlet pressure, where 1 corresponds to approximately 186.9 kPa (12.4 psig), and 2 through 5 correspond to 308.2 kPa (30 psig), 446.1 kPa (50 psig), 584.0 kPa (70 psig), and 721.9 kPa (90 psig), respectively. The lowest pressure corresponds to unchoked flow through the seal, while the others are choked. The shapes of the pressure-gradient plots show fairly good correspondence between theory and experiment. This to be expected, however, since the Hirs' coefficients used in the analysis come directly from the measured pressures. The best agreement occurs for the non-prerotated flow in both the smooth and honeycomb seals. For prerotated flow in either direction, the theoretical gradient is shifted up slightly for both seal configurations. This upward shift is partly due to a total pressure correction that is made. When the flow is prerotated by the guide vanes, it is accelerated as well as turned, and the measured static pressure at the vane exit decreases. This explains why the experimental plots show lower seal entrance pressures for either prerotated case than for the non-prerotated case. Nelson's analysis, however, assumes that the supply pressure upstream of the seal is the total pressure. Hence, the axial component of the fluid velocity as it leaves the guide vanes is used to calculate an effective total pressure, which is higher than the measured static pressure. This corrected pressure is then input as the reservoir pressure to Nelson's analysis.

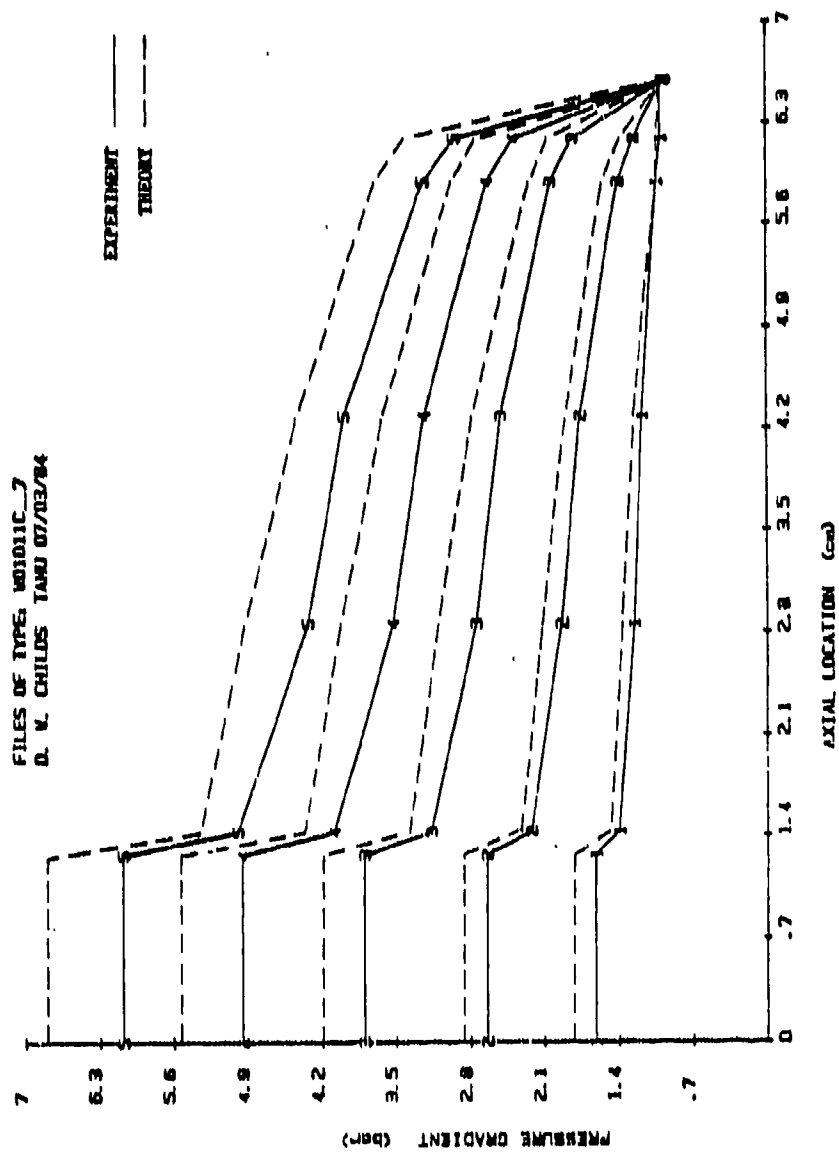


Fig. 23 Axial pressure gradient in smooth seal with prerotation in the direction of rotor rotation.

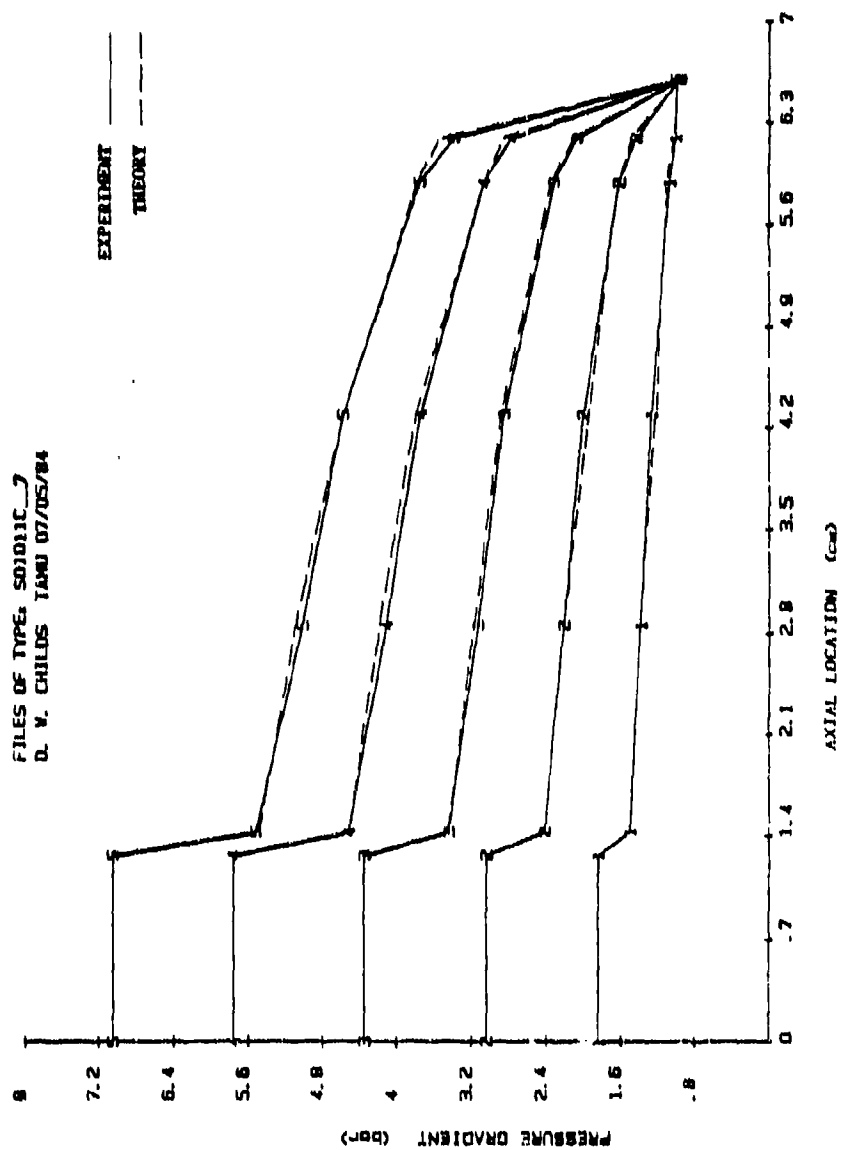


Fig. 24 Axial pressure gradient in smooth seal with no prerotation.

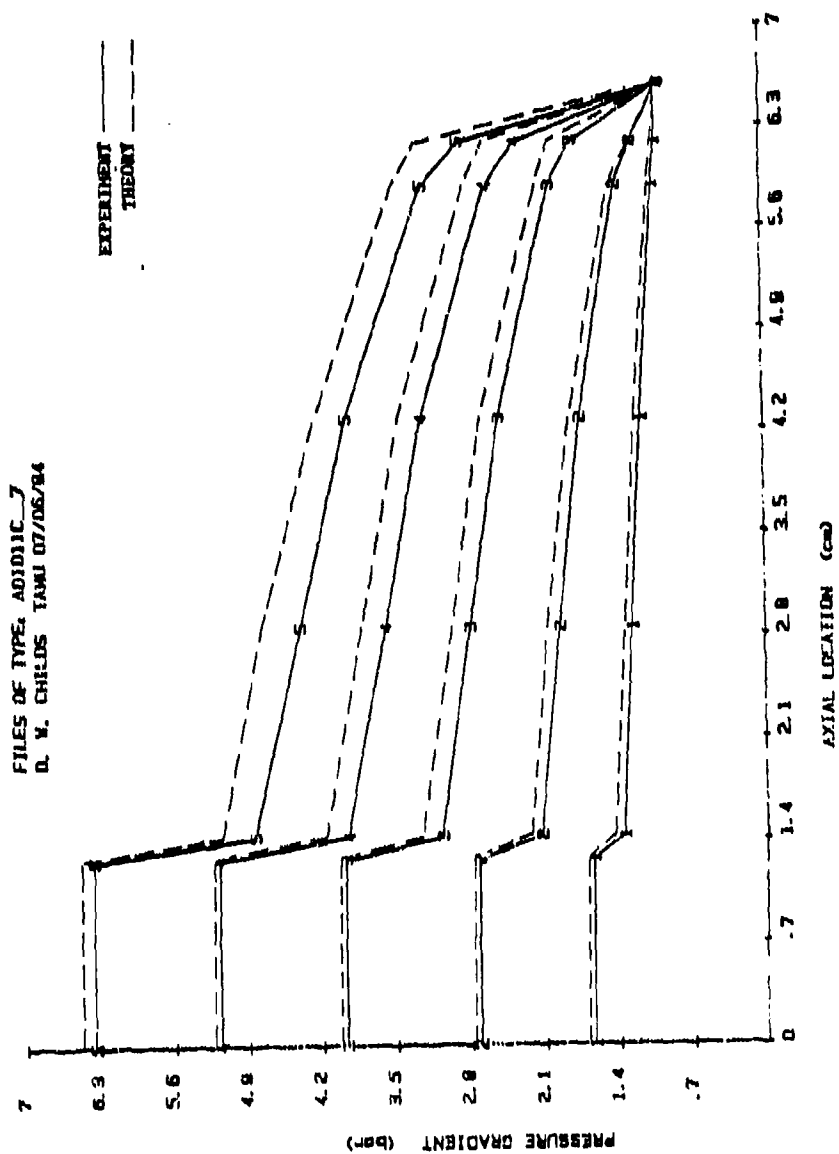


Fig. 25 Axial pressure gradient in smooth seal with prerotation opposing rotor rotation

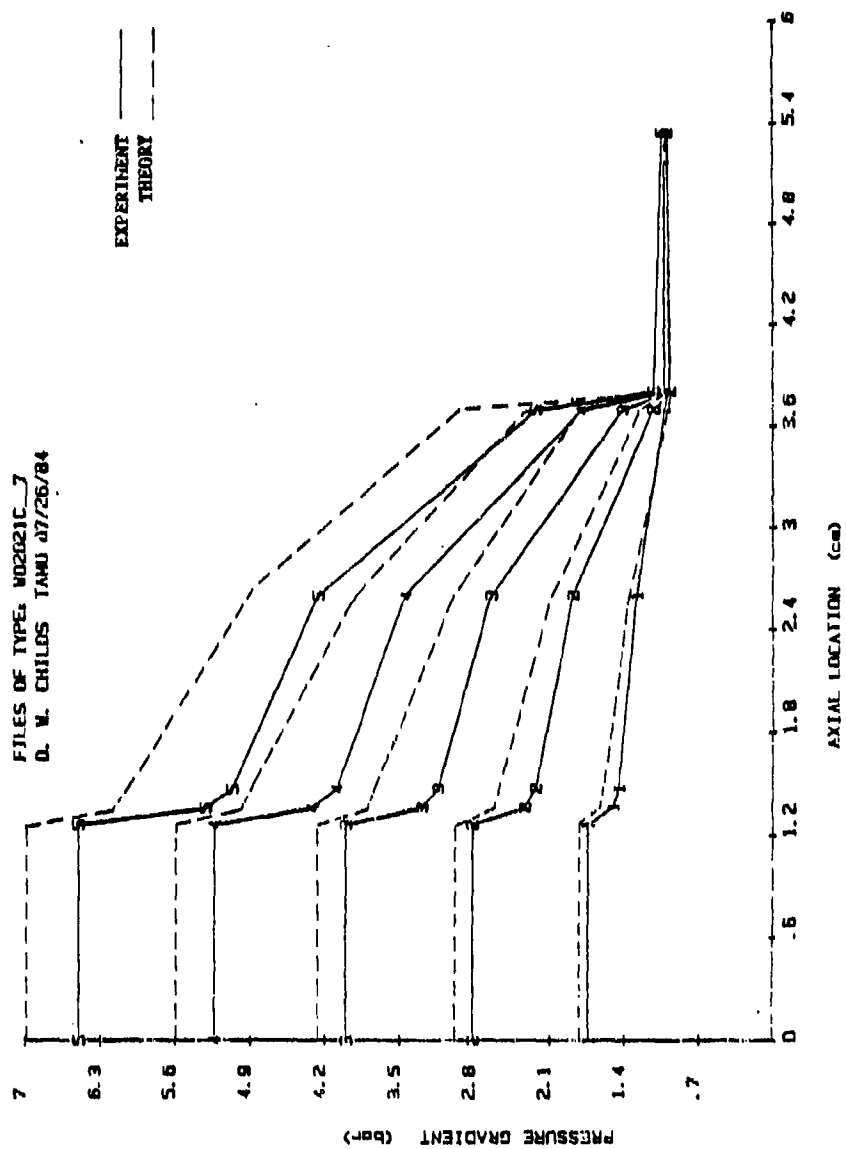


Fig. 26 Axial pressure gradient in honeycomb seal with prerotation in the direction of rotor rotation.

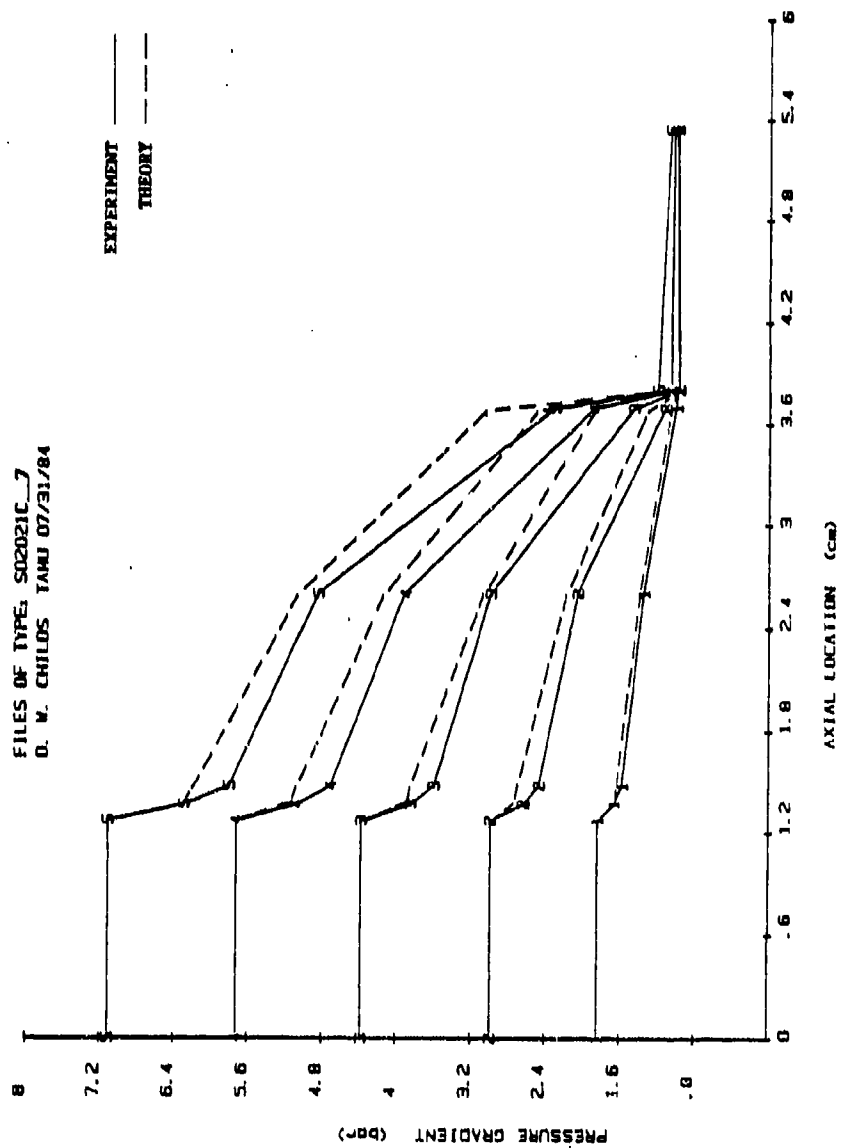


Fig. 27 Axial pressure gradient in honeycomb with no prerotation.

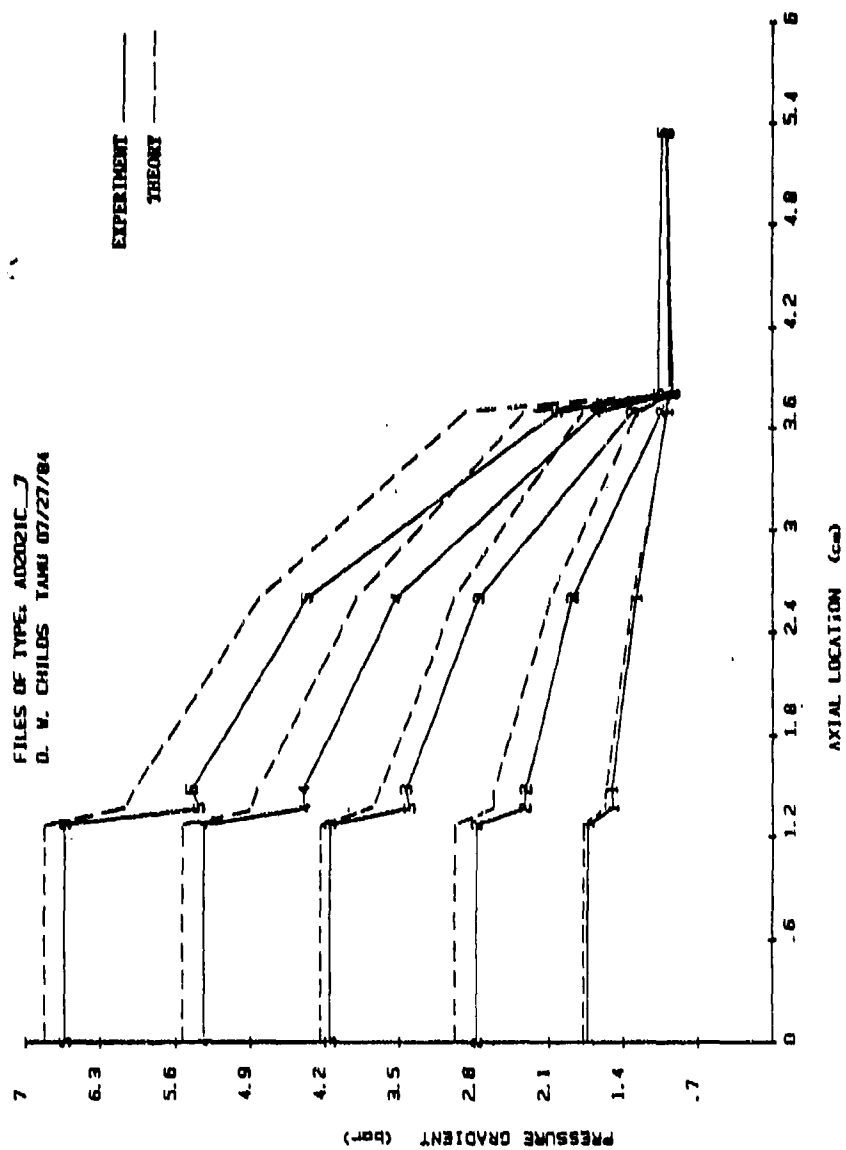


Fig. 28 Axial pressure gradient in honeycomb seal with prerotation opposing rotor rotation.

The entrance loss coefficient, \bar{K} , also may have some bearing on the upward shift seen in some of the pressure gradient plots. Plots of $(\bar{K}+1)$ versus axial Reynolds number are included in Figs. 29-34. Ten experimental curves, corresponding to running speed are plotted on each. Recalling Deissler's curve fit employed by Nelson and plotted in Fig. 3, experimental results show loss terms $(\bar{K}+1)$ significantly higher than those predicted for both prerotated honeycomb seal cases. Agreement between theory and experiment is fairly good for the non-prerotated cases for both seals. For the smooth seal with prerotation in the direction of rotor rotation, the loss coefficient is overpredicted, with the experimental results indicating a negative \bar{K} .

Dynamic Results. Dynamic tests were performed at shaking frequencies of 58.8, 74.6, and 124.6 Hz. As was discussed in the Data Acquisition section of this report, these frequencies were chosen to provide the desired sample rate and a steady trigger signal. The dynamic coefficients obtained at the two lower frequencies are essentially the same. At the 124.6 Hz shaking frequency, however, correspondence of the data to that obtained at the lower frequencies is unsatisfactory. In seeking to explain the discrepancy, tests were run to determine the relative transfer function of the test apparatus. The plots in Fig. 35 show the results of these tests, and indicate a resonance of the apparatus occurring at approximately 25 Hz (the drop in phase difference at approximately 45 Hz corresponds to a resonance of the shaker support structure). As the shaking frequency is increased above this, the input force levels required to achieve a given motion amplitude increase rapidly. At the 124.6 Hz shaking frequency, attainable motion amplitude is about 50% of that achieved at the

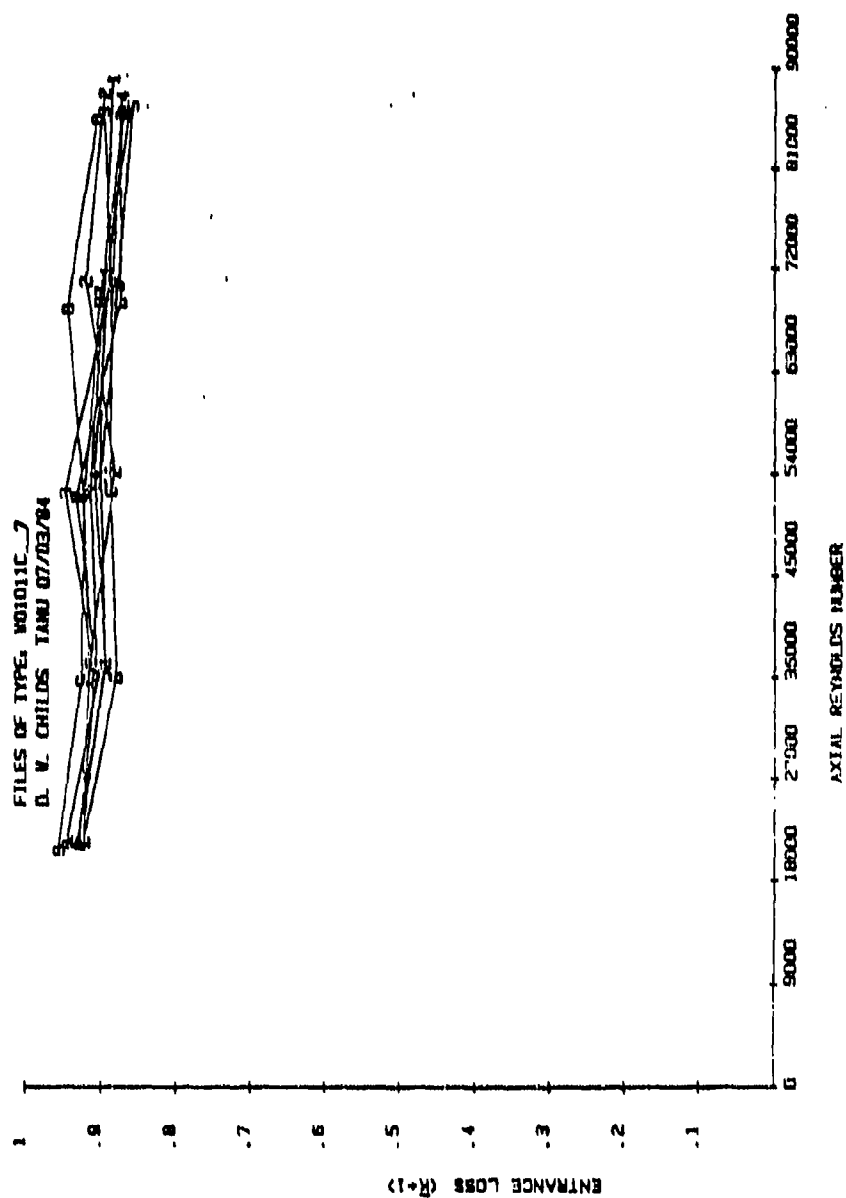


Fig. 29 Entrance-loss for smooth seal, prerotation in direction of rotor rotation.

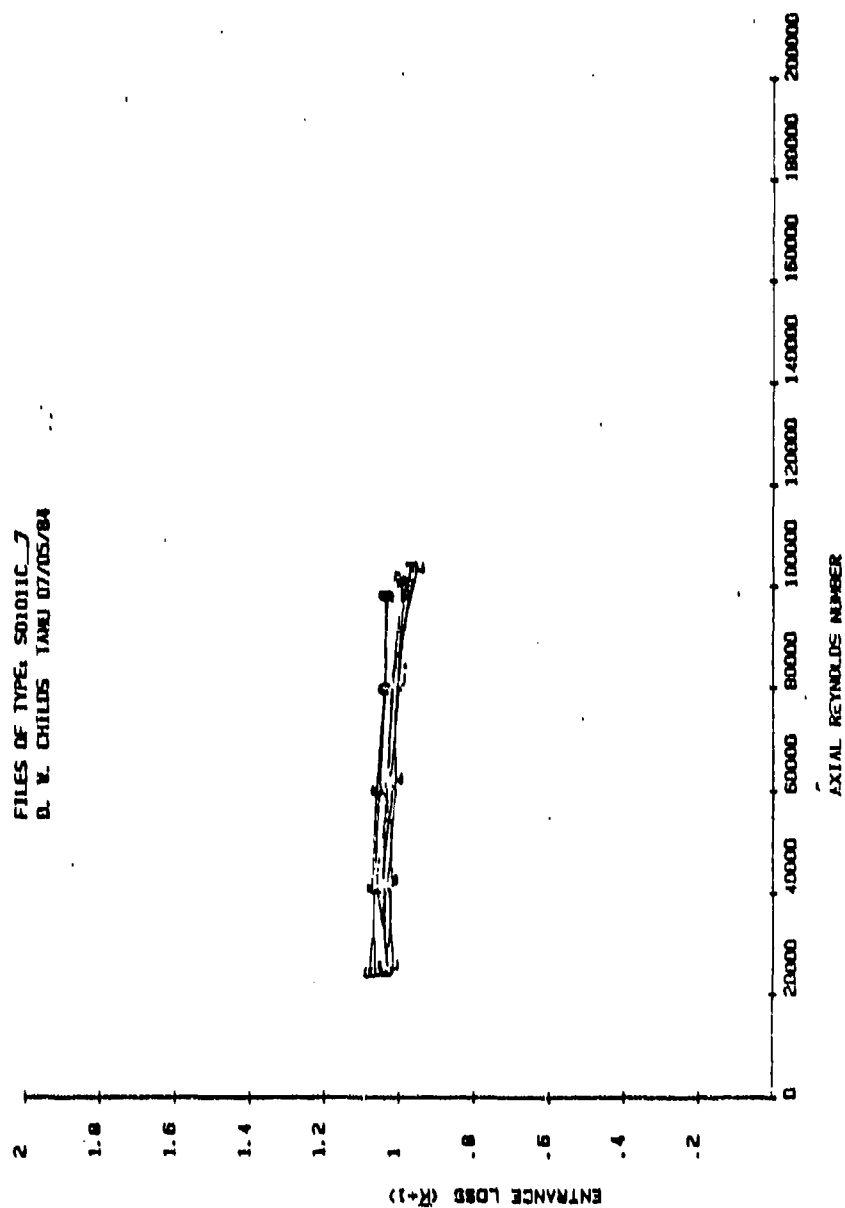


Fig. 30 Entrance-loss for smooth seal, no prerotation.

FILES OF TYPE: A01011E_7
 D. V. CHILDS TAMU 07/06/84

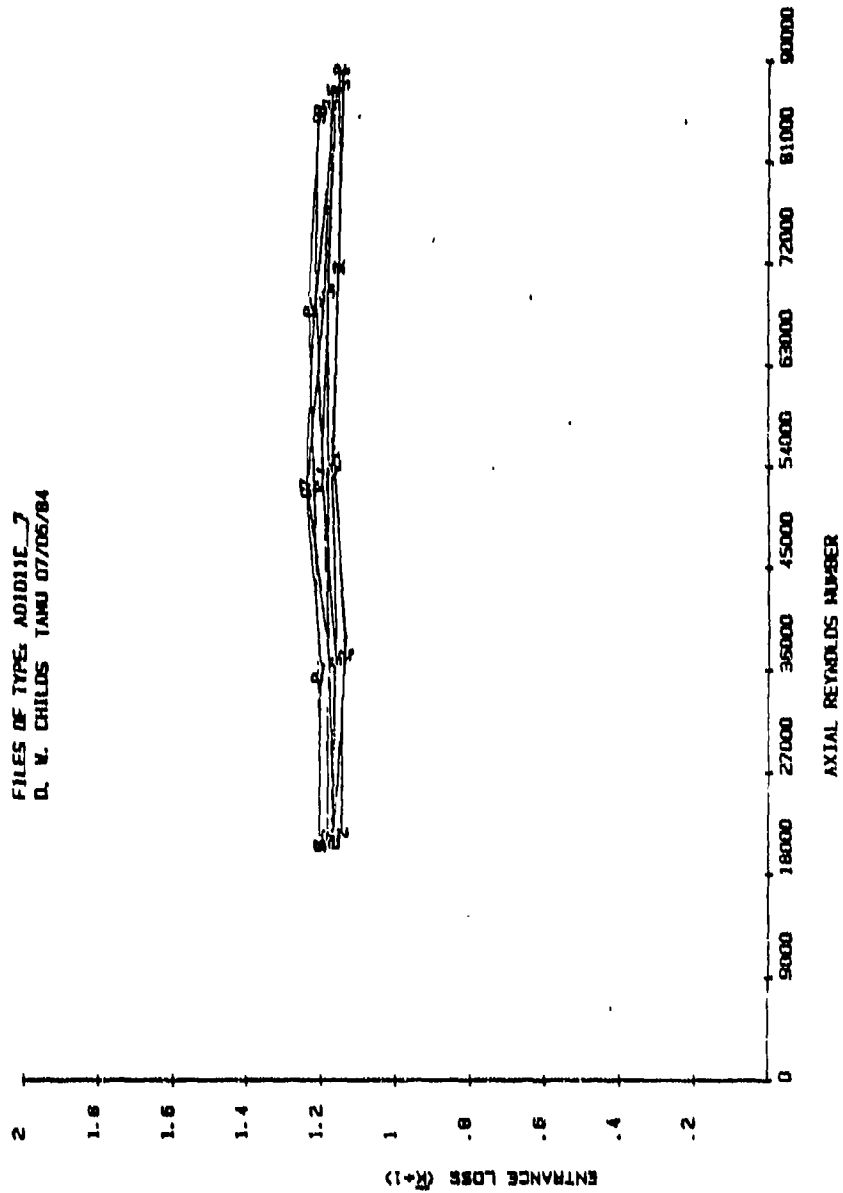


Fig. 31 Entrance-loss for smooth seal, prerotation opposing rotation.

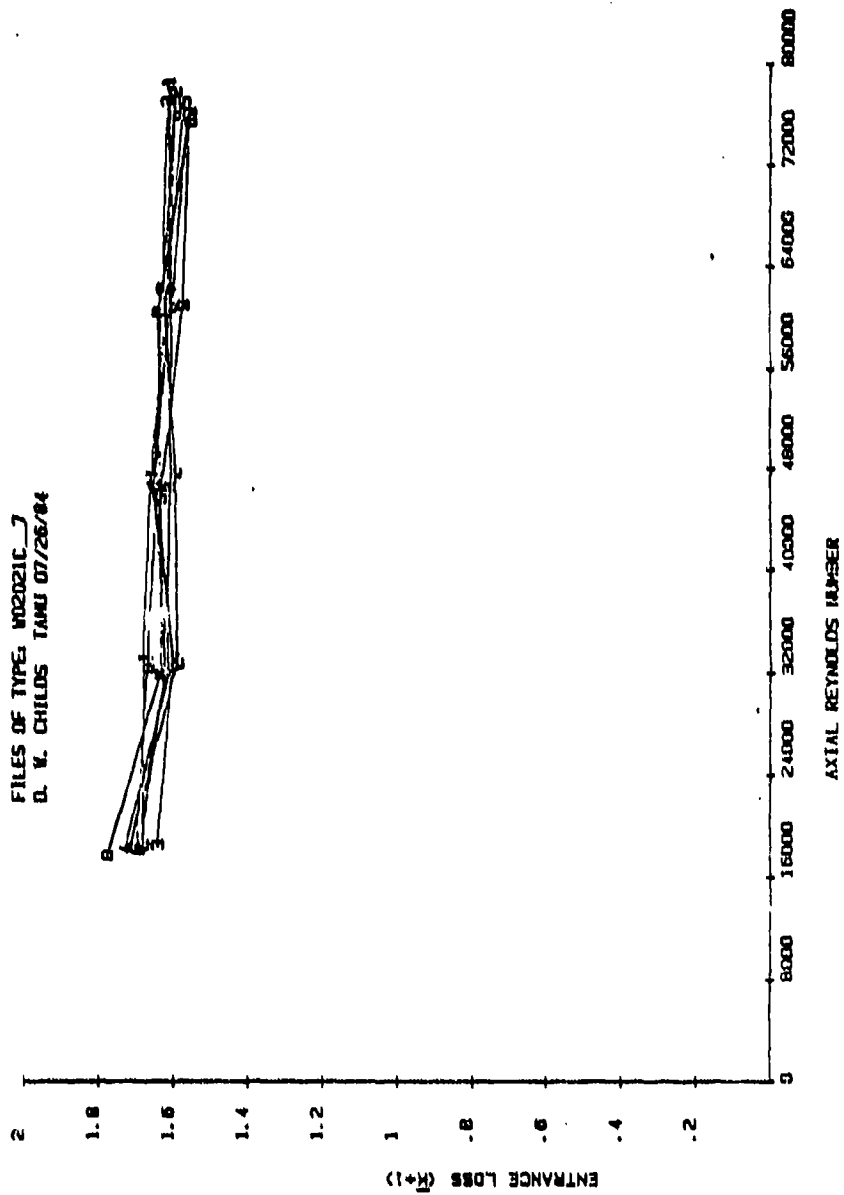


Fig. 32 Entrance-loss for honeycomb seal, prerotation in direction of rotor rotation.

FILES OF TYPE: S02021C-7
D. W. CHILDS JANU 07/31/84

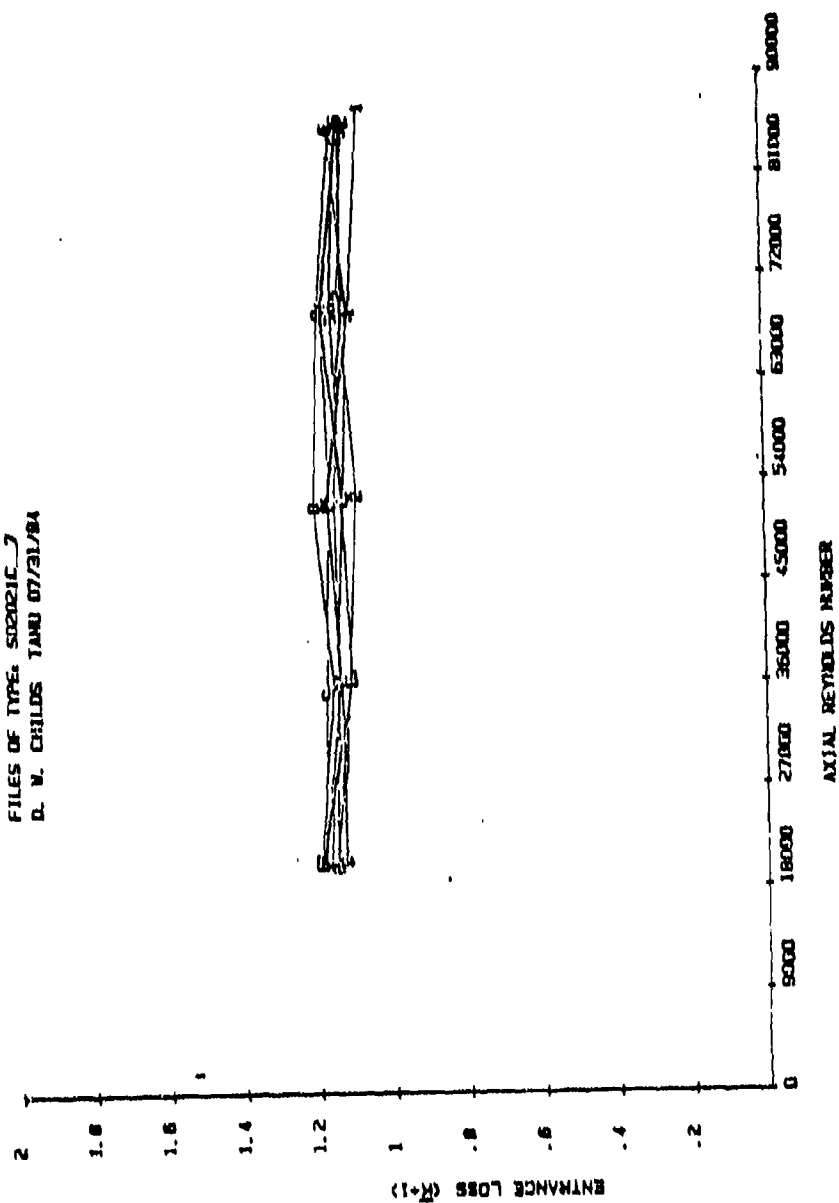


Fig. 33 Entrance-loss for honeycomb seal, no prerotation.

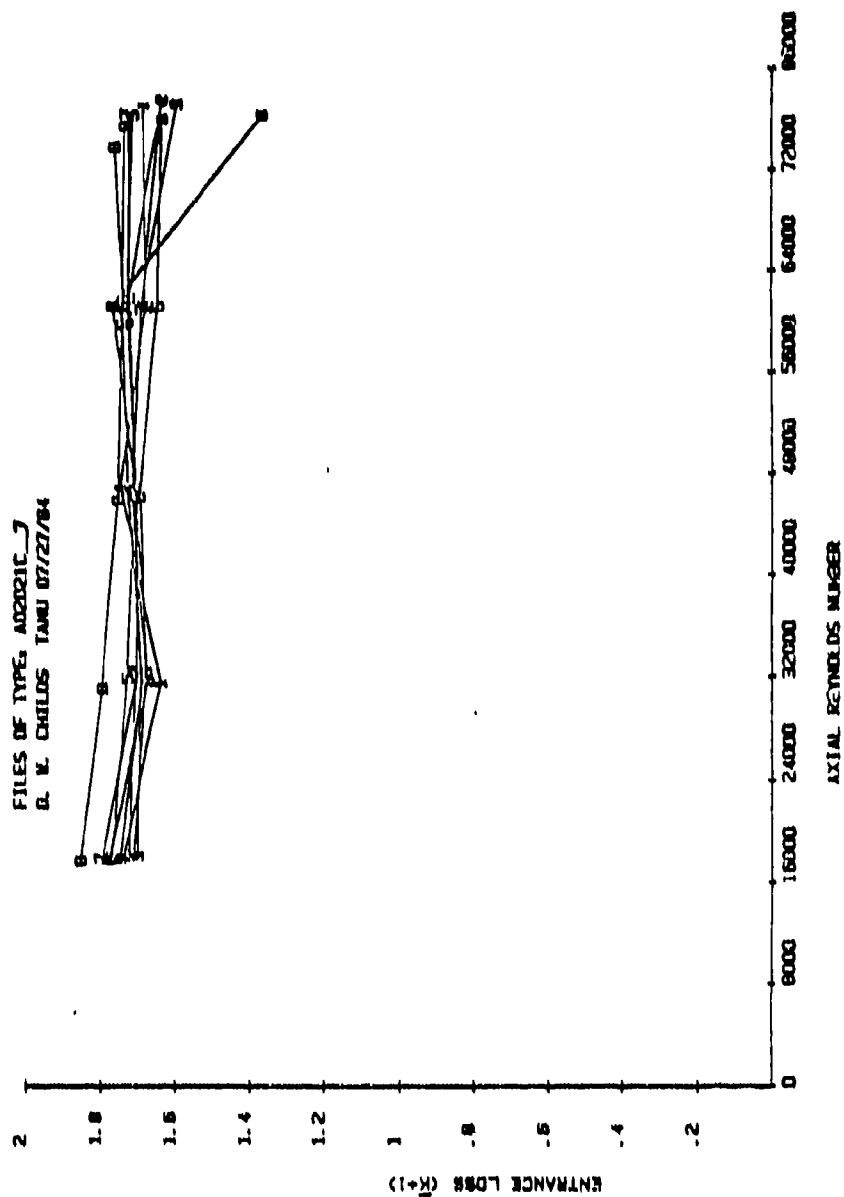


Fig. 34 Entrance-loss for honeycomb seal, prerotation opposing rotor rotation.

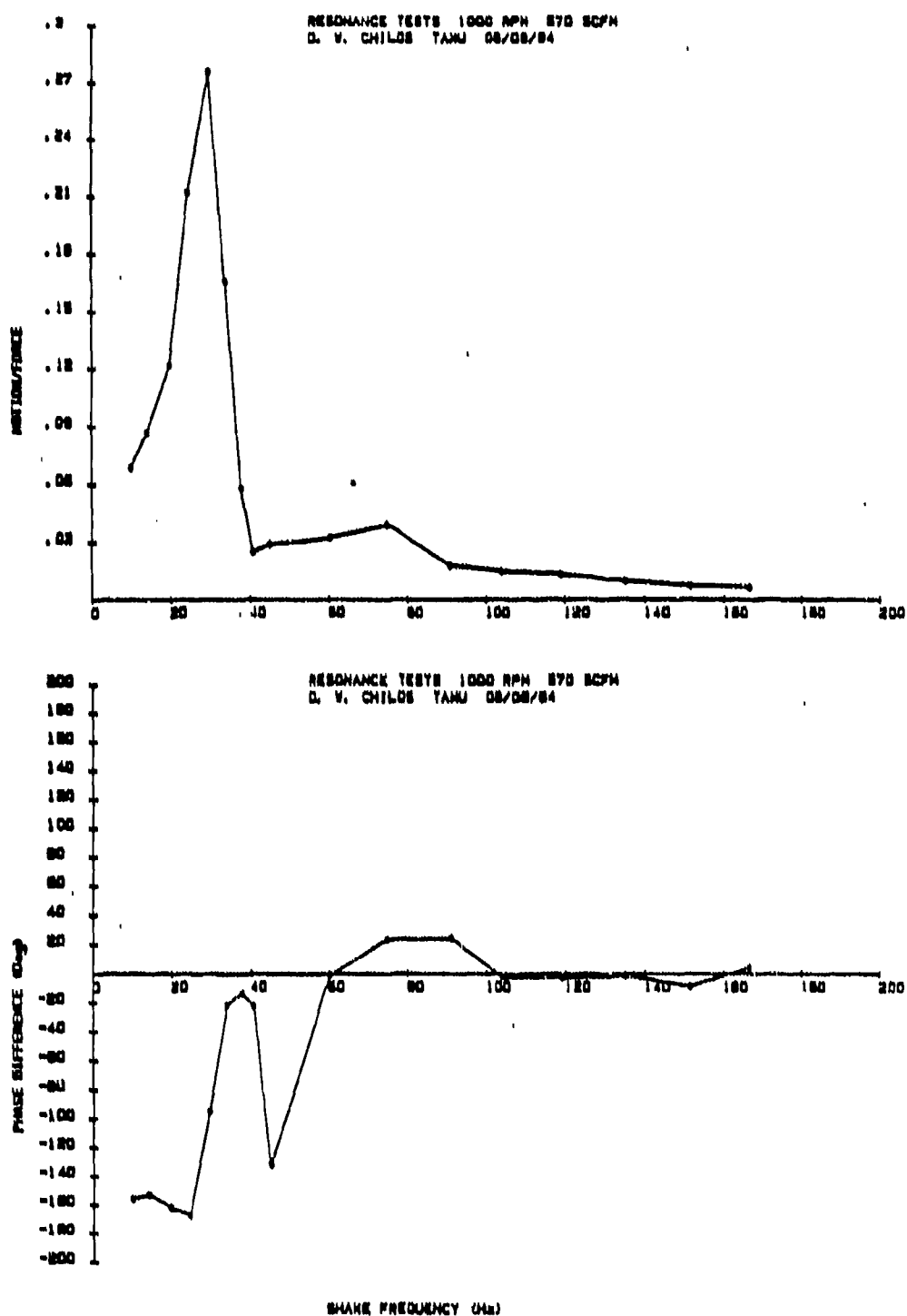


Fig. 35 Relative transfer function of test apparatus.

58.8 and 74.6 Hz frequencies. Therefore, one possible explanation for the poor agreement between the results is that as motion amplitude decreases, so does the force measured by the load cells, and the measurement system resolution suffers.

The plots of the rotordynamic coefficients are found in Figs. 36-43. These plots include both the theoretical and experimental data. The coefficients are plotted versus the reservoir / sump pressure ratio, and the solid lines correspond to the theoretical data. The experimental results are indicated by symbols. The location of the symbols represents the average value of the coefficient (averaged over all of the running speeds) at each particular inlet pressure condition, and the vertical lines drawn through the symbols signify the range over which they varied through the speed range. The test results plotted here were obtained by shaking the rotor with an amplitude of seven mils at 74.6 Hz.

Dynamic Results - Smooth Seal. For the smooth seal, direct stiffness (Fig. 36) is overpredicted for the non-prerotated condition, and underpredicted for both prerotated conditions. Best agreement is seen in the case for prerotation opposite rotor rotation, and the trend of increasing stiffness with increasing pressure ratio compares favorably.

In the cross-coupled stiffness comparison for the smooth seal (Fig. 37), theory overpredicts for both prerotation conditions, and underpredicts for the straight flow case. In every instance, agreement becomes worse with increasing pressure ratio. The non-prerotated case shows a divergence both in magnitude and sign. It should be noted, however, that the magnitudes for this case are significantly smaller than for either of the prerotated cases.

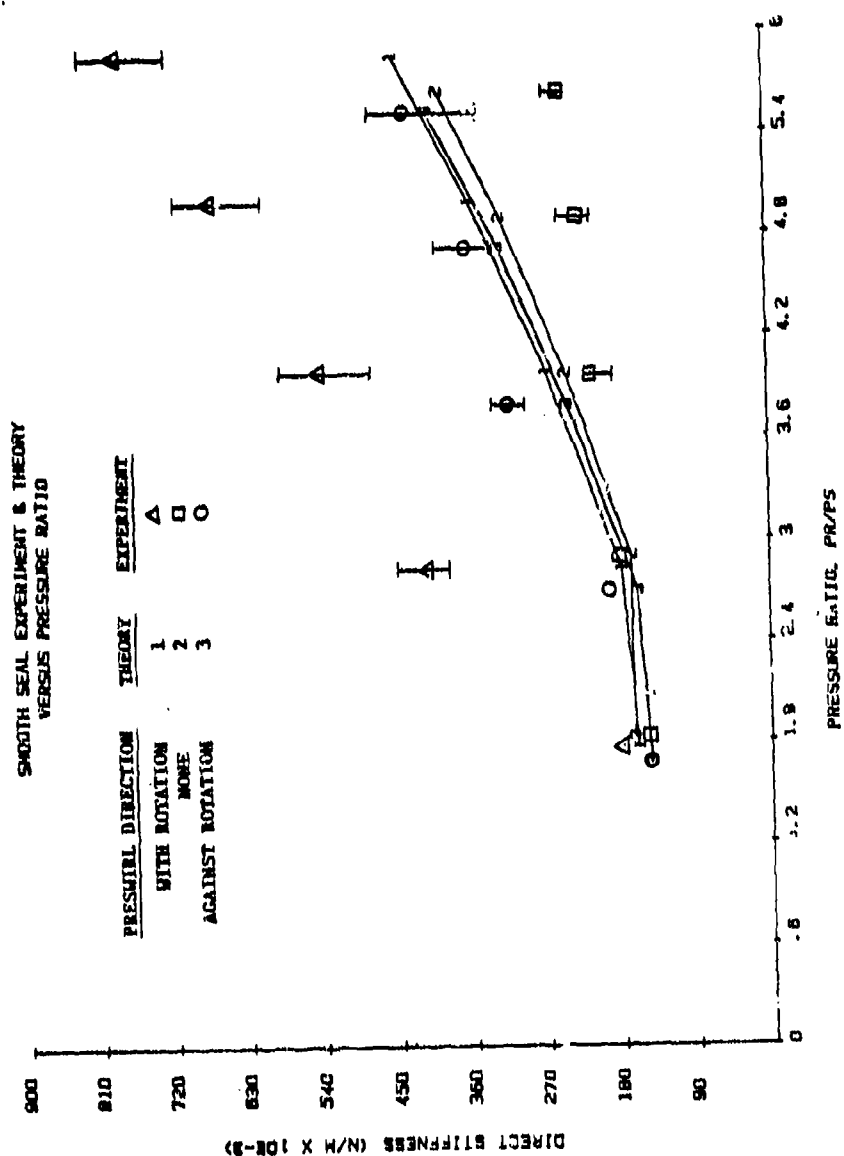


Fig. 36 Direct stiffness of smooth seal.

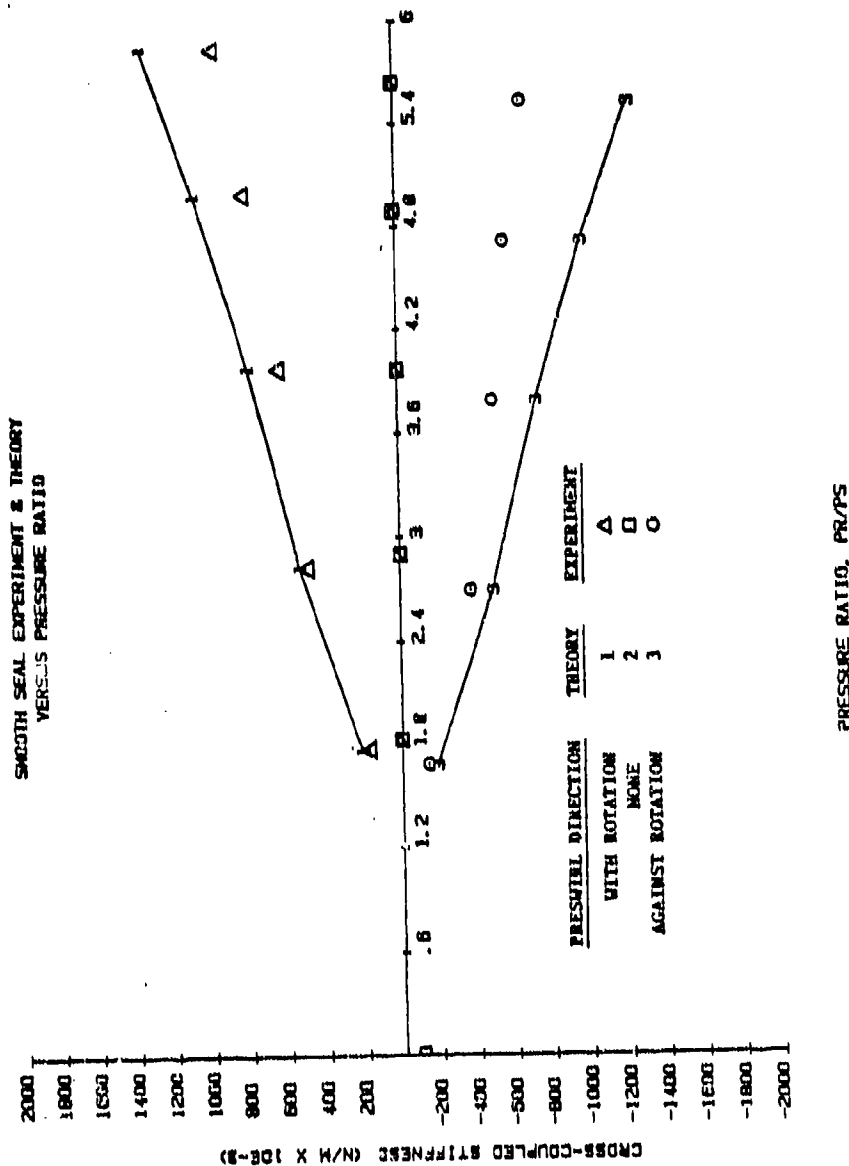


Fig. 37 Cross-coupled stiffness of smooth seal.

Agreement between theory and experiment for direct damping (Fig.38) is the most favorable of all the dynamic coefficients. Direct damping for the smooth seal shows an increase for increasing pressure ratio across the seal, with theory overpredicting slightly for the case of prerotation in the direction of rotor rotation. For the other prerotation conditions, the direct damping is slightly overpredicted at higher pressure ratios.

Cross-coupled damping (Fig.39) for the smooth seal generally shows agreement in the trends for the theoretical and experimental results. For prerotation in and opposing the direction of rotor rotation, the theory underpredicts cross-coupled damping magnitude by approximately 50%, but shows a sign consistent with the test data. For the non-prerotated case, the theory predicts coefficients so small as to be considered negligible. This is not inconsistent with the test results, however, as the magnitudes for this case are significantly smaller than for either prerotated case.

Dynamic Results - Honeycomb Seal. The honeycomb seal data, in general, shows the same correspondence between theory and experiment as the smooth seal. A notable exception, however, is in the direct stiffness coefficient (Fig.40). For both prerotated cases, the predicted stiffness decreases with increasing pressure ratio, while the measured stiffnesses increase. This same predicted decreasing trend is shown for the non-prerotated case at the lower pressure ratios.

In the cross-coupled stiffness comparison (Fig.41), the theory underpredicts the magnitudes, but correctly predicts the signs of the coefficients. For the non-prerotated case, the predicted stiffnesses are essentially zero. The relative magnitudes of the experimental

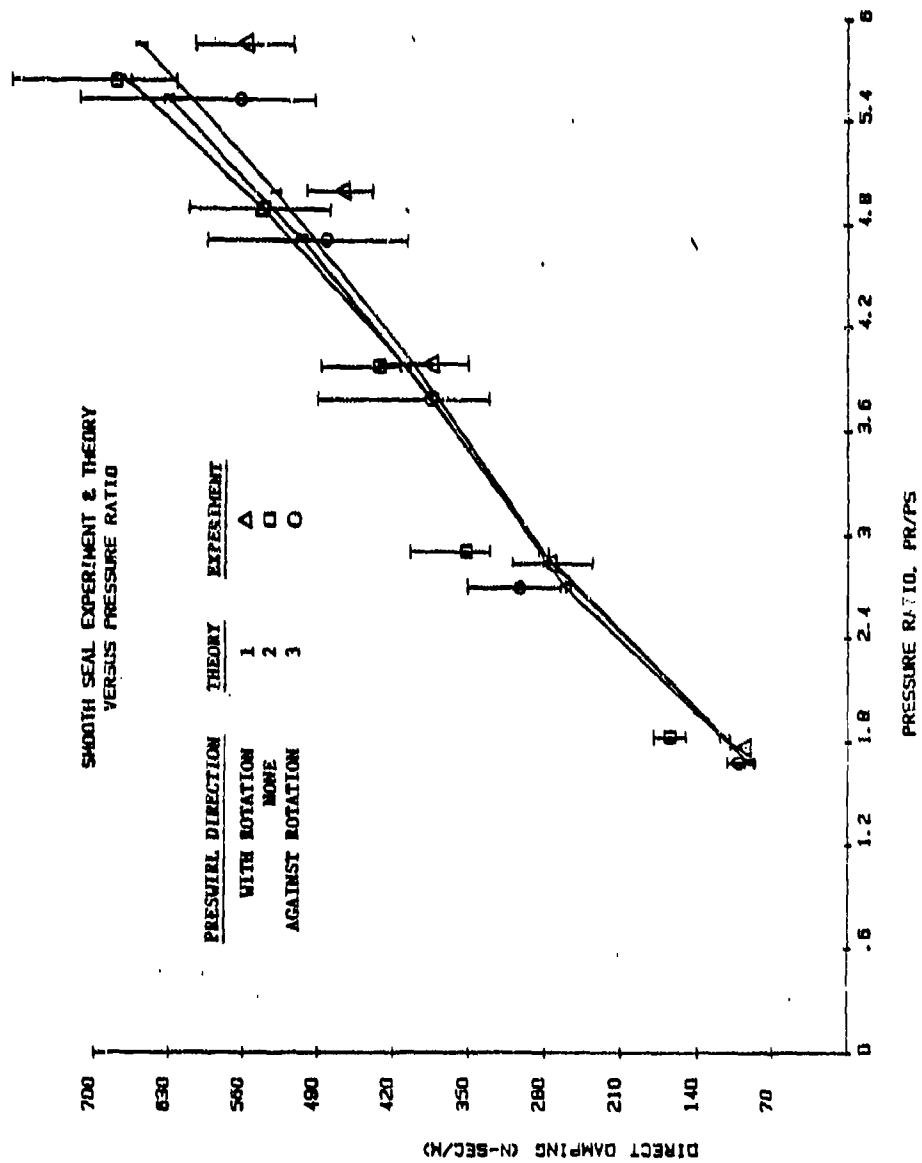


Fig. 38 Direct damping of smooth seal.

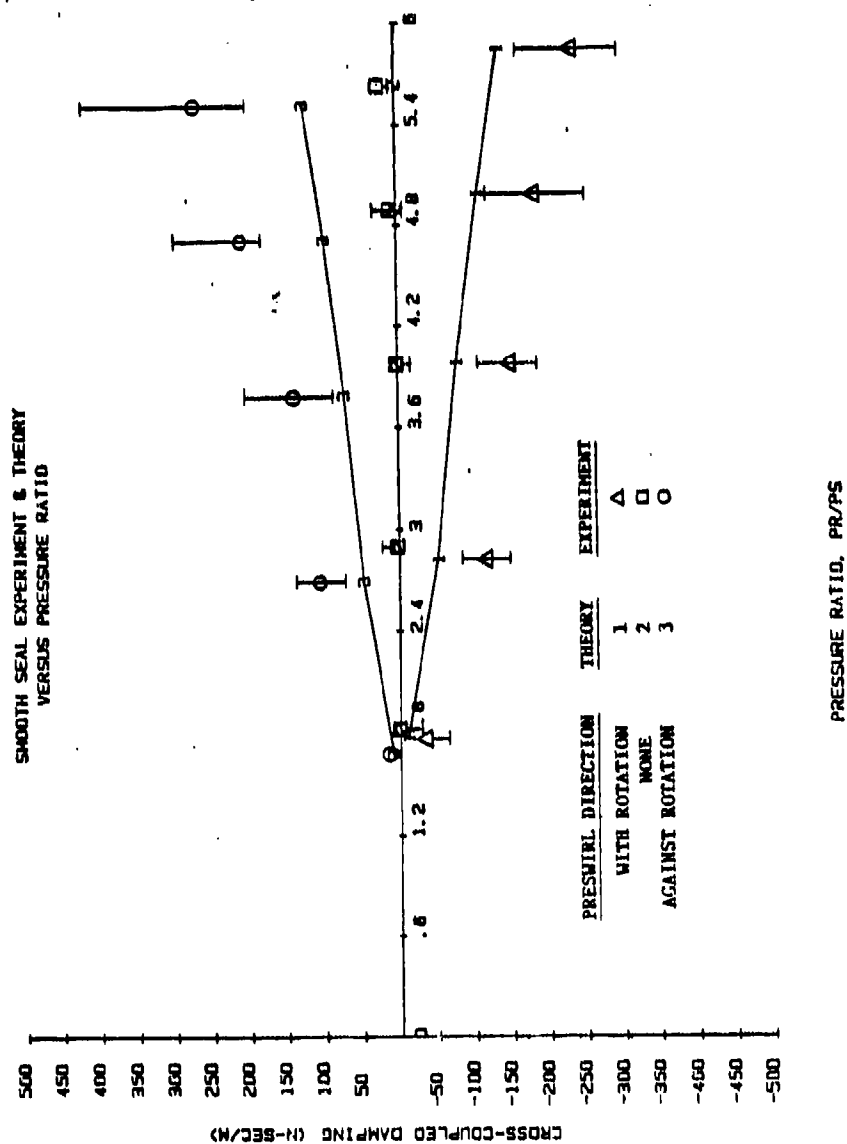


Fig.39 Cross-coupled damping of smooth seal.

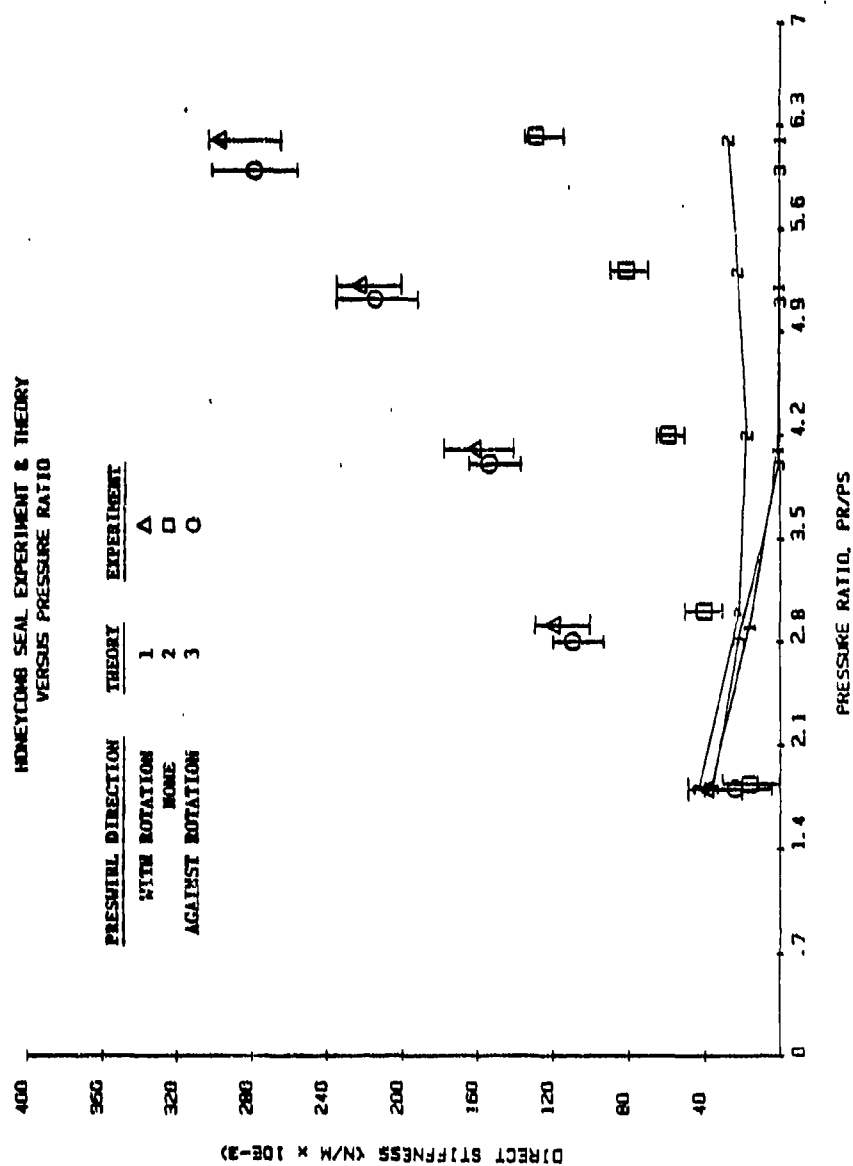


Fig. 40 Direct stiffness of honeycomb seal.

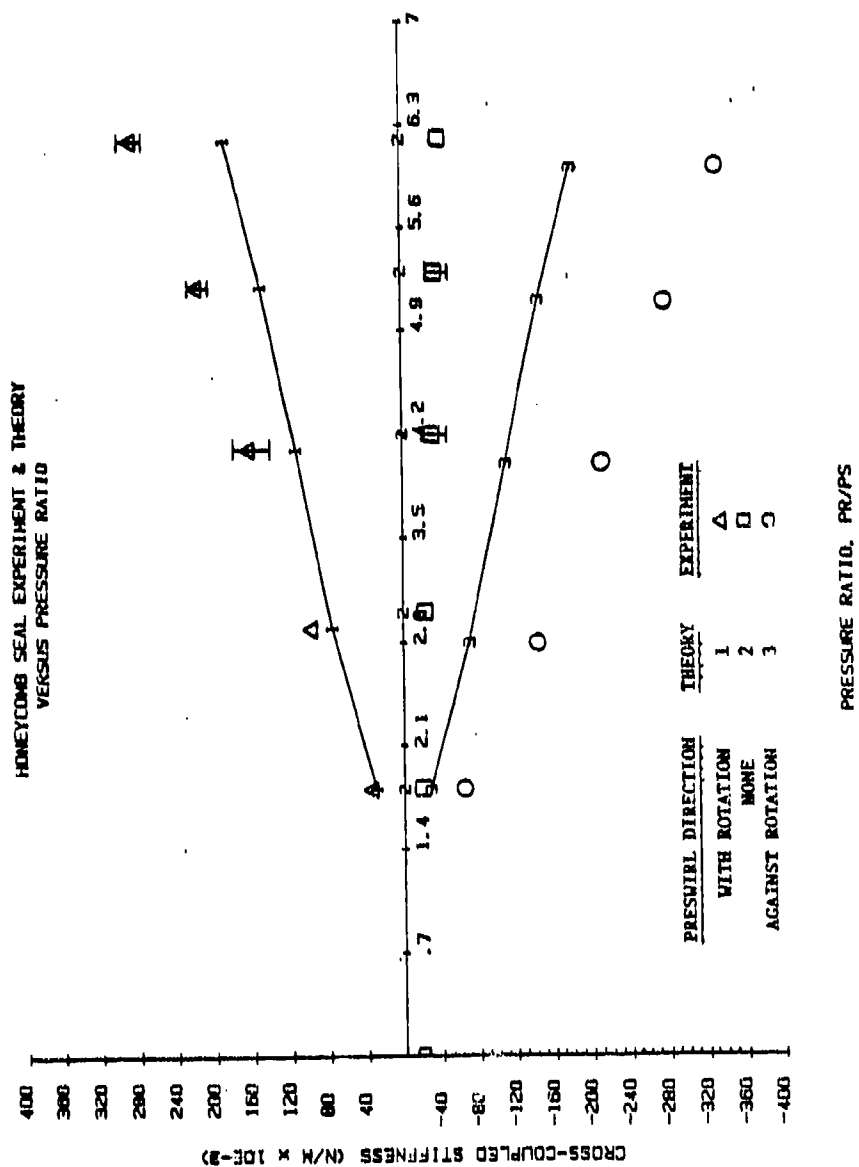


Fig. 41 Cross-coupled stiffness of honeycomb seal.

results for this same case in comparison to either prerotated case are also quite small, however. For prerotation in the direction of rotor rotation, theoretical cross-coupled stiffnesses are approximately 25% less than experimental ones. For counter prerotation, theory underpredicts by about 50%.

With the exception of the non-prerotated case, agreement between theory and experiment is fairly good for the direct damping coefficients (Fig.42) of the honeycomb seal. In the non-prerotated case, theory underpredicts the coefficients by approximately 46%. The prerotated cases show agreement to within approximately 10%.

Theoretical results for the cross-coupled damping coefficients (Fig.43) of the honeycomb seal are small enough to be considered negligible. In every case, the theory underpredicts the coefficients by a wide margin. However, the trend of increasing magnitude with increasing pressure ratio, as well as the signs of the coefficients, agree.

One method in which the dynamic coefficients of the smooth and honeycomb seals can be directly compared is through their respective non-dimensional whirl frequency ratios. Whirl frequency ratio is defined

$$\text{Whirl frequency ratio} = k / C\Omega ,$$

where Ω is the shaking frequency. This ratio is a measure of the destabilizing influence of the cross-coupled stiffness with respect to the stabilizing influence of direct damping. Plots of whirl frequency ratio versus running speed are included in Fig.44. The smooth seal plot shows a small, positive whirl frequency ratio over most of the running speed range. The honeycomb seal plot, however, shows a negative whirl frequency ratio. The negative sign arises due to a

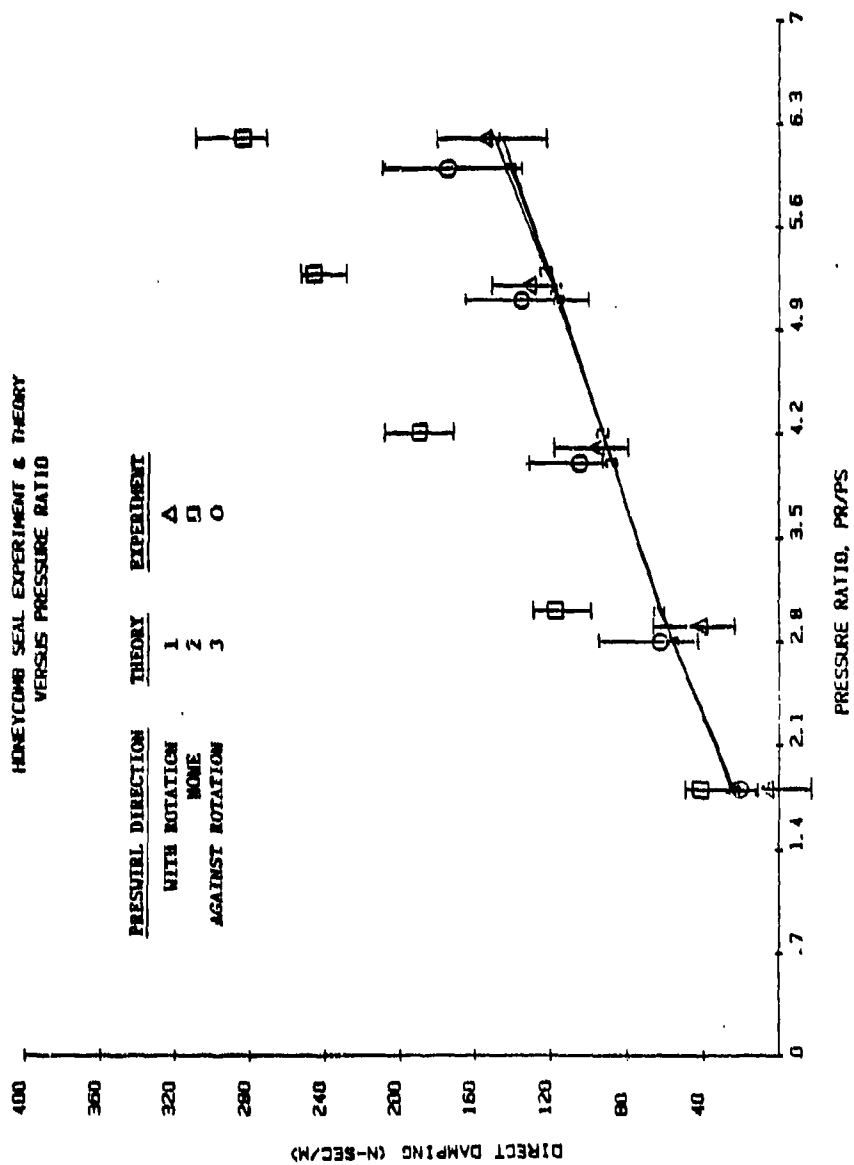


Fig. 42 Direct damping of honeycomb seal.

HONEYCOMB SEAL EXPERIMENT & THEORY VERSUS PRESSURE RATIO

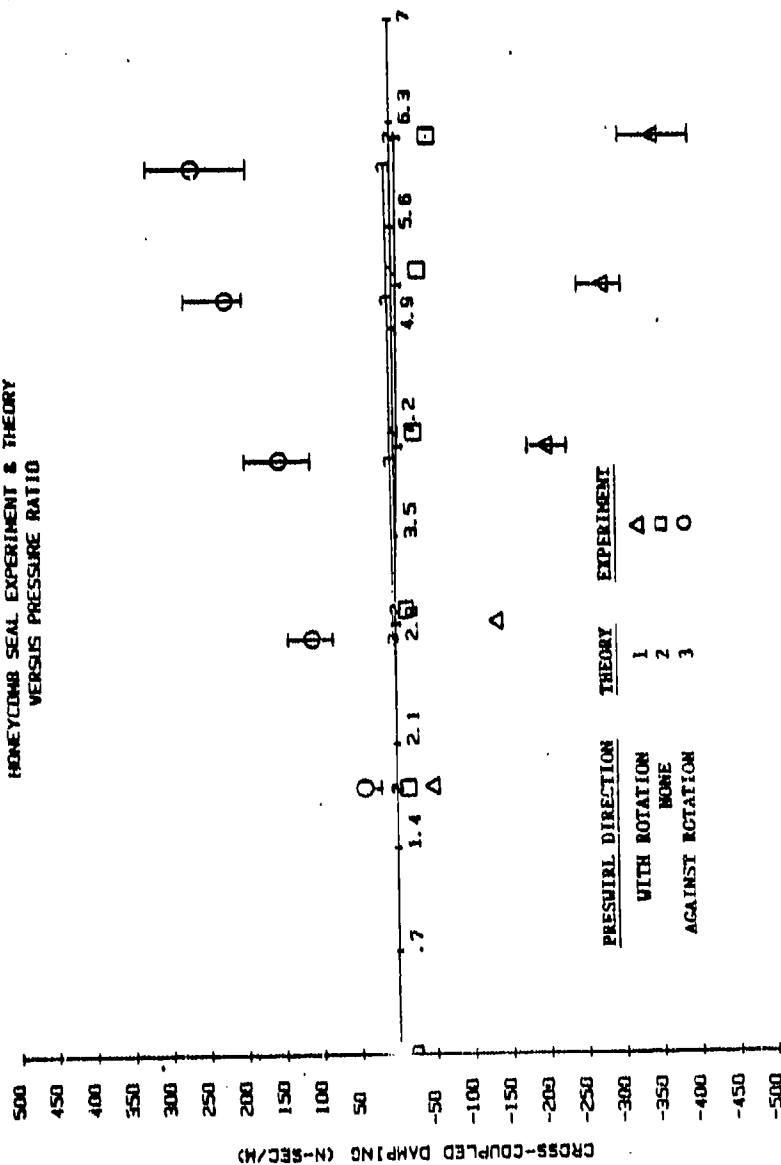


Fig. 43 Cross-coupled damping of honeycomb seal.

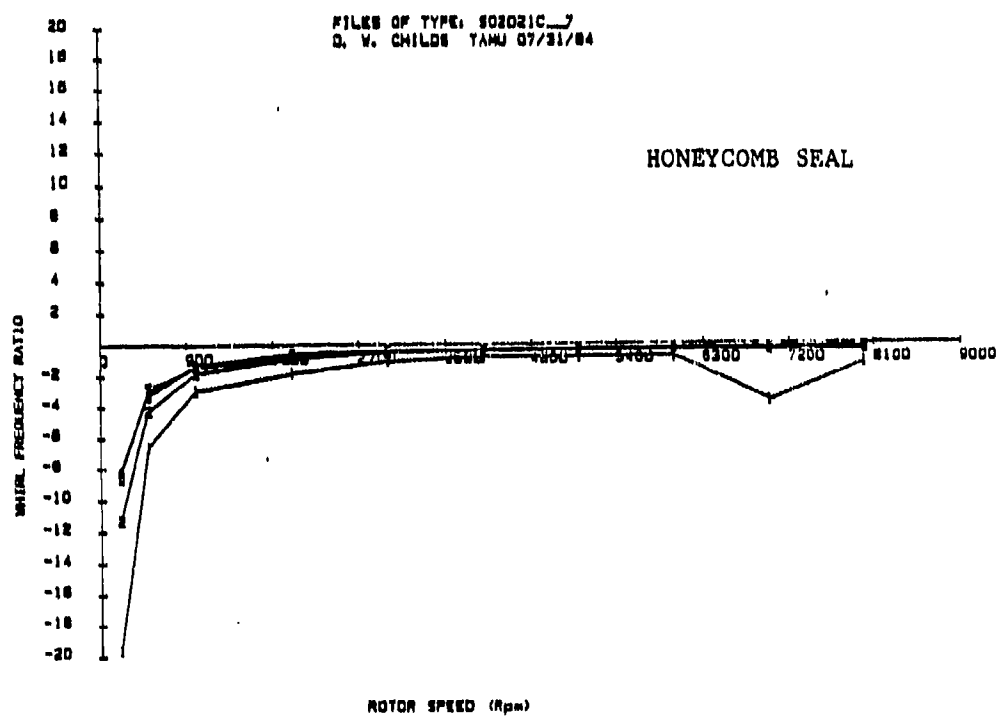
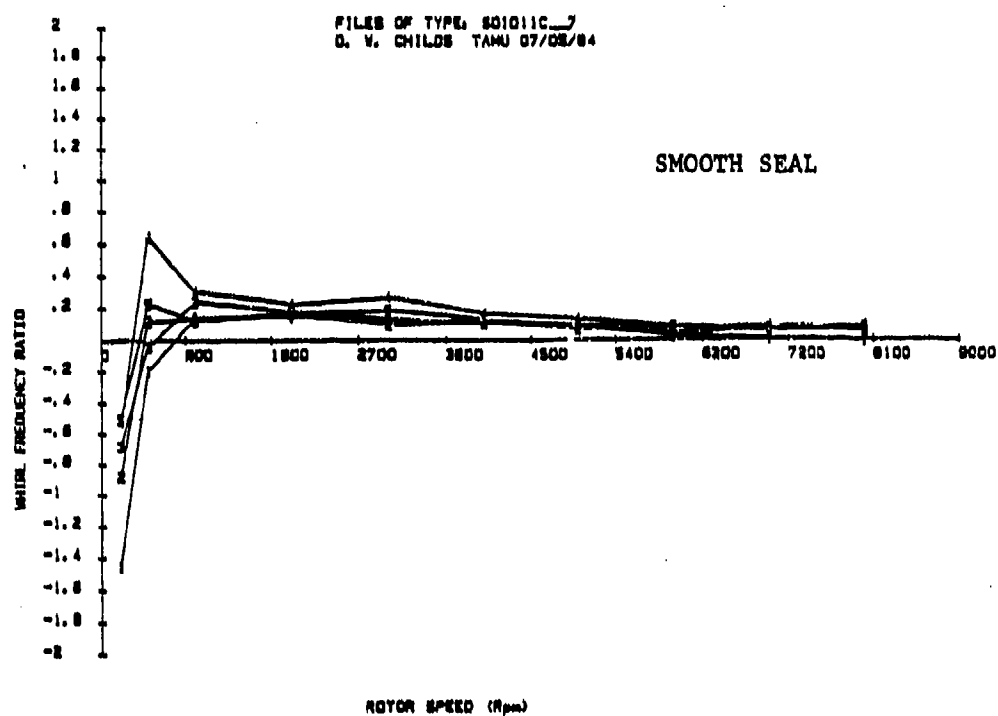


Fig. 44 Whirl frequency ratio for smooth and honeycomb seals.

negative cross-coupled stiffness. This negative k exerts a stabilizing influence, resulting in a force which acts in the same direction as the direct damping force.

CONCLUSIONS

A seal-test facility has been developed for the study of various types of gas seals. A method of determining rotordynamic coefficients has been established, and consistent, repeatable results have been obtained. After some initial failures in the test apparatus, reliability has been satisfactory, and a complete set of experimental results can be acquired in a matter of days.

The experimental and theoretical results of the preceding section support the following conclusions:

(a) Theoretical results for leakage are consistent with test results. Slightly higher leakage occurs for cases where the flow is not prerotated. Agreement between theory and experiment is satisfactory, with a maximum error of approximately 7.5%.

(b) Experimental and theoretical results for the pressure distributions and entrance-loss coefficients are relatively insensitive to running speed for the ranges (0-8500 rpm) and seals tested to date.

(c) The entrance-loss relationship (Deissler [13]) employed by Nelson is inconsistent with the test results for cases where the fluid is prerotated. For all such cases except one, the entrance-loss coefficient is underpredicted.

(d) In the test results for the honeycomb seal, the steep entrance pressure-loss seems to extend partially inside the seal. Also, the measured pressure at the exit of the seal generally equals the back pressure, rather than being greater, as is predicted by compressible flow theory for choked flow. These same phenomena do not occur for the smooth seal, implying that perhaps the effective length of the honeycomb

seal is less than its actual physical length.

(e) Test results for the direct stiffness of both the smooth and honeycomb seals show much greater sensitivity to fluid prerotation than predicted by theory. Prerotation of the fluid (in either direction) results in measured direct stiffnesses which are significantly larger than for no prerotation. Theory predicts the direct stiffness to be relatively insensitive to fluid prerotation.

(f) Theoretical predictions of the influence of fluid prerotation on cross-coupled stiffness and damping are consistent with the test results. In general, theory underpredicts the magnitudes of these cross-coupled coefficients, while correctly predicting their trends with respect to prerotation.

(g) Agreement between theory and test results for the direct damping coefficients is favorable. For both the smooth and honeycomb seal, direct damping is largest for no fluid prerotation.

(h) Over the speed range tested, none of the rotordynamic coefficients show appreciable sensitivity to the rotational speed of the rotor. This may be due to the lack of development of significant shear forces in the seal. It appears that running speeds above those attained to date may be necessary to produce significant shear force effects.

(i) For the non-prerotated case, the smooth seal has a positive cross-coupled stiffness, while k for the honeycomb seal is negative. This negative cross-coupled stiffness, and hence negative whirl ratio, indicates that the stability performance of the honeycomb seal is more favorable than that of the smooth seal.

REFERENCES

- 1 Black, H.F., and Jenssen, D.N., "Dynamic Hybrid Properties of Annular Pressure Seals," Proc. J. Mech. Engin., Vol. 184, pp. 92-100, 1970.
- 2 Jenssen, D.N., "Dynamics of Rotor Systems Embodying High-Pressure Ring Seals," Ph.D. dissertation, Herriot-Watt Univ., Edinburgh, Scotland, July 1970.
- 3 Black, H.F., and Jenssen, D.N., "Effects of High-Pressure Ring Seals on Pump Rotor Vibrations," ASME Paper No. 71-WA/FF-38, 1971.
- 4 Childs, D.W., "The Space Shuttle Main Engine High-Pressure Fuel Turbopump Rotordynamic Instability Problem," ASME Trans. J. of Engineering for Power, pp. 48-57, Jan. 1978.
- 5 Childs, D.W., and Moyer, D.S., "Vibration Characteristics of the HPOTP (High-Pressure Oxygen Turbopump) of the SSME ("Space Shuttle Main Engine)," ASME Paper No. 84-GT-31, 29th International Gas Turbine Conference and Exhibit, Amsterdam, 1984.
- 6 Black, H.F., Allaire, P.E., and Barrett, L.E., "The Effect of Inlet Flow Swirl on the Dynamic Coefficients of High-Pressure Annular Clearance Seals," Ninth International Conference in Fluid Sealing, BHRA Fluid Engineering, Leeuwarden, The Netherlands, Apr. 1981.
- 7 Childs, D.W., "Finite-Length Solutions for Rotordynamic Coefficients of Turbulent Annular Seals," ASME J. of Lubrication Technology, Vol. 105, pp. 437-444, July 1983.
- 8 Hirs, G.G., "A Bulk-Flow Theory for Turbulence in Lubricant Films," ASME Journal of Lubrication Technology, Vol. 95, pp. 137-146, April 1973.
- 9 Fleming, D.P., "Stiffness of Straight and Tapered Annular Gas Path Seals," ASME Journal of Lubrication Technology, Vol. 101, pp. 349-355, July 1979.
- 10 Fleming, D.P., "Damping in Ring Seals for Compressible Fluids," NASA CP 2133, Rotordynamic Instability Problems in High-Performance Turbomachinery, proceedings of a workshop held at Texas A&M University, 12-14 May 1980, pp. 169-188, 1980.
- 11 Nelson, C.C., "Rotordynamic Coefficients for Compressible Flow in Tapered Annular Seals," Mechanical Engineering Dept., Texas A&M University.
- 12 Nelson, C.C., "Analysis for Leakage and Rotordynamic Coefficients of Surface-Roughened Tapered Annular Gas Seals," ASME Paper No. 84-GT-32, 1984. Texas A&M University.

13 Deissler, R.G., "Analysis of Turbulent Heat Transfer and Flow in the Entrance Regions of Smooth Passages," NACA TN 3016, 1953.

14 Benckert, H., and Wachter, J., "Flow Induced Spring Coefficients of Labyrinth Seals for Application in Rotor Dynamics," NASA CP 2133, Rotordynamic Instability Problems in High-Performance Turbomachinery, proceedings of a workshop held at Texas A&M University, 12-14 May 1980.

15 Childs, D.W., and Dressman, J.B., "Testing of Turbulent Seals for Rotordynamic Coefficients," NASA CP 2250, Rotordynamic Instability Problems in High-Performance Turbomachinery, proceedings of a workshop held at Texas A&M University, 10-12 May 1982.

16 Chameih, D.S., Acosta, A.J., Brennen, C.E., Caughey, T.K., and Franz, R., "Experimental Measurement of Hydrodynamic Stiffness Matrices for a Centrifugal Pump Impeller," NASA CP 2250, Rotordynamic Instability Problems in High-Performance Turbomachinery, proceedings of a workshop held at Texas A&M University, 10-12 May 1982.

17 Shoji, H., and Ohashi, H., "Lateral Fluid Forces Acting on a Whirling Centrifugal Impeller in Vaneless and Vaned Diffuser," presented at the Third Workshop on Rotordynamic Instability Problems in High-Performance Turbomachinery, 28-30 May 1984.

18 Adams, M.L., and Makay, E., "Measurement of Interstage Fluid-Annulus Dynamical Properties," NASA CP 2250, Rotordynamic Instability Problems in High-Performance Turbomachinery, proceedings of a workshop held at Texas A&M University, 10-12 May 1982.

19 Iino, T., and Kaneko, H., "Hydraulic Forces Caused by Annular Pressure Seals in Centrifugal Pumps," NASA CP 2133, Rotordynamic Instability Problems in High-Performance Turbomachinery, proceedings of a workshop held at Texas A&M University, 12-14 May 1980.

20 Bowen, W.L., and Bhateje, R., "The Hollow Roller Bearing," ASME Paper No. 79-Lub-15, ASME-ASLE Lubrication Conference; Dayton, Ohio, 16-18 October 1979.

21 Cohen, H., Rogers, G.F.C., and Saravanamuttu, H.I.H., Gas Turbine Theory, Longman Group Limited, 1972.

22 White, F.M., Fluid Mechanics, McGraw-Hill, 1979.

VITA

Name: Colby Oran Nicks

Permanent Address: 4501 Elm Branch Drive
Arlington, Texas 76017

Birthdate: 1/10/60

Higher Education: B.S., Mechanical Engineering, 1983,
Virginia Polytechnic Institute and State University

ON THE PREDICTION OF INCOMPRESSIBLE FLOW IN LABYRINTH SEALS *

D.L. Rhode, J.A. Damko, U.K. Traegner, and S.R. Sobolik
Mechanical Engineering Department
Texas A&M University
College Station, TX

ABSTRACT

A new version of a swirl-flow finite difference computer program was developed incorporating the recent quadratic, upwind-weighted differencing scheme. It was employed in predicting the incompressible flow within each of two simple labyrinth seal cavity configurations. Close agreement between predictions and previous corresponding seal measurements is shown for verification purposes. The distribution of each quantity revealing the complete flow character for a labyrinth seal cavity is presented and discussed here for the first time. The effect of seal cavity geometry on overall pressure drop is shown to be significant.

In addition, this investigation constitutes a timely evaluation of the QUICK convective differencing scheme for realistic, highly non-linear turbulent flow applications. No significant stability difficulties were encountered. Moreover, the resulting increased accuracy allows an accurate solution using considerably fewer grid points than for the Hybrid upwind/central scheme. Computer execution time consumed employing QUICK was only 44% of that for the Hybrid scheme.

NOMENCLATURE

A	- Control volume face area
c	- Tooth clearance
d	- Radial distance from cavity base to stator wall
k	- Turbulence kinetic energy
L	- Axial length of seal cavity
Pe	- Grid Peclet number
Q	- Leakage volumetric flow rate
R	- Stator wall radius
r _{sh}	- Shaft radius
Re _x	- Axial Reynolds number
S _p , S _u	- Components of linearised source term
S _q	- Source term of ϕ -equation
Ta	- Taylor number
U	- Tooth-clearance bulk axial velocity
V = (u, v, w)	- Time-mean velocity (in x, r, θ direction)

W	- Bulk swirl velocity
x, r, θ	- Axial, radial, azimuthal cylindrical polar coordinates
Γ	- Turbulent exchange coefficient
Δ	- Internodal mesh spacing
ϵ	- Turbulence dissipation rate
ϕ	- Generalized dependent variable
ρ	- Time-mean density
ν	- Kinematic viscosity
Ω	- Shaft speed

Subscripts

n.s.e.w	North, south, east, west faces of a control volume
N,S,E,W	North, South, East, West neighboring grid points

INTRODUCTION

Background

Labyrinth seals play a vital role in gas and steam turbines, compressors, and high-capacity fuel pumps. In fuel pumps the sealing objective is generally to minimize the leakage flow around the impellers, whereas for turbines it is often to maintain a minimal leakage flow for cooling hot parts. The basic idea in the design of a labyrinth seal is to provide a highly dissipative flow path between high and low pressure regions. This is accomplished by means of a series of restrictor teeth and dissipation cavities. The flow passage through a labyrinth is illustrated in Fig. 1 for a simple straight-through seal configuration. Each tooth converts a portion of the available pressure head into mean flow kinetic energy, some of which is dissipated within the cavity immediately downstream.

Numerous investigators have experimentally studied several gross overall flow characteristics of labyrinth seals in attempting to obtain empirically-based relations for estimating the leakage rate. A few have employed incompressible fluids [1-4] while others have

* Presented at the 7th Annual Energy-Sources Technology Conference (ASME, et al.), New Orleans, La, Feb. 12-16, 1984.

utilized compressible ones [5-10], often at incompressible flow conditions. The majority of these investigations have performed parametric studies concerning how pressure drop, seal design, clearances, rotational speed, etc. affect overall performance. The results of such studies can be used with a fair amount of accuracy for predicting the leakage rate through the particular labyrinth seal that was studied. However, when a labyrinth seal of a considerably different design is considered, use of these empirically-based relations entails substantial error.

Accurate numerical simulation of labyrinth seal flowfields employing the governing differential equations is relatively complicated and expensive. A recent computerized literature search conducted by the present authors indicated that only Stoff [11] and Rhode et al. [12] have reported such an investigation. Stoff's solution corresponded to a very large scale experimental water facility consisting of a straight-through series of generic cavities as illustrated in Fig. 1. He compared a single radial profile of predicted mean swirl velocity, r.m.s. swirl velocity and turbulence dissipation rate with his corresponding measurements for an axial station midway between adjacent teeth. A sample of these measurements was utilized in this investigation for experimental verification purposes (these are apparently the only detailed measurements available). Rhode et al. presented several solutions, involving different grids and convection differencing schemes, clearly illustrating false diffusion numerical error effects on the solution for compressible flow through a cavity of unique configuration.

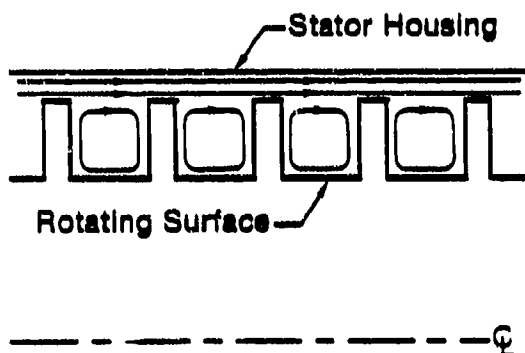


Fig. 1 Generic labyrinth seal configuration

False Diffusion

Until recently the most effective method for avoiding instability in numerical solutions of convection-dominated flows has been the use of upwind differencing for convection terms. However, this first-order accurate scheme introduces false diffusion [13]. This is a second-order truncation numerical error which can, under certain conditions, yield serious consequences for solution accuracy. This difficulty occurs where convection dominates (i.e. where the grid Péclet number $|Pe| = |V|\Delta/r_\phi$ exceeds 2.0) in the presence of both streamline-to-grid skewness and diffusive transport normal to the flow direction.

False diffusion results in an overly diffusive solution. In fact, some solutions have been obtained in which false diffusion has entirely obscured phys-

ical diffusion [14-15]. It is the turbulent recirculating type of flow, such as that of the present problem, which is particularly susceptible to this phenomenon. Grid refinement sufficient to allow central differencing (i.e. when $|Pe| \leq 2.0$) for convection terms would circumvent this error. However, cost and storage difficulties would become severe for most two-dimensional problems and prohibitive for three-dimensional ones.

Fortunately, two improved convective differencing approaches which minimize false diffusion have recently been proposed. The "skew upwind differencing" scheme of Raithby [16] reduces skewness errors by essentially aligning the upwind differencing scheme for convection terms along local streamlines. The recent QUICK (Quadratic Upstream Interpolation for Convective Kinematics) scheme of Leonard [17] eliminates false diffusion by incorporating a three-point upwind-shifted interpolation formula. Recent investigations by Leschiner [18] and Leschiner and Rodi [19] discuss results using both QUICK and skew-upwind differencing, indicating distinct advantages over the hybrid upwind/central differencing scheme.

Although several application studies [18-24] have incorporated one or both of these two recent schemes, most of the flow problems considered thus far are relatively easy to solve. Hence the stability and overshoot tendencies of these two schemes remain to be sufficiently challenged. Specifically, to the knowledge of these authors, only Leschiner and Rodi [19] and Han et al. [22] have formally documented predictions using QUICK for highly non-linear, turbulent recirculating flows. Similarly only Militsar et al. [24], Leschiner and Rodi [19], and Banodakar et al. [23] have reported using Raithby's method for such cases. The present problem is perhaps the most challenging for stability considerations because of the very high Re and the enhanced pressure-velocity non-linearity due to the presence of swirl momentum.

NUMERICAL PROCEDURE

General Remarks

The numerical procedure employed in this investigation is based on that of the TEACH-2E computer program of Gosman and Pun [25]. The recent QUICK convective differencing scheme of Leonard, which is described below, was implemented as a new version of the code. Other features include swirl momentum and its influence on wall functions as well as the simulation of sloping wall boundaries. There are several methods of numerically simulating the sloping cavity wall shown in Fig. 5(b). In the interest of conceptual simplicity, the stairstep simulation approach illustrated in Fig. 2 was followed. Rhode et al. [26] found that, if carefully implemented, the error arising from this approximation is small in comparison to that of the turbulence model.

The governing equations for this axisymmetric flow consist of conservation of mass and momentum (with x, r, θ velocity components u, v, w), as well as transport equations for turbulence kinetic energy k and turbulence dissipation rate ϵ . They may be expressed in the general form

$$\frac{1}{r} \left[\frac{\partial}{\partial x} (r u \phi) + \frac{\partial}{\partial r} (r v \phi) - \frac{\partial}{\partial x} (r \Gamma_\phi \frac{\partial \phi}{\partial x}) - \frac{\partial}{\partial r} (r \Gamma_\phi \frac{\partial \phi}{\partial r}) \right] = S_\phi \quad (1)$$

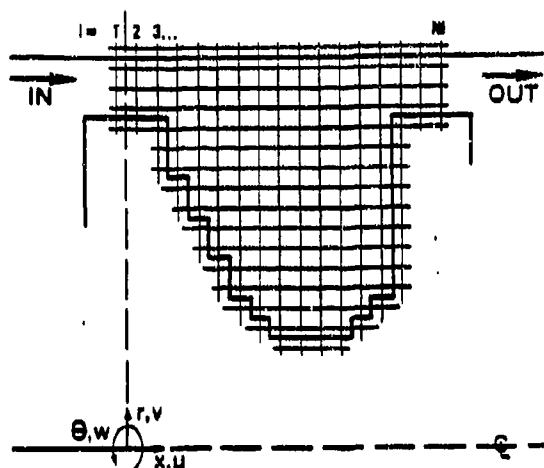


Fig. 2 Computational domain for a labyrinth seal cavity with a coarse grid

where ϕ represents any of the dependent variables, and the equations differ primarily in their final source terms S_ϕ [27]. It is the standard version of the two-equation $k-\epsilon$ turbulence model [28], extended to include swirl momentum, which has been employed thus far. The corresponding finite difference equations are solved via the SIMPLX semi-implicit, line-by-line method employing the tridiagonal matrix algorithm. The solution method advances, processing one column of control volumes at a time, always sweeping in the downstream direction.

Boundary values at the cavity inlet are naturally very important, but unfortunately were unknown, as necessary quantitative flow measurements were unavailable even at a single operating condition. Due to this lack of inlet boundary data, for each numerical iteration the inlet values of each variable (except pressure) were assumed equal to the latest corresponding outlet values. This practice implies the presence of a series of geometrically identical cavities and a streamwise periodic flow occurring downstream of the first two or three cavities. The boundary treatment utilized along each wall employed the wall function formulae for swirling flows [27]. A special technique of implementing these formulae was utilized for control volumes along the rotor in order to properly account for the circumferential velocity of the surface.

Discretization Using QUICK

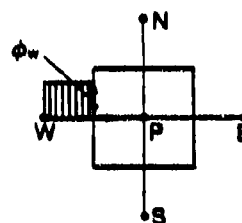
The computer code originally embodied the Hybrid upwind/central differencing scheme for convection terms. This formulation yields the upwind difference treatment when the grid Péclet number magnitude in a given direction exceeds 2.0; otherwise central differencing is used. The false diffusion difficulty with the first-order accurate upwind portion of the Hybrid scheme motivated the use of QUICK. The QUICK scheme yields a third-order accurate difference equation which is free of false diffusion, a second order truncation error. Raithby's skew upwind differencing scheme would have probably dispensed with false diffusion just as effectively.

Following the approach of Gosman and Pun, the finite difference equation for each ϕ can be obtained by first analytically integrating Eq. 1 over the volume of the appropriate micro-control volume using the Gauss Divergence theorem. The result may be expressed in terms of the control volume face values. The convection and diffusion terms become surface integrals of the convective and diffusive fluxes while the source term is linearized. This results in [25]

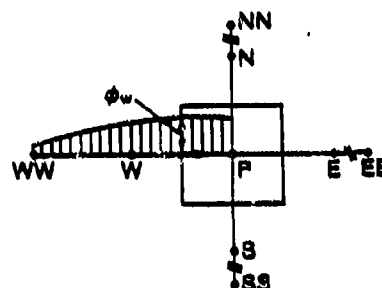
$$\begin{aligned} & [\rho u \phi - \Gamma_\phi \frac{\partial \phi}{\partial x}]_e A_e - [\rho u \phi - \Gamma_\phi \frac{\partial \phi}{\partial x}]_w A_w \\ & + [\rho v \phi - \Gamma_\phi \frac{\partial \phi}{\partial r}]_n A_n - [\rho v \phi - \Gamma_\phi \frac{\partial \phi}{\partial r}]_s A_s \\ & = [S_p \phi_p + S_u] Vol \end{aligned}$$

where subscripts n, s, e and w refer to north, south, east and west control volume faces. There are various ways of evaluating the face values of ϕ in the convection terms using latest available values at neighboring nodes. Each method of evaluation constitutes a distinct convection differencing scheme. The objective of any method is to accurately evaluate the convected ϕ -value at each face of the control volume while avoiding the instability associated with high convection rates.

Observe from the illustration in Fig. 3 that the upwind scheme is based on the uniform ϕ -distribution



(a) Upwind differencing concept



(b) QUICK differencing concept

Fig. 3 Illustration of (a) Upwind and (b) QUICK differencing concepts for evaluating ϕ at a west control volume face with flow from left to right

assumption in evaluating ϕ at any face. Also shown is that QUICK is based on upstream-shifted quadratic interpolation for each control volume face. The west face QUICK interpolation expressions using a uniform grid for simplicity are

$$\phi_w = \frac{1}{2}(\phi_p + \phi_W) - \frac{1}{6}(\phi_p - 2\phi_W + \phi_{WW})$$

if u_w is positive and

$$\phi_w = \frac{1}{2}(\phi_p + \phi_W) - \frac{1}{6}(\phi_p - 2\phi_p + \phi_W)$$

if u_w is negative. The first term in these expressions represents the centered difference formula, and the second is the crucial stabilizing upstream-weighted curvature contribution. Quadratic interpolation was incorporated only for the convected variable ϕ whereas centered differencing was applied for the convecting velocities.

This scheme has been carefully implemented in the convective terms of only the momentum equations. Leschiner and Rodi [19] have supported this in explaining that solutions for k and ϵ were found to be unaffected by the convective differencing scheme, especially in the shear layer bordering a recirculation zone. They attribute this to the fact that the source terms of these equations dominate convective transport within the influential shear layer such as that found in the present seal problem.

RESULTS AND DISCUSSION

Experimental Verification

A computerized literature search indicated that only the paper by Stoff [11] gives detailed quantitative velocity measurements within a labyrinth seal cavity. Only the circumferential velocity component is presented; it was measured with a laser doppler anemometer at a single axial station, located midway between adjacent teeth. These measurements were employed for preliminary verification testing of the current computer code.

Stoff utilized a large-scale test section model of a straight-through seal with rectangular cavities through which water flowed. It is assumed that the flow conditions are characterized primarily by the axial Reynolds number $Re_x = 2Uc/\nu \approx 3.4 \times 10^2$ and the Taylor number $Ta = (Wd/\nu)(d/r_{sh})^4 \approx 1.1 \times 10^4$. These are based on: tooth-clearance bulk axial velocity U , tooth clearance c , kinematic viscosity ν , cavity bulk swirl velocity W , shaft radius r_{sh} , and radial distance from cavity base to stator wall d .

Figure 4 shows that predictions using the computer code described above are in good agreement (6% discrepancy) with Stoff's corresponding measurements. Further, Stoff's computation employed the same numerical approach and Hybrid differencing scheme discussed earlier, and his predictions are essentially identical to those shown here.

Operating Conditions

The operating conditions of the two seals investigated herein are identical. Liquid hydrogen at 42°K enters a cavity with tooth-clearance bulk velocity $U = 338$ m/s. The primary dimensionless flow parameters (defined earlier) are: $Re_x = 1.0 \times 10^3$ and $Ta = 1.2 \times 10^5$. Other conditions are: shaft speed $\Omega = 35,410$ rpm, cavity axial length $L = 1.113$ mm, stator wall radius $R = 42.89$ mm, tooth radial

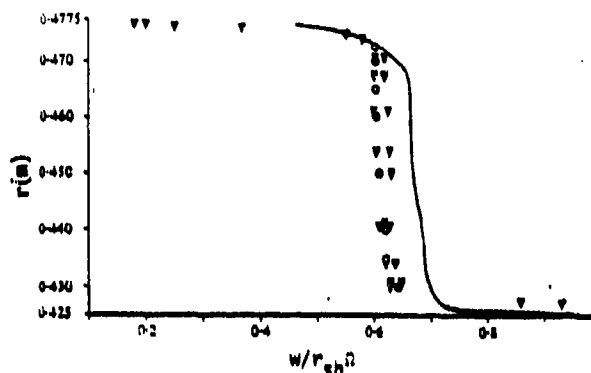


Fig. 4 Comparison of present predictions (—) of dimensionless swirl velocity with corresponding LDA measurements (o o o, $\nabla \nabla \nabla$) of Stoff [11] at $x/L = 0.5$

clearance $c = 0.216$ mm, radial distance from cavity base to stator wall $d = 1.105$ mm, and kinematic viscosity $\nu = 1.462 \times 10^{-7}$ m²/s.

A grid dependence study was conducted and is discussed in detail below. Convergence tests using convergence criteria as low as 0.05% were undertaken for the normalized sum of residual mass source magnitudes, for example.

Streamline Plots

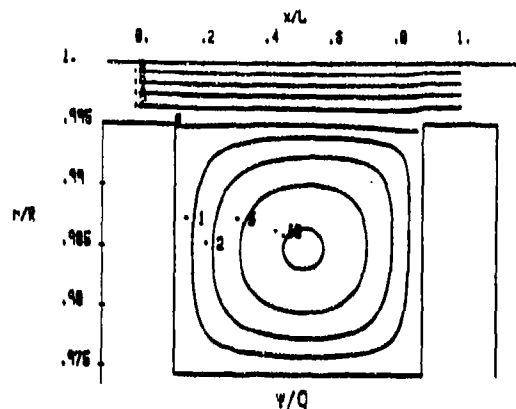
Figures 5(a) and (b) show predicted dimensionless streamline patterns calculated and plotted by computer. The recirculation cell given in Fig. 5(a) is the expected result of a free shear layer flowing over a cavity. The predictions give no indication that an additional small recirculation cell exists in the corner at the base of each tooth. For the case of negligible inlet (i.e. leakage) flow rate, a pair of counter-rotating Taylor-like cells are expected within the cavity. A predicted velocity vector plot of this flowfield is presented by Stoff. He also shows a similar plot for the case of small inlet flow rate $U/W = 0.06$. That case exhibits both recirculation cells, the upstream one being extended downstream near the free shear layer, and the other occupying only the lower right-hand corner of the rectangular cavity.

Also observe in Fig. 5(a) that the dividing streamline exhibits a reattachment stagnation point slightly below the peripheral corner of the downstream tooth. This is also true of the typical cavity design as seen in Fig. 5(b). The predicted recirculation strength for the typical design is approximately 29% of the leakage flow rate, whereas it is 39% for the generic case.

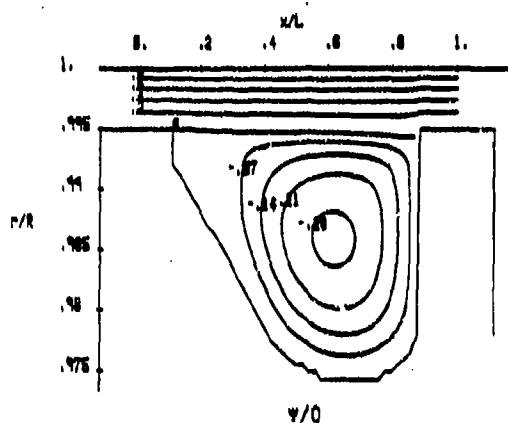
Profile Plots

Many quantitative details for the flow field in a labyrinth cavity are not found elsewhere, particularly concerning the inlet boundary values. Therefore numerous radial profiles of each flow variable are included here. For velocity predictions, three separate solutions are shown, employing: (a) the QUICK formulation with a 33×31 grid, (b) the Hybrid formulation with a 53×53 grid, and (c) the Hybrid formulation with the 33×31 grid. Both grids are uniform for comparison purposes.

All the data presented here was calculated and plotted by computer. Figures 6, 8, and 9 exhibit the distribution of predicted axial, radial, and swirl



(a) Generic cavity



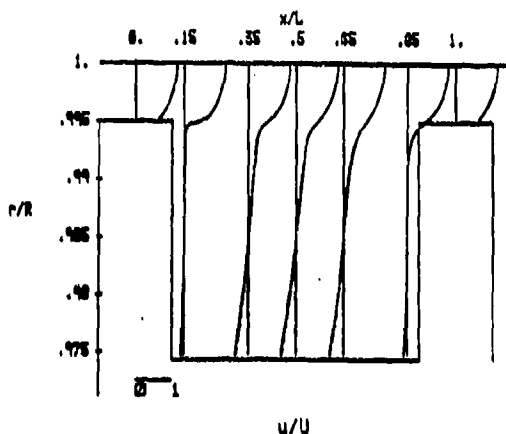
(b) Typical cavity

Fig. 5 Predicted dimensionless streamline pattern for: (a) a generic and (b) a typical labyrinth seal cavity

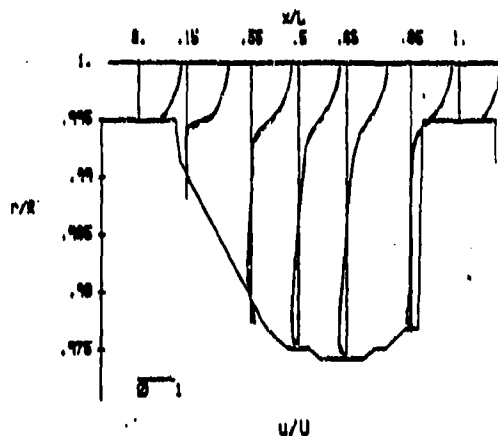
velocity values, whereas Fig. 7 provides a magnified view of a portion of Fig. 6 for detailed inspection. Figure 6(a) shows the dimensionless mean axial velocity distribution for the generic cavity. The axial velocity values of the three solutions given are in agreement. These solutions indicate that a very large value of $\partial u / \partial r$ occurs near the separation corner; this is indicative of high turbulence energy generation in the free shear layer.

The magnified view (with expanded velocity scale) of Fig. 7(a) reveals that, indeed, the 33 x 31 QUICK and 53 x 53 Hybrid solutions are essentially identical. This indicates that both solutions are accurate and that the QUICK formulation has been correctly implemented. The 33 x 31 Hybrid and 53 x 53 Hybrid solutions differ very slightly.

The axial velocity distribution for the typical cavity in Fig. 6(b) is very similar to that in Fig. 6(a). The most significant differences appear at $x/L = 0.35$, both in the free shear layer and in the lower extremity of the cavity. As with the generic cavity, the magnified view in Fig. 7(b) clearly shows



(a) Generic cavity

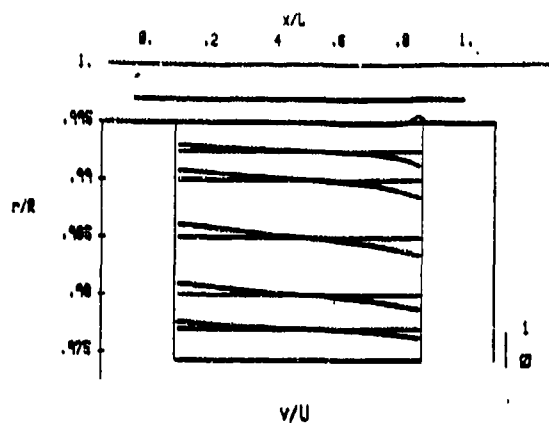


(b) Typical cavity

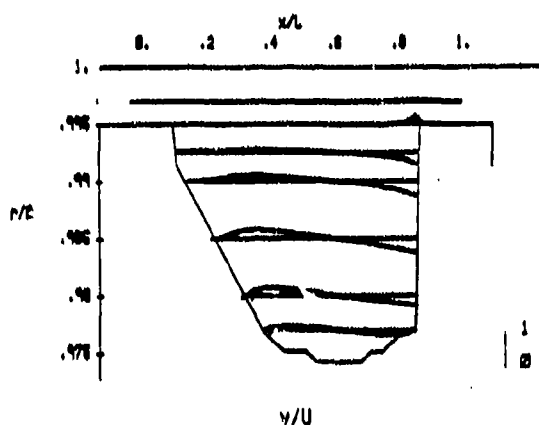
Fig. 6 Predicted dimensionless mean axial velocity for (a) a generic and (b) a typical labyrinth seal cavity showing 33 x 31 QUICK (—), 53 x 53 Hybrid (—), and 33 x 31 Hybrid (—) solutions

that the 33 x 31 QUICK and the 53 x 53 Hybrid solutions of axial velocity are nearly identical. Note that in this case the 33 x 31 Hybrid solution is not grid independent in the free shear layer. The axial velocity values of this solution deviate from those of the other two solutions by as much as 20% of U .

Observe at this point that the QUICK approach - as implemented here - exhibits a major economical advantage over the Hybrid approach. In obtaining a grid independent solution, utilization of the Hybrid method requires 53 x 53 grid points (consuming 1.79×10^4 CPU seconds on a Prime 750 computer), whereas utilization of QUICK requires only 33 x 31 points (using only 7.79×10^3 CPU seconds). This execution



(a) Generic cavity

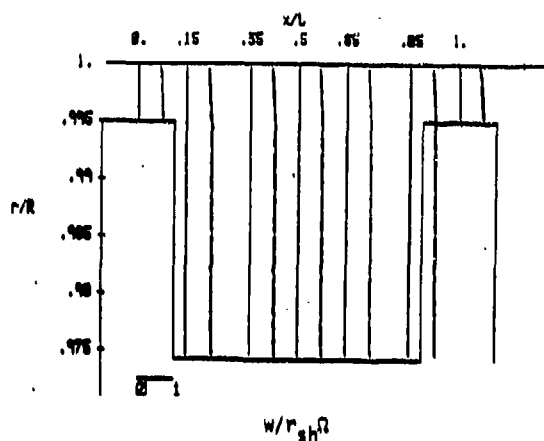


(b) Typical cavity

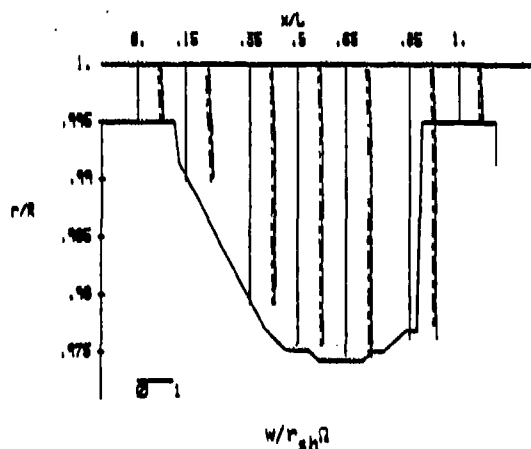
Fig. 8 Predicted dimensionless mean radial velocity for: (a) a generic and (b) a typical labyrinth seal cavity showing 33 x 31 QUICK (—), 33 x 33 Hybrid (---) and 33 x 31 Hybrid (- - -) solutions

decrease at constrictions in flow area. The variation of flow area is indicated by the dividing streamline in Figure 5(a). A sharp positive pressure peak, which occurs in an annular fashion near $x/L = 0.85$, results from the flow stagnation on the downstream tooth. The resulting overall pressure drop from inlet to outlet of this cavity at the staged conditions is predicted as approximately 6.0×10^2 kPa. Only the 33 x 31 QUICK solution is presented here, as values from the other two solutions show insignificant deviations.

The pressure distribution within the typical cavity is seen in Fig. 10(b) to exhibit similar trends. However, leakage flow pressure varies in the streamwise direction much more gradually for this geometry until about $x/L = 0.65$. Preceding downstream, pressure decreases more rapidly than for the generic case as the flow area constricts in passing



(a) Generic cavity

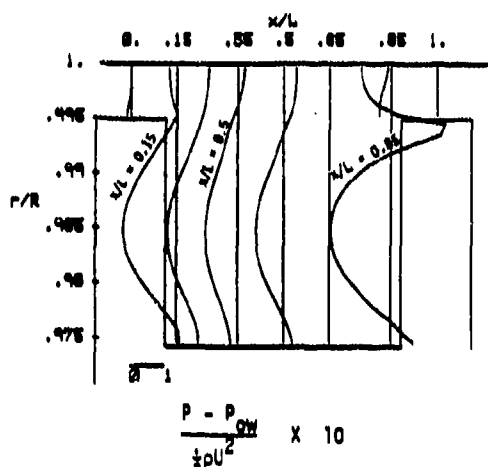


(b) Typical cavity

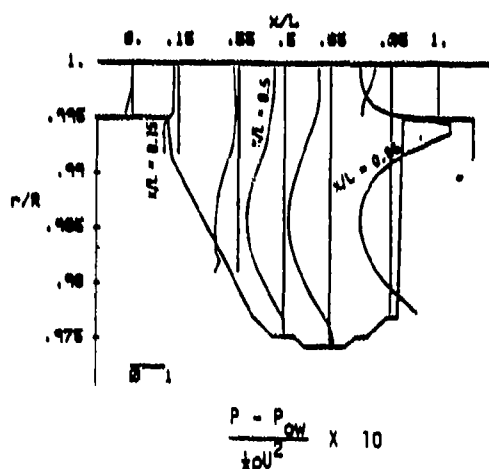
Fig. 9 Predicted dimensionless mean swirl velocity for: (a) a generic and (b) a typical labyrinth seal cavity showing 33 x 31 QUICK (—), 33 x 33 Hybrid (---) and 33 x 31 Hybrid (- - -) solutions

over the downstream tooth. The predicted bulk pressure drop for this cavity is approximately 8.0×10^2 kPa, an increase of 33% from the generic geometry. Hence, apart from rotordynamic stability considerations, the typical design is therefore preferred over its generic counterpart.

As mentioned earlier, the large value of $\partial u / \partial r$ in the free shear layer yields a high generation rate of



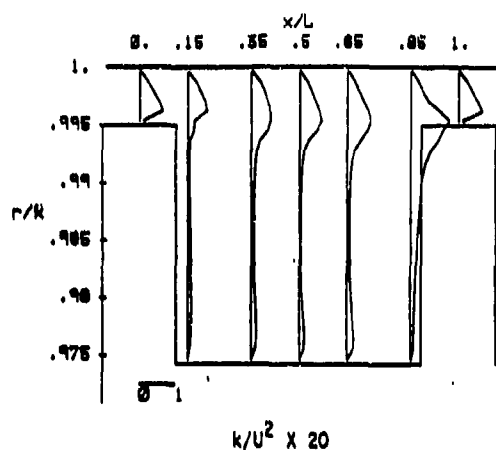
(a) Generic cavity



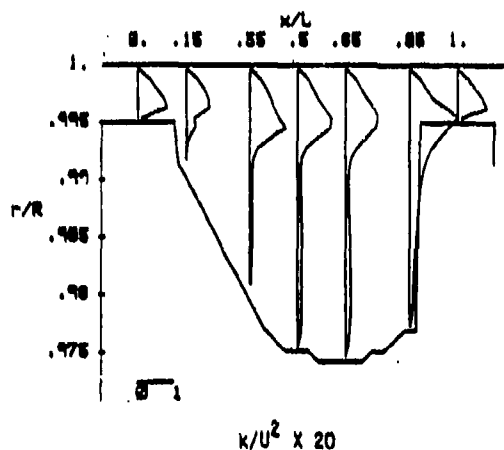
(b) Typical cavity

Fig. 10 Predicted dimensionless mean relative pressure for: (a) a generic and (b) a typical labyrinth seal cavity showing the 33 x 31 QUICK solution

turbulence kinetic energy. This of course promotes the large overall pressure drop. Hence, the station maximum of turbulence energy occurs near the free shear region as seen in Figs. 11(a) and (b). Note that the typical cavity geometry exhibits a significantly higher level of turbulence energy than for the



(a) Generic cavity



(b) Typical cavity

Fig. 11 Predicted dimensionless turbulence kinetic energy for: (a) a generic and (b) a typical labyrinth seal cavity showing the 33 x 31 QUICK solution

generic case. The greatest value occurs in both cases near the reattachment stagnation point. A significant portion of this turbulence energy is converted over the downstream tooth as indicated by the distribution at $x/L = 1.0$. As expected for both cavities considered here, the recirculation region is seen to be an effective turbulence energy sink.

CONCLUDING REMARKS

The complete distribution of each quantity revealing the flow character within a realistic laby-

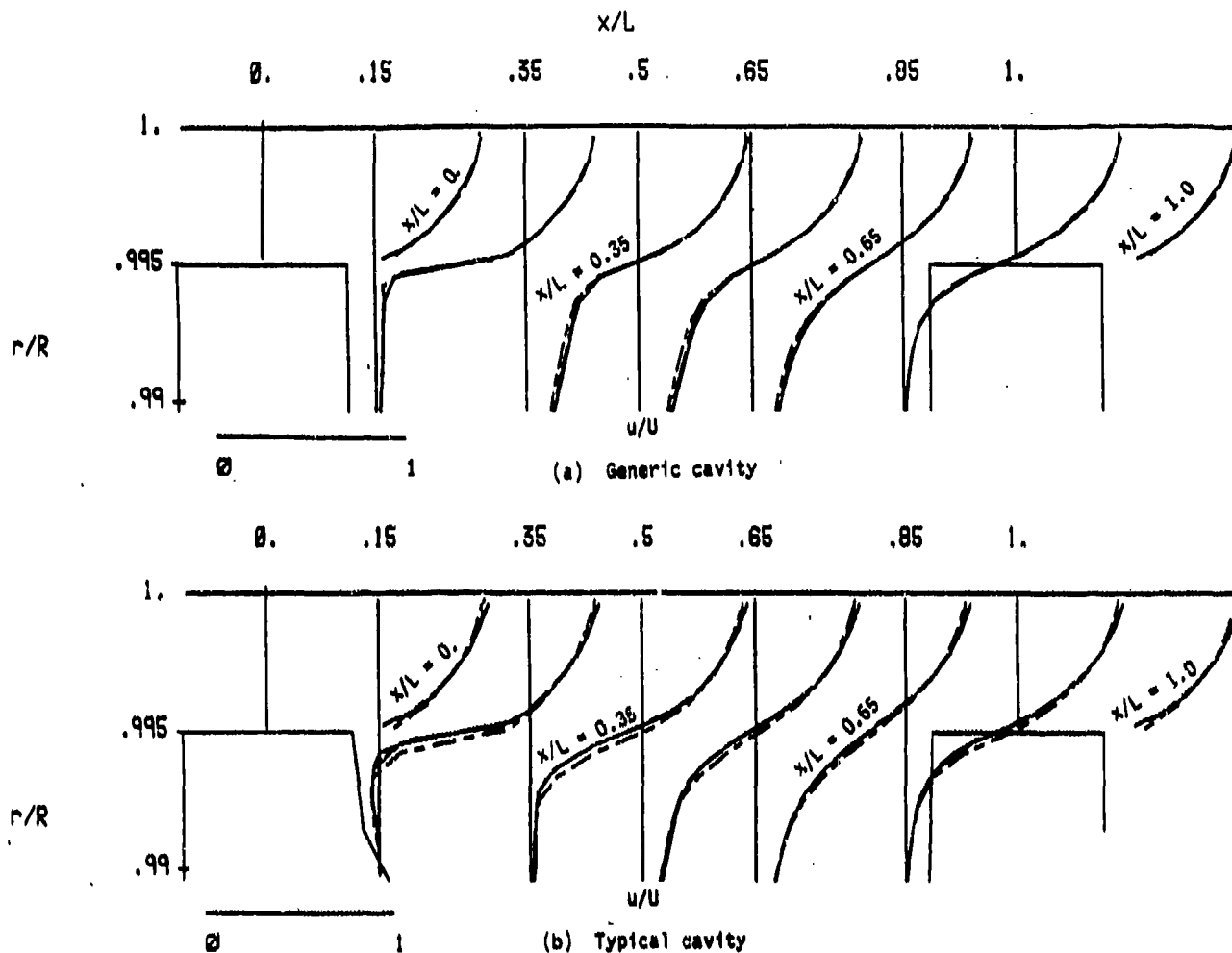


Fig. 7 Magnified view of predicted dimensionless mean axial velocity for (a) a generic and (b) a typical labyrinth seal cavity showing 33 x 31 QUICK (—), 33 x 31 Hybrid (---) and 33 x 31 Hybrid (— · —) solutions

time for the present QUICK version of the code is only 44% of that required by the Hybrid version. This is mostly attributed to the well known apparent sluggish response to grid refinement of the upwind portion of the Hybrid scheme. As demonstrated by Han et al. [22], this lack of response is actually a false diffusion effect.

As expected, there is negligible mean radial velocity in the leakage flow region of the generic cavity as seen in Figs. 8(a) and (b) except near the stagnation point on the downstream tooth. Seal designers can perhaps reduce this leakage contribution by altering the tooth shape at this location. Essentially the same values result from the three solutions. The swirl velocity in Figs. 9(a) and (b) is normalized by the shaft circumferential velocity. The values

for both seal designs are almost uniform throughout the entire domain. They are 0.65 and 0.69 for Figs. 9(a) and (b) respectively. Not shown is a very sharp gradient near each surface. All three solutions give essentially the same swirl velocity values for the generic design while the 33 x 31 Hybrid solution is not quite grid independent for the typical case.

Figures 10(a) and (b) show the distribution of pressure relative to the cavity inlet stator wall pressure P_{0w} . In the leakage flow region of the generic cavity, pressure decreases in the streamwise direction until about $x/L = 0.5$. Then it increases slightly until approximately $x/L = 0.75$, whereupon it suddenly decreases as the flow accelerates over the downstream tooth. This pressure variation is a reflection of the Bernoulli effect of pressure

rinth seal cavity is documented here for the first time. This serves to provide seal designers with new insight regarding important flowfield details. These results further allow one to advance the development of simple empirically-based algebraic design models in current use. One result of particular interest in this regard is that, for similar cavities, the dimensionless swirl velocity may be accurately approximated by a uniformly-distributed value of 0.69. Another important finding is the shape of the dividing streamline and how it influences leakage flow pressure variation.

The numerical aspect of this investigation constitutes a timely and stringent test of the inherent stability of QUICK for a realistic application. The flows considered here are highly nonlinear, as the presence of swirl momentum is known [26] to increase the pressure-velocity coupling considerably. As implemented here, QUICK contributed no noticeable stability difficulty for each of several such highly nonlinear turbulent flow problems. Moreover, for a given level of accuracy, this version of the code consumed only 44% of the execution time required by the Hybrid version.

ACKNOWLEDGMENT

These results were obtained as a by-product of a fundamental study for which the financial support of AFOSR is gratefully acknowledged.

REFERENCES

- Jaria, J., "Flow Through Straight-Through Labyrinth Seals," Proceedings of the Seventh International Congress of Applied Mechanics, 1948, Vol. 2, pp. 70-82.
- Han, J.T., "A Fluid Mechanics Model to Estimate the Leakage of Incompressible Fluids Through Labyrinth Seals," ASME Paper No. 79-FE-4, 1979.
- Isaacson, J., "Pump Impeller Labyrinth Seal Study," DDR-712-3012, Dec. 4, 1957.
- Yamada, Y., "On the Pressure Loss of Flow Between Rotating Co-Axial Cylinders with Rectangular Grooves," Bulletin of the JSME, Vol. 5, No. 20, 1962, pp. 642-651.
- Martin, H., "Labyrinth Packings," Engineering, Vol. 85, Jan. 10, 1908, pp. 35-38.
- Stodola, A., Steam and Gas Turbines, 6th ed., McGraw-Hill, Vol. 1, 1927, pp. 189-194.
- Gercke, M., "Flow Through Labyrinth Packing," Mechanical Engineer, Vol. 36, 1934, pp. 678-680.
- Egli, A., "The Leakage of Steam Through Labyrinth Seals," Transactions of the ASME, Vol. 57, 1935, pp. 115-122.
- Kearton, W., and Kah, T., "Leakage of Air Through Labyrinth Glands of Staggered Type," Proceedings of the Institute of Mechanical Engineers, Vol. 166, 1952, pp. 180-194.
- Stockar, H.L., "Advanced Labyrinth Seal Design Performance for High Pressure Ratio Gas Turbines," ASME Paper No. 75-WA/GT-22, 1975.
- Stoff, H., "Incompressible Flow in a Labyrinth Seal," JL. Fluid Mech., Vol. 100, 1980, pp. 817-829.
- Rhode, D.L., Sobolik, S.R. and Traegner, U.K., "Prediction of Compressible Flow in Labyrinth Seals," 36th annual meeting of the American Physical Society, Nov. 20-22, 1983, Houston, TX.
- Roache, P.J., Computational Fluid Dynamics, Hermosa, Albuquerque, NM, 1976.
- De Vahl Davis, G. and Mallinson, G.D., "An Evaluation of Upwind and Central Difference Approximations by a Study of Recirculating Flow," Computers and Fluids, Vol. 4, 1967, p. 29.
- Leschziner, M.A., "On the Problem of Numerical Diffusion in First-Order Finite Difference Schemes Applied to Free Recirculating Flows," Proceedings of the 2nd GAMM Conference on Numerical Methods in Fluid Mech., Cologne, Fed. Rep. of Germany, 1977.
- Raithby, G.D., "Skew Upwind Differencing Schemes for Problems Involving Fluid Flow," Comp. Maths. Appl. Mech. Eng., Vol. 9, 1976, p. 133.
- Leonard, B.P., "A Stable and Accurate Convective Modelling Procedure Based on Quadratic Upstream Interpolation," Comp. Maths. Appl. Mech. Eng., Vol. 19, 1979, pp. 59-98.
- Leschziner, M.A., "Practical Evaluation of Three Finite Difference Schemes for the Computation of Steady-State Recirculating Flows," Comp. Maths. Appl. Mech. Eng., Vol. 23, 1980, pp. 293-312.
- Leschziner, M.A., and Rodi, W., "Calculation of Annular and Twin Parallel Jets Using Various Discretization Schemes and Turbulence-Model Variations," ASME J. Fluids Eng., Vol. 103, 1981, pp. 352-360.
- Follard, A., and Siu, A.L., "The Calculation of Some Laminar Flows Using Various Discretization Schemes," Comp. Maths. Appl. Mech. Eng., Vol. 35, 1982, pp. 293-313.
- Huang, F.G., Launder, B.E., and Leschziner, M.A., "Discretisation of Non-Linear Convection Processes: A Broad Range Comparison of Four Schemes," Report TFD/83/1, Mech. Engr. Dept., University of Manchester, Manchester, England, 1983.
- Han, T., Humphrey, J.A.C. and Launder, B.E., "A Comparison of Hybrid and Quadratic-Upstream Differencing in High Reynolds Number Elliptic Flows," Comp. Maths. Appl. Mech. Eng., Vol. 29, 1981, pp. 81-95.
- Bemodakar, R.W., Goddard, A.J.H., Gosman, A.D. and Issa, R.I., "Numerical Prediction of Turbulent Flow Over Surface Mounted Ribs," ASME paper 83-FE-13, presented at the 1983 Applied Mechanics, Bioengineering, and Fluids Engr. Conf., June 20-22, 1983, Houston, TX.
- Militzer, J., Nicoll, W.B., and Alpay, S.A., "Some Observations on the Numerical Calculation

of the Recirculation Region of Twin Parallel Symmetric Jet Flow," Proceedings of the First Symposium on Turbulent Shear Flows, Penn. State Univ., April, 1977.

25. Gosman, A.D., and Fan, W.M., "Calculation of Recirculating Flows," Rept. No. HTS/74/2, 1974, Dept. of Mech. Engr., Imperial College, London, England.
26. Rhode, D.L., Lilley, D.G., and McLaughlin, D.K., "On the Prediction of Swirling Flowfields Found in Axisymmetric Combustor Geometries," ASME J. Fluid Mech., Vol. 104, 1982, pp. 378-384.
27. Lilley, D.G., and Rhode, D.L., "A Computer Code for Swirling Turbulent Axisymmetric Recirculating Flows in Practical Isothermal Combustor Geometries," NASA CR-3442, Feb. 1982.
28. Launder, B.E., and Spalding, D.B., "The Numerical Computation of Turbulent Flows," Comp. Methods in Appl. Mech. and Engrg., Vol. 3, 1974, pp. 269-289.